SENSITIVITY ANALYSIS OF CASTING DISTORTION AND RESIDUAL STRESS PREDICTION THROUGH SIMULATION MODELING AND EXPERIMENTAL VERIFICATION

DISSERTATION

Presented in Partial Fulfillment of the Requirements for
the Degree Doctor of Philosophy in the
Graduate School of the Ohio State University

By

Adham E. Ragab, M.S.

* * * * *

The Ohio State University
2003

Dissertaion Committee:

Dr. R. Allen Miller, Adviser

Dr. Khalil Kabiri-Bamoradian

Dr. Jerald R. Brevick

Dr. Jose M. Castro

Approved by:

_____

Adviser

Department of Industrial, Welding
& Systems Engineering

ABSTRACT

The die casting process is one of the net shape manufacturing techniques and is widely used to produce high production castings with tight tolerances for many industries. An understanding of the stress distribution and the deformation pattern of parts produced by die casting will result in less deformed from the part design specification, a better die design and eventually to more productivity and cost savings. This dissertation presents a technique that can be used to simulate the die casting process in order to predict the deformation and stresses in the produced part.

A coupled thermal-mechanical finite elements model was used to simulate the die casting process. The simulation models the effect of thermal and mechanical interaction between the casting and the die. It also includes the temperature dependant material properties of the casting. Based on a designed experiment, a sensitivity analysis was conducted on the model to investigate the effect of key factors. These factors include the casting material model, material properties and thermal interaction between casting and dies. To verify the casting distortion predictions, it was compared against the measured dimensions of produced parts. The comparison included dimensions along and across the parting plane and the flatness of one surface.

In order to validate and verify the die casting machine model, experimental work was conducted. The contact forces between dies and platens, strain in tie bars and dies

and die temperature were measured. The experiments were run on a 250 metric ton Buhler die casting machine available at the Ohio State University. A total of 68 sensors (35 load cells, 31 strain gauges and one thermocouple) were mounted on the machine. The readings from these sensors were compared to the similar simulation predictions.

Dedicated to my parents, my wife and my kids

ACKNOWLEDGMENTS

First of all, I would like to thank my advisor Dr. R. Allan Miller for his continuous guidance and support. Working with Dr. Miller was one of my most precious experiences. His technical knowledge, constructive criticism and patience can be noticed in every part of this dissertation.

I am very thankful to Dr. Khalil Kabiri for the enormous amount of time he spent with me on this research. I owe him most of my knowledge in simulation and experimental works. Dr. Kabiri's first name "Khalil" means "friend" in Arabic language, and he was really a very good friend during the time period of the research.

I am, also, grateful to Dr. Jerald R. Brevick and Dr. Jose M. Castro for their contribution and support as members of my dissertation committee. Dr. Brevick was very helpful in providing assistance and advice during the experimental part of this dissertation.

My gratitude to my past and present colleagues in my research group: Caixia Zhang, Ashish Vashisht, Abelardo garza, Hongyu Xue, Eduardo Arrambide and Jeeth Kinatingal for their help and support, especially in the experimental work. My gratitude, also, to the Industrial Engineering Department staff who were a great help in my work, especially, Darline Wine, Mary Hartzler and Cedric Sze and his team.

At the end I would like to express my deep gratitude to my wife, the one who supported me in every step of this research with patience and encouragement. I really owe her a big share of this dissertation.

VITA

October 28, 1968……..	Born – Sabha, Libya.
1990……..	B.S. Mechanical Engineering, Zagazig University, Egypt.
1996……..	M.S. Industrial Engineering, Zagazig University, Egypt.
1996 – 1998……..	Teaching Associate, Zagazig University, Egypt.
1998 – Present …….....	Graduate Research Associate, The Ohio Statue University.

PUBLICATIONS

Adham Ragab, Khalil Kabiri, Allen Miller, "Analysis of the Part Distortion and Stresses in Die Casting Process", NADCA 2001 Conference, October 2001, Cincinnati, OH, USA.

Adham Ragab, Khalil Kabiri, Allen Miller, "Modeling Part Distortion and Residual Stresses in Die Casting Process", NADCA 2000 Conference, November 2000, Chicago, IL, USA.

Yuming Ma, Adham Ragab, Khalil Kabiri, Allen Miller, "Qualitative Geometric Reasoning for Thermal Design Evaluation of Die Casting", ASME2000, 5th Design for Manufacturing Conference, September 2000, Baltimore, MD, USA.

FIELDS OF STUDY

Major Field: Industrial and Systems Engineering

Minor Field: Manufacturing

TABLE OF CONTENTS

LIST OF TABLES

LIST OF FIGURES

CHAPTER 1

INTRODUCTION

The die casting process is one of the net shape manufacturing techniques and is widely used to produce high production castings with tight tolerances for many industries. In the die casting process molten metal is injected under high pressure into a die cavity through the runner and gating system. This high pressure is applied via the plunger mechanism. A toggle system is required to hold the two halves of the die closed during molten metal ejection and intensification.

Castings are the final products of the die casting process, and care must be taken to guarantee their quality. A quantitative understanding of the stress distribution and the deformation pattern of parts produced by die casting will result in closer tolerances to the part design specification, a better die design and eventually to more productivity and cost savings. To achieve these objectives the casting and the dies have to be studied together as an integrated system. This will enable practitioners to more accurately predict the deformation of the part in the final form using analytical tools and to modify the die and parting surfaces based on the simulation results so that a dimensionally sound product will result.

Modeling and computer simulation of the die casting process has been a great challenge for the investigators. This process involves multiple inter-related phenomena. These phenomena includes, but are not restricted to, molten metal flow; part (casting) solidification; conduction through the part, the die, and the die machine components; casting and die interface heat transfer; heat transfer to and from the cooling and heating lines; and mechanical loads on the die and part. A complete die casting simulation should address molten metal flow starting in the shot sleeve and into the die cavity, followed by the heat transfer and structural simulation of the part and die casting machine.

1.1 Problem Definition

The Foundrymen's handbook [1] defines casting distortion (or casting warping) as "If the casting strains are great enough to force the casting from it's intended shape, it is said to be distorted". Figure 1.1 shows a distorted casting [2]. The strains that may cause distortion are being developed through the casting solidification and cooling.

The common reason for developing these strains in the casting is the variation of cooling rates between its different sections [3, 4]. Castings that suffer these variations may be subjected to cracks, distortion and structural weaknesses [3]. This variation in cooling rates may be due to casting design or casting process. Thin sections will cool more rapidly than the thick ones. This will result in the thin sections contracting ahead of the thick ones [3]. Sometimes contraction may take place in some sections and expansion in others due to the phase change, as in the case of steel castings [3]. Figure 1.2-a shows a casting of a simple shape, consisting of three parallel and straight members equal in

length and connected at their ends by cross members of equal length [3]. This casting will end as seen in Fiure1.2-b with the middle member distorted. This is because the outer members will cool faster than the center one [3].

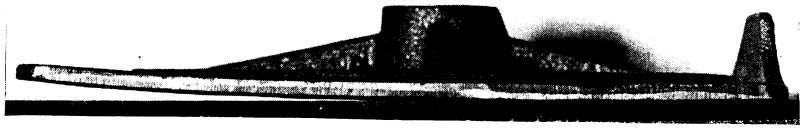

Figure 1.1: Distorted casting [2]

(a) (b)

Figure 1.2: Distortion in a simple part [3]

A solidifying material suffers deformation in a completely different way from that of a solid body [5]. This difference is due to the characteristics of the liquid, which displaces without causing stresses [5].

Figure 1.3 illustrates a simplified sequence of steps, which lead to the distortion and stresses in a solidifying casting [5]. The first step shows two thin liquid layers of the casting [i.e. outer layer and inner layer]. The outer layer (i.e. the one in contact with the chilled substrate) solidifies first, as expected, without generating significant stresses, unless it is stacked to the substrate, which is not our concern here. This stress free solidification is due to the relatively freedom of this layer to shrink towards the inner layer and displaces some of the liquid above it [5].

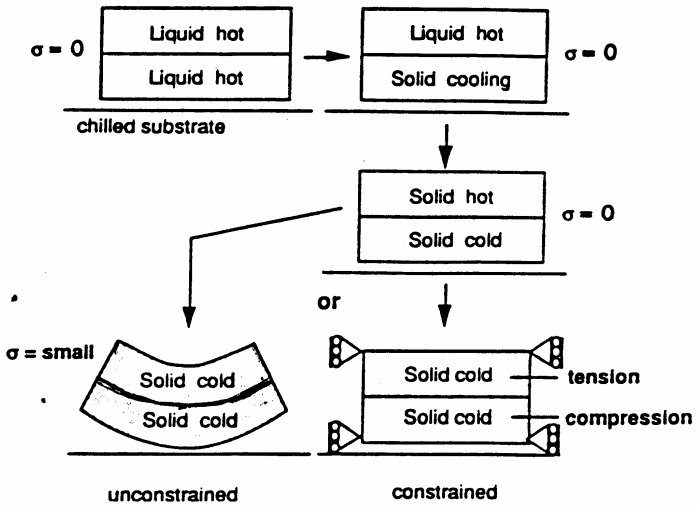

Figure 1.3: Mechanical behavior of a solidifying shell [5]

When the second layer solidifies, it also solidifies stress free. The final step shows that the inner layer tries to shrink, upon cooling, opposite to the mold face (chilled substrate), and there is no liquid to displace, thus results in the distortion shown [5]. This is repeated as later layers solidify. If the casting is restricted as shown, the distortion is prevented but the stresses in the shell will be very high [5].

To have a sound casting, allowances must be added to the pattern/mold design to compensate for the difference between the pattern/mold shape and the resultant casting. Shrinkage allowance and machining allowance are typical examples. For those castings that are subjected to distortion more than the allowable, distortion allowance must be added. This allowance is added to the pattern/mold depending on previous experience and/or by "trial and error" for a given alloy, and according to the casting process characteristics.

Modeling of deformation and stress in a solidifying body presents a monumental challenge from multi-physics involved to numerical solution algorithms. The solidification process needs an accurate description of the thermo-mechanical behavior of the solidifying body. The material, mechanical and thermal, properties of the solidifying part are highly temperature dependent. This temperature dependency will force simultaneous solution of the temperature and stress equations. Also temperature dependency of the properties will result in a set of non-linear systems. The stress relaxation and creep behavior during solidification will drastically alter the deformation patterns and residual stresses in a solidifying body and subsequent cooling. Therefore an accurate model of the creep-relaxation is required to predict the stress and deformation of casting in the final form.

In die casting processes part distortion is more complicated than in continuous or sand casting. This is mainly because of the enormous forces involved which may reach several thousands tons. The clamping load is applied to the dies and inserts; this load deforms the cavity shape. When the cavity is filled, the intensification pressure is applied to the part. This hydrostatic load will distort the cavity further more and will relocate the molten metal in the die cavity and keep the liquid under pressure during solidification. Therefore, the die cavity will be filled in its deformed shape. As the casting shrinks, it solidifies and in turn the die will react to the casting shrinkage.

Figure 1.4 shows the operation sequence in die casting process while Figures 1.5 shows the die distortion sequence in a simplified cavity shape.

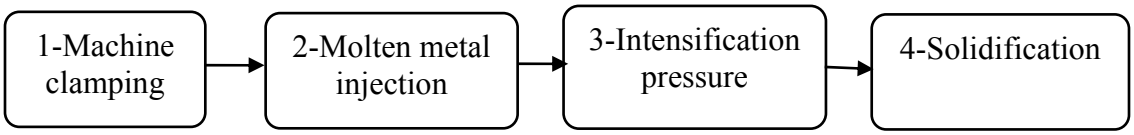

Figure 1.4: The die casting process sequence

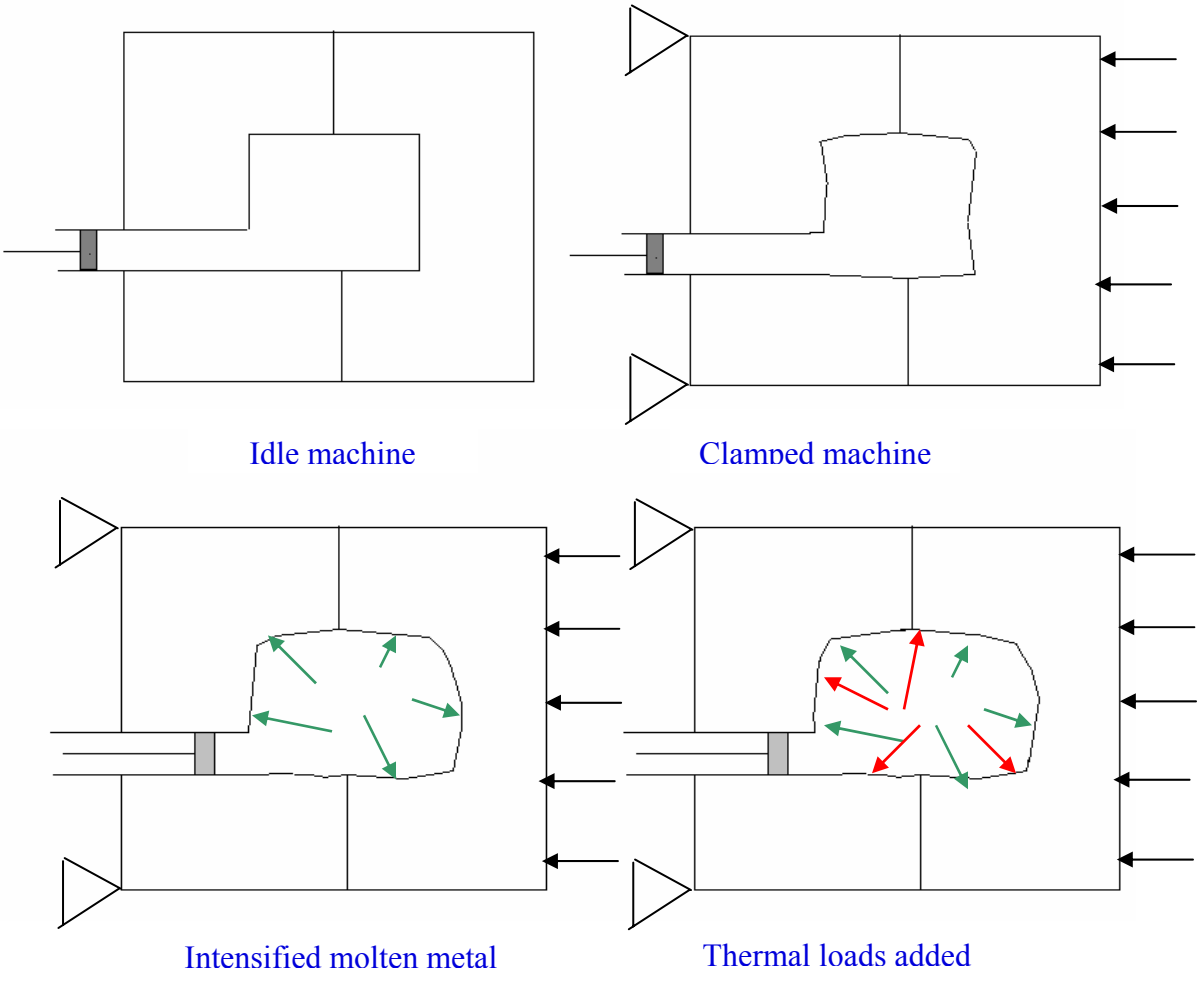

Figure 1.5: Die casting die distortion sequence

Another important issue is the formation of a gap between the casting and the mold surface. During the solidification phase the casting will shrink. The inserts will experience a cyclic thermal load and will grow from its initial size at room temperature. Gaps can form between the casting and the inserts. An approximate but representative model of the gap heat transfer is essential for correct prediction of the heat loss to the inserts. The heat loss to the inserts wall will decrease rapidly as the gap opening increases. The gap locations and its form may differ from cycle to cycle, until steady state operating conditions are reached.

The casting and die cavity geometry will limit the casting movement and will influence to a large degree the final casting deformation and stresses. The casting is not completely free to move or slide on the mold walls. The casting will interact mechanically with mold walls due to friction. The mechanical interaction of the casting and mold needs to be included in the simulation through contacting surfaces of casting and mold. The frictional effects will increase the system non-linearity and will drastically increase the computational time.

Due to interaction of the inserts and the casting, the final casting shape and its deformation cannot be predicted if only the casting is considered in the simulation. Therefore, it is imperative to include both the casting and inserts in the analysis under the thermal and mechanical loads and contact interaction between them. This will lead to increased model size and greater computational resources will be required. It is also known from previous experience that the effect of the machine parts on the whole die casting process is very significant [7, 8]. Therefore the machine components should be

included in the simulation. In particular, dies, platens, toggle system, and cooling lines must be modeled with their interactions with the part and the inserts. This will, even more, increase model size and complexity substantially and hence will increase dramatically the required computational powers.

1.2 Research Objective

The objective of this research was to build a model that represents the die casting process in order to predict the final part shape and residual stresses. A comprehensive model was required to take into account most of the factors that affect the part distortion and stresses. Sensitivity analysis was also needed to show the relationship between each one of these factors and the simulation predictions. Relative importance of the considered factors is very important for the process of model building and interpreting the results.

Part of the objective was to validate the adequacy of the model. Extensive experimental work was needed to achieve this goal. The results from the experimental measurements were compared to the corresponding output from the simulation model to verify that the model adequately represents the actual die casting process.

1.3 Research Methodology

In order to develop the required simulation model and validate it, the research was divided into two parts. These are the computer simulation part and the experimental part. In the computer simulation part the Finite Element Method (FEM) was used to build the die casting process model. In the experimental part, several measurements from the die

casting machine and casting dimensions were collected in order to validate the simulation model.

The computer simulation part of the research started with building the solid model of the machine parts (i.e. casting, inserts, dies and platens). The second step was to create the finite element model. This process was divided into several tasks: meshing, adding boundary conditions, adding initial conditions and building the loading sequence. The model was solved in the third step using the general purpose finite element package ABAQUS [9]. Post processing the results and evaluating its correctness was the fourth step. In this step the part deformation and residual stresses were retrived and doctumented. After determining that the model works as expected, the next step was to run sensetivity anslysis for the model, changing the values of some modeling parameters. The goal was to evaluate the significance of these parameters on the results. These parameters were:

- Material model (i.e. elastic, elastic-plastic and visco-plastic models).
- Yield strength of the casting material.
- Strain hardening of the casting material.
- Heat transfer coefficient between casting and inserts.
- Injection temperature.

The experimental section of the research aimed to validate the modeling criteria that were used in the simulation modeling part. Two categories of experimental data were collected and compared to the simulation results. The first category is related to the casting distortion. Three casting dimensions along the parting plane and one dimension

across the parting plane were measured. Also the flatness of one of the casting surfaces was measured.

The second category of experimental data was related to the die casting machine. The contact forces between dies and platens, strain in tie bars and dies and die temperature were measured. Three types of sensors were used to measure output from the machine during operation. Load cells were used to measure the contact force between the dies and platens. Strain gages were used to measure the deflection of the tie bars and dies. The temperature at one location in the cover die was measured using a thermocouple.

1.4 Outline of Dissertation

The dissertation is divided into six chapters (including this one) and five appendices. Chapter 2 is a literature review of casting process modeling. It covers some related work in flow modeling, thermal modeling and mechanical modeling. Several casting processes are considered, namely, continuous casting, sand casting, permanent mold casting and die casting.

Chapter 3 and 4 are devoted to the simulation part of the research. Chapter 3 describes the die casting finite element model. It starts with the model assumptions and its expected effects. Few aspects in FEA are depicted briefly in the next section. Some important issues in the model are then illustrated in detail. These include: model application case, boundary conditions, initial conditions and material properties. The governing equations are summarized at the end of this chapter.

Chapter 4 gathers the results from the simulation model. The first section includes a comparison between the simulation results using different material models. The sensitivity analysis results are covered in the second section. The third section takes account of the comparison between casting distortion predicted by the simulation model and the distortion measured from actual castings.

Chapter 5 explains the die casting machine experimentation. This chapter includes the experiment methodology, results and comparisons with the simulation predicted values. Chapter 6 includes the conclusions and the recommendations.

Appendix A includes the drawings of the casting, inserts, dies and the fixtures that were designed and manufactured for the experiment. Appendix B describes the characteristics of the different sensors used in the experimental work. Appendix C shows the LABVIEW program used in the data acquisition system to collect the data from the different sensors. Appendix D contains the raw data from the experimental work. Appendix E includes the simulation results for the different DOE cases.

CHAPTER 2

LITERATURE REVIEW

Modeling casting processes is a very complex problem, and the fundamental aspects of the problem have received very little attention in the literature. But now, with the advances in computational power and modeling facilities, research in this area is beginning to receive significantly more attention.

Most of the research on the modeling stresses and distortion in casting has been performed for continuous casting. The interest in continuous casting is due to its industrial importance, various complex defects that affect it and the simple geometries produced by this casting process (i.e. normally, ingots with rectangular or circular cross sections). These simple geometries allow using the simple 2D modeling techniques. Little research has been done in sand casting, permanent mold casting, or particularly in die-casting.

Several issues are presented in modeling casting processes. These issues include, but are not limited to, molten metal flow through the running system and gates, thermal analysis of the casting process, stresses formation in the casting and the die during

solidification and cooling, and predicting casting defects. In this chapter we try to investigate some of the research done under these titles.

2.1 Flow Analysis

One of the most common problems in casting processes is the improper runner system design. J. Campbell [11] states that 80-90% of casting problems are associated with the poor design of the filling path of the mold. Casting defects due to flow problems are mostly caused either by early solidification of the casting or trapped gas inside it [12]. Early solidification means that the casting may solidify before filling the whole cavity and leads to a non-complete casting [12]. The trapped air will cause porosity in the casting and hence degrading its quality. Both problems can be eliminated, or at least reduced, by proper design of the metal flow channels and air flow channels (vents) in the die [12]. The flow pattern will affect the casting temperature distribution and the cavity surfaces and hence affects the whole load history of the casting. Therefore an honest modeling of the mold filling should be the first step towards accurate modeling of the casting process.

The flow in the runner system in any casting process, even for small castings, is usually a turbulent flow with Reynold's numbers over 5000 [13]. Modeling turbulent flow is very expensive because of its, high non-linearity that requires very fine mesh, very long computational time before convergence and very small time increments [13]. Therefore, only laminar flow computations are usually considered in modeling the flow in casting process [14].

One of the widely used softwares to model casting process is MAGMASOFT. Several modules are available to model the molten metal flow in sand casting, permanent mold casting and die casting. This software allows modeling the turbulent filling of the molten metal into the mold. The MAGMASOFT uses FDM as a solver [15].

2.2 Thermal Analysis

As previously mentioned, the main reason that strains develop in the casting is the variation in cooling rates within its volume. These strains are defined as thermal strains. The temperature history of the casting must be known at every point accurately in order to compute the developed thermal strains [6]. This requires solving the thermal problem of the model before solving the mechanical one, or simultaneously with it [6].

Rosindale and Davey [16,17] conducted a research to develop steady state and transient thermal models for the hot chamber injection system in the die casting process. These models were created to predict both the steady state and transient thermal behavior of the injection system and die. The three dimensional model was represented using boundary element method (BEM). The models studied the heat flow through the nozzle, gate and the runner. The results from both models were verified against experimental data, and they were used to submit recommendations to improve the thermal behavior of the process.

Thomas et al [18, 19], developed a two dimensional model to predict the thermal behavior of steel ingots in continuous casting. The goal was to use these results as an input to a mechanical analysis model in order to predict the thermal stresses in the ingots.

The results from the heat flow model were verified with analytical solutions and with measurements from industry.

Barone and Caulk [20] developed a new technique used for thermal analysis in die casting. This new method relies on the fact that, under some conditions, the temperature distribution in the die, below some certain depth, is independent of the time. This fact allows solving for the transient phase only for the cavity surface and very small depth below it, and considers the rest of the die as in a steady state temperature distribution.

Related to the previous research, Bounds et al [21] presented a thermal model for the pressure die casting process. The finite element method (FEM) was used to model the thermal behavior of the casting, while the boundary element method (BEM) was used to model the thermal behavior of the dies. The transient solution is found only for the die surfaces close to the cavity, while the rest of the die is considered in the steady state.

Two important aspects in the thermal analysis are latent heat and interfacial heat transfer coefficient, which are discussed in the following sections.

2.2.1 Latent Heat

Latent heat is the amount of energy required to change a unit mass of liquid into solid or vise versa. Pure metals and eutectic alloys have a sharp distinction between the solid and liquid phases [14, 22], i.e. the material phase changes at a constant temperature. While in a conventional alloy the phase change takes place over a temperature range. The limits of this range are named solidus temperature (the lower limit) and liquidus temperature (the upper limit). This range differs greatly between alloys. In this

temperature range the material is composed of both solid and liquid phases, and hence the material is said to be in the mushy zone.

Voss and Tsai [22] investigated four latent heat release modes. These are linear and quadratic modes, lever rule and Scheil's equation. The four patterns were simulated for two alloys, steel alloy with narrow mushy zone and aluminum alloy with wide mushy zone. Both the alloys were cast in a sand mold. According to their results, the latent heat release pattern affected the flow, temperature and solidification results of the simulation model and the difference was significant between the four models in the aluminum alloy, while it was insignificant in steel alloy. Hence their conclusion was that for wide mushy zone alloys the latent heat release pattern in the model should be studied, and the actual pattern should be used in the simulation to get accurate results.

R.W. Lewis et al [14], classifies the various methods to manipulate the latent heat in finite element models under two categories, **front tracking methods** and **fixed grid methods**. In front tracking methods the solid-liquid interface is continuously tracked. The solid and liquid zones are treated as two separate zones [14]. This method has some advantages, which are [14]:

- Predicts the location of the liquid-solid interface accurately.
- Releases the latent heat accurately.

While the disadvantages of this method are [14]:

- Special purpose computer programs are needed to run it.
- Does not suite to alloys with finite freezing range.
- Can be practically applied to simple geometries only.

In fixed grid methods both the solid and liquid zones are treated as one continuous zone [14]. The advantages of this method are [14]:

- Can be easily applied in any available conduction program.
- Does not need to track the interface in each time increment.
- Does not require remeshing.
- Applies to alloys with finite freezing range.
- Can be applied to simple or complicated geometries.

While the disadvantages are [14]:

- The conservation of energy is sometimes approximate.
- The interface may not be predicted accurately.

2.2.2 Interfacial Heat Transfer Coefficient

Theoretically the casting/mold is assumed to be in perfect contact after pouring the metal in the cavity. As the molten metal solidifies, a gap may form between them. The gap is mainly formed by the relative motion, due to distortion and shrinkage, between the casting and the mold [23]. The gap width and position affect the heat transfer coefficient between the casting and the mold, and hence the temperature history of the casting. The gap position and width cannot be pre-determined by part geometry even for a simple casting shape, and hence it should be predicted from the simulation [11]. Figure 2.1 [11] shows the decrease of the heat transfer coefficient in permanent mold casting versus time. This decrease is mainly due to gap formation between the casting and the

mold [11]. Figure 2.2 shows the position of air gaps formed in sand casting for a simple part geometry [11].

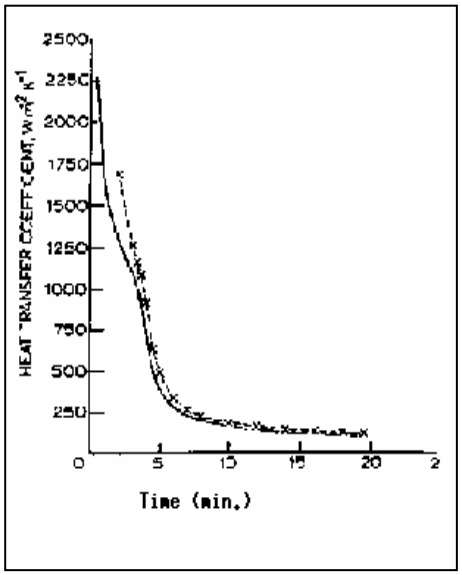

Figure 2.1: Heat transfer coefficient vs. time in a permanent mold casting [11]

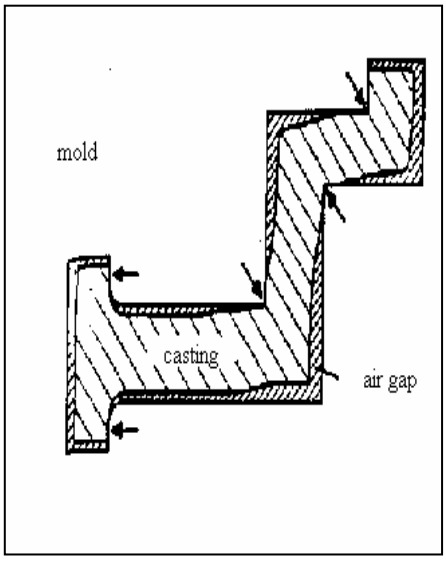

Figure 2.2: Positions of air gaps in a sand casting [11]

Nishida et al, [23] designed an experiment to measure gap width and heat transfer coefficient through it. The experiment was performed for cylindrical and flat castings. Two materials were chosen for these castings. They are pure aluminum and aluminum alloy with 13.2% silicon content. The gap width was measured as the distance between the mold inner surface and the casting outer surface. The heat transfer coefficients were calculated depending on the measured temperatures in the casting and the mold. Different gap formation sequences between the cylindrical and flat castings were noticed. In the

cylindrical casting case the gap started very small immediately after pouring but with no significant effect on the heat transfer coefficient. When contraction began, the gap started to increase and the heat transfer coefficient decreases significantly. In the case of flat casting the maximum gap width was reached before the contraction of the casting starts due to the movement of the mold.

Hwang et al, [24] calculated experimentally the heat transfer coefficient between an aluminum alloy 356 casting and a resin-bonded sand mold. Two methods were used to calculate the heat transfer coefficient. The first one was measuring the distance between the casting and the mold and then calculating the heat transfer coefficient depending on this distance. The gap width was measured using very sensitive displacement gages. The second method was to calculate the temperatures at different locations in the casting and the mold, and then using the inverse method to calculate the interfacial heat transfer coefficient. According to their results the inverse method gave interfacial heat transfer coefficient that is ten times higher than the other method. They also declared that the composition of the gas entrapped inside the gap is very significant in the calculation of heat transfer coefficient. The effect of the gas type is shown in Figure 2.3 [11].

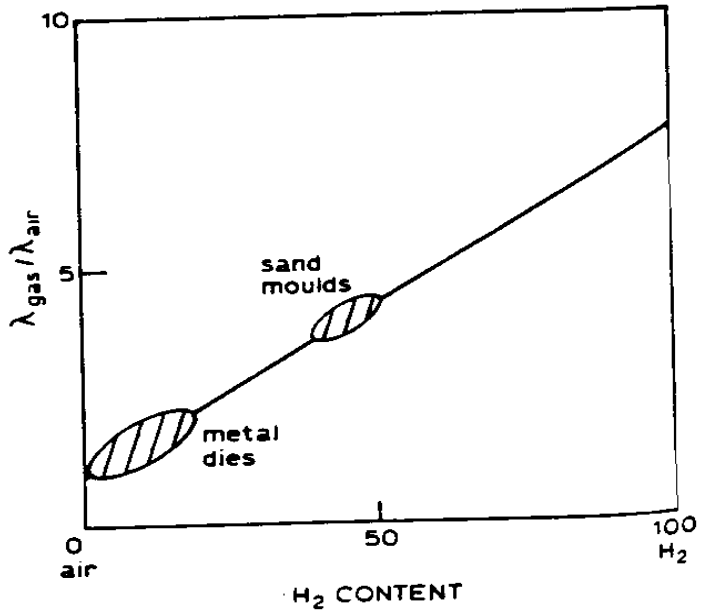

Figure 2.3: Effect of hydrogen content on heat transfer coefficient through gap [11]

Hou et al [25] ran experimental work to measure the interfacial heat transfer coefficient between an Al – 13% Si alloy casting and a dried silica sand mold. The results are given in Table 2.1. As shown in the table the heat transfer coefficient (H_g) drastically decreases with increasing the gap.

Time (seconds)	Gap width (μm)	H_g Values (W/m^2K)
240	2.0	5298
300	5.0	2101
360	10.0	1050
480	23.0	460
600	34.0	312
720	40.0	267
840	45.0	233
960	52.0	204
1020	52.0	204
1080	57.0	187
1140	66.0	159

Table 2.1: Interfacial heat transfer coefficient (H_g) between an Al- 13% Si alloy casting and a dried silica sand mold versus gap width [25]

Lewis and Ransing [57] studied the interfacial heat transfer coefficient in order to optimize the design of the feeder. Their model was applied on an axisymmetric aluminum gravity die casting. They developed a thermo-elasto-visco-plastic model to predict the air gap depending on the deformation of the casting with respect to the mold. In their research also, they accounted for the relative motion between the casting and the mold using special elements (interface elements).

Due to the significant effect of gap formation on the temperature history of the casting, and hence on its final deformation, it should be considered in modeling die casting part distortion. No literature was found that study the gap formation in die casting. However the effect of the gap in die casting is expected to be very close to the

effect in permanent mold casting, though the gap formation mechanism is completely different due to the huge pressure applied in die casting.

2.3 Mechanical Analysis

2.3.1 Thermal Stresses

Dantzig [26] explained in details the development of thermal stresses in metal casting. In his research finite element analysis was used to solve the modeling problem numerically. The finite element model was explained step by step in conjunction with the constitutive equations. The model was created for homogeneous, isotropic, material deformed under plane strain conditions.

Two applications were run using this model. The first application was uncoupled thermal-mechanical analysis for a gray iron casting in a sand mold. The second application was coupled thermal-mechanical analysis of continuous steel casting.

Smelser and Richmond [27] studied the effect of the constitutive model on stresses and deformations. The application was on a solidifying circular cylinder made of pure aluminum. A finite element model was built and the finite element code ABAQUS was used to solve it. The thermal part of the model was designed based on temperature measurements. Using an inverse heat conduction technique, the heat flux value versus time was calculated as shown in Figure 2.4.

In this research two constitutive models- inelastic constitutive model and elastic constitutive mode- were compared against each other. The comparison has shown that the elastic constitutive model might be useful in the preliminary process design phase, but for

accurate estimates of stresses and air gap formations, the inelastic constitutive models should be used. Figure 2.5 shows the model predicted stresses using both models. From the figure it is very clear that the elastic constitutive model overestimates the stresses.

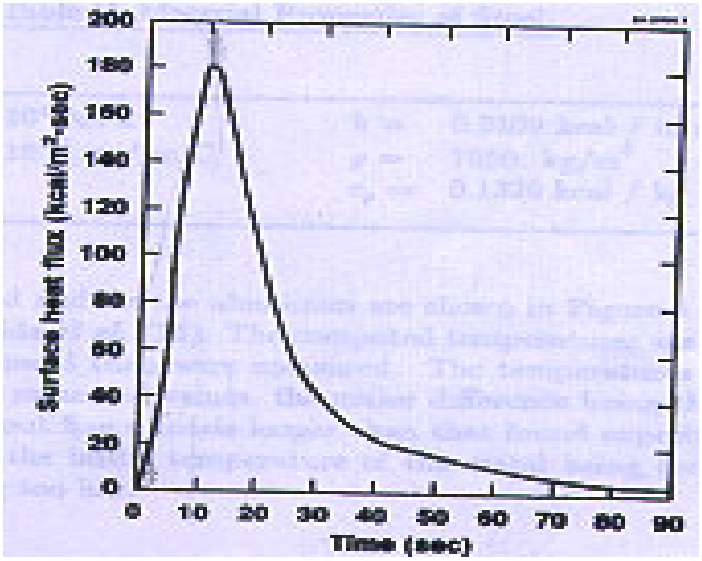

Figure 2.4: Surface heat flux versus time [27]

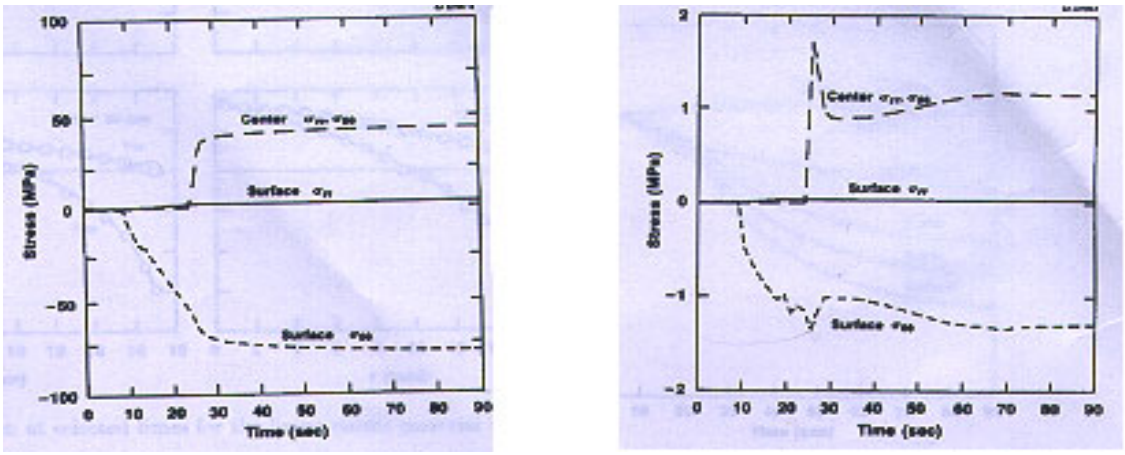

a b

Figure 2.5: Model predicted stresses using a: elastic constitutive model and b: inelastic constitutive model [27]

Selection of the constitutive model to be used in the simulation is not a trivial problem, since the required material properties are not always available. In modeling casting processes the material properties are required at elevated temperatures which is not easy to find. So the modeler may have to work with uncertainty of his material properties, and sensitivity analysis may be needed to explain the results. Another problem is the tractability of the simulation model and the expected cost of using a complicated constitutive model.

Kelly, et al [28] developed a mathematical model to simulate the thermo-mechanical behavior of continuously cast steel in round molds. This model included the

effect of billet velocity inside the mold and the gap formation on the heat transfer coefficient. Their simulation model was one of the first models to account for the dynamic effects on the heat transfer coefficient and also consider the plasticity of the casting material.

N. Zabras et al [29] built a finite element model to be used in simulating continuous or ingot casting process of pure aluminum. This model is limited to castings of axial symmetry or plain strain casting conditions. In this model the thermal and mechanical analyses are uncoupled. A hypoelastic-viscoplastic constitutive model was used. The effect of different melt pressure rates and cooling rates is examined and presented in the paper. According to the results the liquid pressure had significant effect on the stresses pattern in the ingot at the early stages of solidification, while its effect at the end of cooling was negligible. The results also showed that the liquid pressure may play a significant role in the formation of the air gap. As was expected, the stresses in the ingots were very sensitive to the cooling rate. In die casting, the pressure is much higher and its effect on gap formation needs to be studied accordingly.

K.C. Wang, et al [30] used both finite difference and finite element methods to analyze the thermal stresses formation in sand casting of cast iron. FDM was used to compute the temperature distribution in the casting, while the FEM was used to predict the thermal stresses depending on the temperature results. The cast iron properties were given as a function of temperature.

Kristiansson [31] created a two dimensional numerical model to calculate the developed stresses and strains during solidifications of steel in continuous casting.

Different steel types and different cooling conditions were examined. The results were verified against an exact solution of one dimension problem.

In two related papers, B.G. Thomas et al [18, 19] presented their mathematical model to predict the internal stresses generated in a steel ingot in continuous casting. The model was divided into two parts, the thermal part and the stress part. A transient, elasto-viscoplastic finite element analysis was used to solve the model.

R. N. Parkins and A. Cowan [32] ran several experiments to study the mechanism of residual stress formation in sand casting. The experiments were run for different alloys. The results showed that the residual stress in sand castings is a result of three factors:

- Temperature differences in the casting during cooling.
- Phase transformation in the alloy.
- The sand resistance to casting contraction.

According to their results, the most significant factor is the temperature difference in the casting.

2.3.2 Mold & Machine/Casting Interaction

Thomas states that the effect of mold/casting interaction on the final shape of the part and its residual stresses is very significant [5, 6]. While inside the mold the casting may not be free to distort against the die surface, leading to residual stresses build up. This is usually the case when the mold is made of metal or ceramic. The stress history of the part alters due to the mold constraints, and hence, the final part distortion and stresses are expected to change. Another factor, in the interaction between the casting and the

mold, is the gap formed between them. The gap effect was explained earlier in this chapter. The effect of the mod on the casting behavior is more complicated if there is a relative motion between them as in continuous casting.

Also the shape of the mold changes due to cavity pressure, clamping loads and thermal expansion. The final shape of the part is a function of the mold shape. Figure 2.6 shows the effect of mold distortion on the casting shape [11].

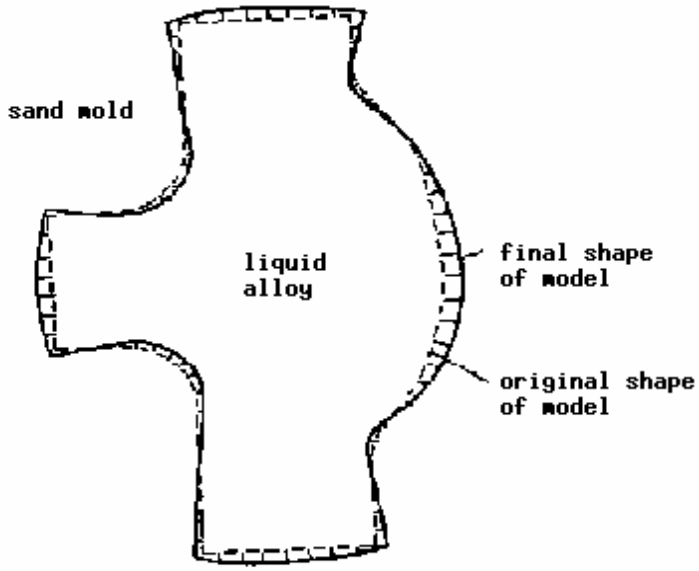

Figure 2.6: The effect of mold distortion on casting shape [9]

R. Miller et al [7,8,] have shown, in their research on modeling die casting processes, the effect of different machine parts on the die distortion, and hence on the part final shape. According to their results, platens, slides and tie bars sizes and locations with respect to the die were proven to be very significant and must be considered when modeling the die casting process.

A fundamental question arises about the possibility of predicting casting distortion, in a die casting process, ignoring the mechanical loads in the solidification stage and keeping the required accuracy at the same time. Considering the die casting machine in a casting distortion model may answer this question.

CHAPTER 3

MODEL DESCRIPTION

3.1 Model Assumptions

Die casting is a very complex process and the researchers are faced with a large number of hard to solve physical problems when tackling its computer modeling. Due to these challenges, it is deemed necessary to start the modeling with some assumptions. Although these assumptions may affect the results, it is the only way that a researcher can get a tractable model for the die casting process. Usually a researcher concerns only with one particular area of die casting processes and ignores, or assumes, the other aspects. These assumptions are not only due to the complexity of the physical phenomena that are involved, but also due to the limitations of the software that may be used, this includes both finite elements and finite difference packages presently available. Some of these softwares are designed particularly for die casting and some others are general-purpose ones. In the first category the assumptions are already built in the software to fit the particular end user. The user gets the results with these assumptions in mind. In the latter category, the user is free to manipulate his assumptions depending on his/her thoughts and goals. One thing to keep in mind is that, even for the general-purpose packages, some

assumptions are buried within the package code itself. In our research a general-purpose finite element package (ABAQUS) was used to simulate the die casting process.

Several assumptions were made in our simulation model, which aims to predict the casting distortion and residual stresses after complete cooling. The first significant assumption was the instantaneous cavity filling. This means that the cavity filling stage was not considered in our model. Although considering the cavity filling stage is very important in modeling the casting process, it increases the modeling complexity as a result of different flow patterns expected in the shot sleeve, gate, runner and different cavity features [8]. The flow of gas from the cavity through the vents is another factor that was ignored in our model as a result of this assumption.

Our second assumption was that the cast metal has uniform temperature distribution inside the cavity, at the starting point of simulation. This temperature was assumed to be above the liquidus limit, i.e. the solid fraction was 0.0% of the cast metal at the start of simulation. This assumption was related to the first one. In other words, it was impossible to estimate the temperature distribution of the molten metal inside the mold without modeling the filling stage applying the heat and mass balance equations.

The third assumption was due to ABAQUS limitations. ABAQUS cannot deal with multi-phase models; therefore, solid elements were used to define the casting instead of multi-phase (liquid/solid) elements. Liquid elements can carry the hydrostatic pressure from the shot sleeve and apply it on the cavity surfaces, while the solid elements do not have this capability. To compensate for this assumption we added the cavity pressure as a boundary condition and applied it on the cavity surface separately from the part. Another

issue with this assumption was that the liquid casting can follow the cavity shape when it distorts. With the use of solid elements to represent the casting during its liquid state the capability to follow the cavity is lost.

The last assumption was that all the applied loads are static loads only. This includes clamping and cavity pressure. Although the motion of the machine parts produces dynamic loads, modeling it is very complicated and beyond the scope of this research.

3.2 Finite Element Method (FEM)

Finite Element Method (FEM) is a powerful computational tool that is used to numerically solve many engineering problems. As mentioned in chapter 2, most of the research on the area of casting processes modeling, uses FEM as a solver to the casting process model. The definition of FEM is as follows: "The FEM is a computer-aided mathematical technique for obtaining approximate numerical solutions to the abstract equations of calculus that predict the response of physical systems subjected to external influences." [38].

3.2.1 Analysis Type

The solution of the energy equation to define the temperature history of the casting (i.e. the thermal analysis) may be done separately from the stress analysis. This type of solution is called uncoupled (or sequentially coupled) thermal-mechanical analysis. It consists of two subsequent runs: (i) thermal analysis, and, (ii) stress analysis.

This method may be used when the stress and/or deformation field in a body depends on its temperature field, while the temperature field can be found without the need to know the stress and/or deformation field [9].

Another analysis technique is to solve the thermal analysis at the same time with the stress analysis. This technique is called coupled (or simultaneously coupled) thermal-mechanical analysis. This type of analysis is done when the temperature field and the stress and/or deformation fields are affecting each other simultaneously.

Both techniques are used in modeling casting processes. In our model the effect of air gap on the heat transfer coefficient between casting and dies and the dependence of material properties on temperature lead to interchangeable effect between thermal and stress results. Therefore the coupled analysis was the only option for our simulation model.

The heat transfer problem by its nature is a time dependent problem. In die casting process the part is ejected from the die before its temperature reaches the steady state and then it is left to cool down to room temperature (the steady state temperature). After part ejection, the cycle starts over again with a new part. Due to this cyclic loading of dies and different cooling phases seen by the part, transient analysis is needed to predict the part thermal history.

As previously mentioned in the beginning of this chapter, we assume that all the loads were static. Hence the complete description of the analysis in this model is: *transient coupled thermal mechanical analysis.*

Before starting the coupled analysis, a thermal analysis was run to reach the steady state temperatures of the machine parts and use it as the initial condition of the

coupled analysis. Ten thermal cycles were simulated till the change in temperature between cycles was less than 5 ^{o}C. At this point the temperature distribution of the dies and inserts was considered close enough to the steady state. Table 3.1 describes the thermal cycle.

Cycle segment	Time (Sec)
Die closed – casting is injected	9
Die open	3
Casting ejection	3
Die open - idle	10
Ejector die spraying	4.5
Die open - idle	3
Die closed – idle	7.5
Total cycle time	40

Table 3.1: Thermal cycle time

3.2.2 Element Type

Several element types are available for modeling casting processes. Some of them (2D elements) may be suitable for very simple parts, which is not the usual case in die casting. In our model we use 8-noded 3D brick elements. According to ABAQUS manual [9], brick elements are more reliable than tetrahedral elements, especially in solidification and stress analysis. The linear tetrahedral elements are overly stiff [9], while the quadrilateral tetrahedral elements suffer from what is called “Spurious oscillations due to

small time increments [9]". This phenomenon leads to meaningless temperature values in the quadrilateral tetrahedral elements.

The 8-noded brick (hexagonal) element is a linear element that can be used in thermal, mechanical and coupled analysis. In coupled analysis the element has 4 degrees of freedom; three degrees of freedom for the displacement (u_x, u_y, u_z) and one degree of freedom for temperature (T). Figure 3.1 shows the 8-noded hexagonal element and its node numbering [9].

Trying to simulate the cavity pressure as a hydrostatic pressure applied within the casting, two element types were investigated, but success was not achieved. One of these elements was the *hybrid* element. This element is used to simulate the incompressible materials. According to ABAQUS manual, this element can transform hydrostatic pressure. This element was used to model the casting and the intensification pressure was applied as a hydrostatic pressure on the biscuit. Although the element could transform some of the hydrostatic pressure to the cavity surface, it was not capable of transforming the whole pressure. This problem was detected easily by reviewing the reactions at the constrained nodes. Besides this problem the hybrid elements suffered unreasonable deformations at high temperatures. Due to these two problems the hybrid elements were not used in the analysis.

The second element type used was shell elements. The outer surface of the casting was covered with shell elements, and pressure boundary conditions were applied on the shell elements with negative values (i.e. the pressure is going out of the casting towards the cavity). This technique worked with the elastic analysis, but it suffered serious

convergence problems with plastic analysis and hence it was not possible to use in the current model.

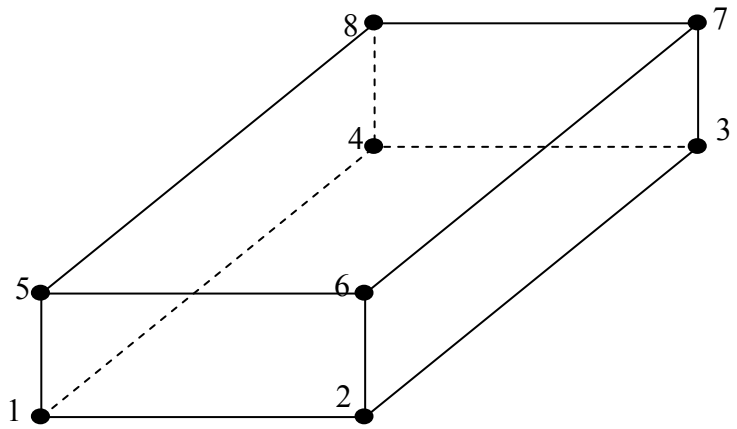

Figure 3.1: 8-noded hexagonal element [9]

3.2.3 Non-linearity

Three sources of non-linearity may be contained in a finite element analysis [9]. These are geometric non-linearity, material non-linearity and boundary non-linearity [9]. Geometric linear analysis assumes that both the displacements and strains remain small during the analysis. In other words the element keeps its geometry during the loading process [39].

Material non-linearity is a result of the dependence of material properties on a field variable. In this model most of material properties are functions of temperature as

explained before in this chapter. For a transient thermal analysis, the latent heat always causes non-linearity. Also for the plastic analysis with strain hardening and for creep analysis the material behavior under loading is non-linear. So the material non-linearity was acknowledged in our model.

The boundary non-linearity arises at the interfaces between the different parts in the model. The main source of boundary non-linearity in the model is the contact boundary conditions. Contact boundary conditions causes non-linearity due to the changes in the contact condition during the solution. At one time step two elements may be in contact, and in the next time step they are not. This leads to non-linear alteration of the loading conditions of the two elements. The friction between parts increases the effect of the contact non-linearity due to the heat generation and reaction forces resulted from the friction. Another source of boundary non-linearity is the dependence of gap conductance on gap width for the casting/inserts contact surface.

3.3 Model Application

3.3.1 The part

The simulation model was applied on a test part, Figure 3.2. The part was designed previously for another research [40]. A detail drawing of this part was not available and the dimensions used were measured from previously cast part. The part drawing is shown in appendix A.

The part model was simplified from the original one to facilitate the special mesh required by the coupled thermal mechanical analysis. The simplifications included

removing the overflows, drafts and fillets from the casting. Also, any surface curvature was straightened.

- The part overall dimensions are:

Length =	250 mm
Width =	100 mm
Height =	50 mm
Maximum thickness =	5 mm
Minimum thickness =	2.5 mm

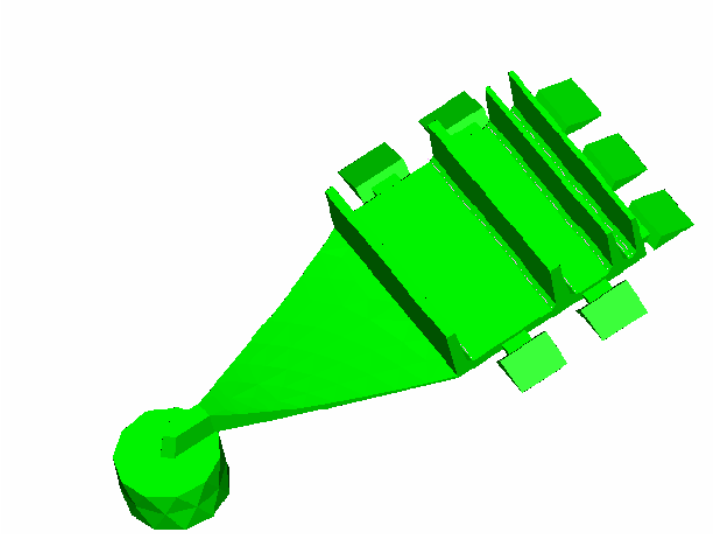

Figure 3.2: The test part used in the model

3.3.2 The machine

As mentioned before one of our goals was to investigate the effect of the machine on the part distortion. Several parts of the machine were added to the model besides the casting. These were the inserts, dies, platens and tie bars. Figures 3.3 & 3.4 show the finite element model and the schematic drawing of the modeled half of the die casting machine respectively.

The machine modeled was the BUHLER H-250SC, which is available in the Ohio State University, Net Shape Manufacturing Lab. The machine capacity is 250 tons. Drawings of the inserts and dies are given in appendix A. The tie bars were modeled as springs to simplify the model. The stiffness of springs was defined to be equal to the tie bars stiffness.

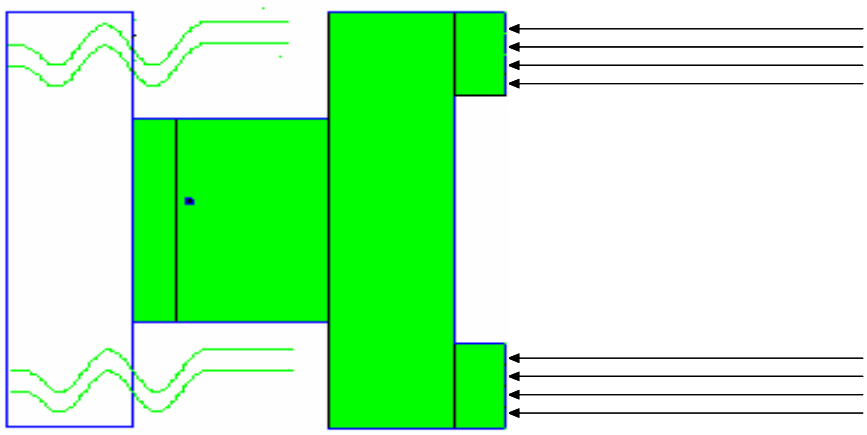

Figure 3.3: Half model of the die casting machine

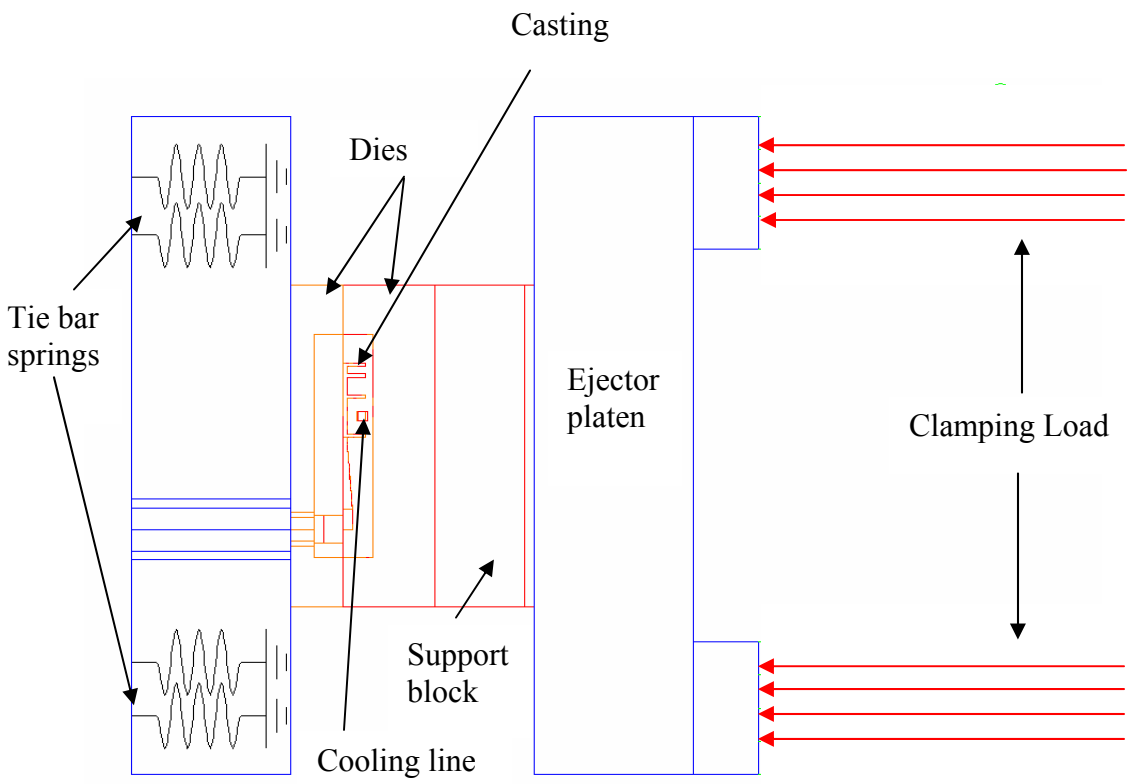

Figure 3.4: Schematic drawing of the die casting machine model

3.3.3 Model mesh

Figure 3.5 shows the mesh of the casting, inserts, dies and platens. For each part the front and side views are given.

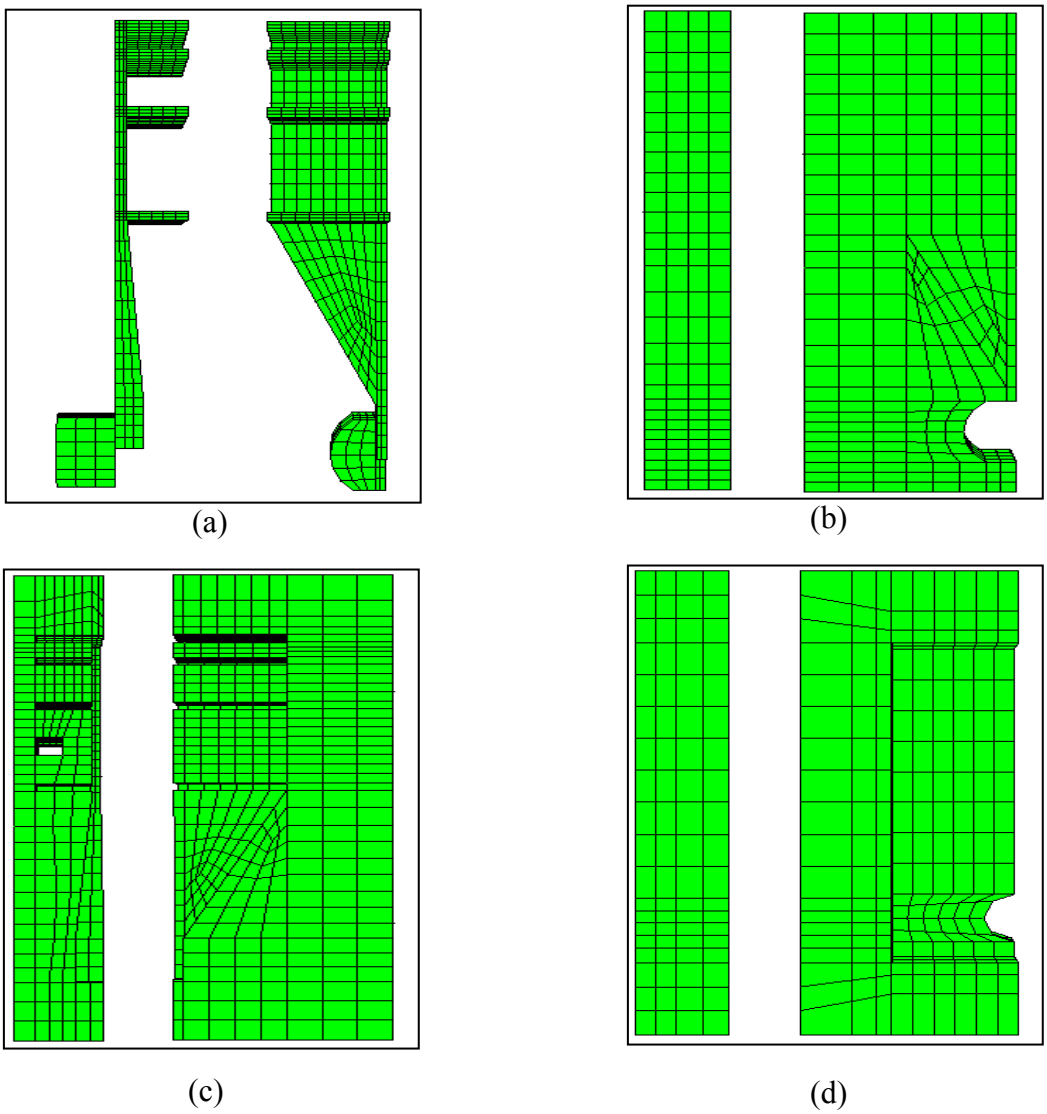

Figure 3.5: The mesh of casting (a), cover insert (b), ejector insert (c), cover die (d), ejector die (e), cover platen (f), ejector platen (g)

(Continued)

Figure 3.5: Continued

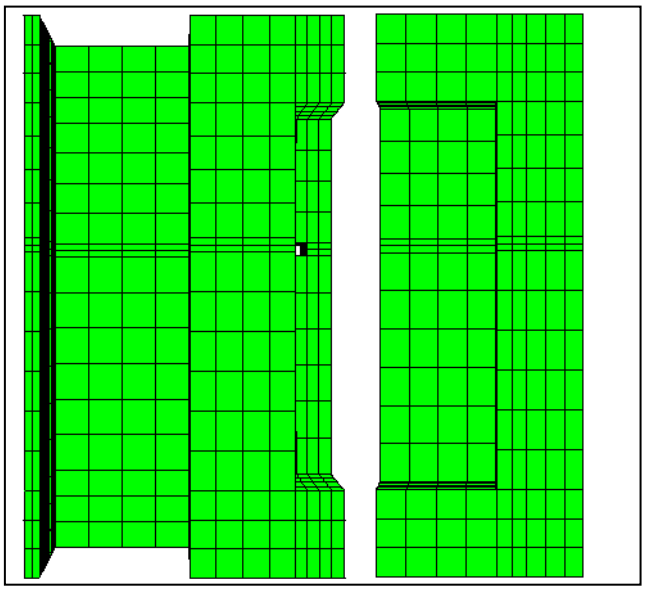

(e)

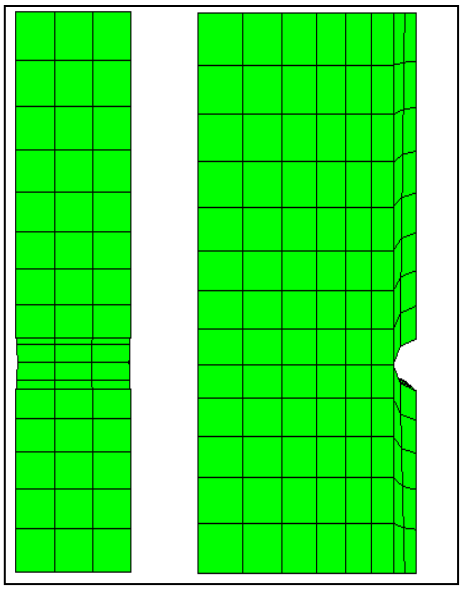

(f)

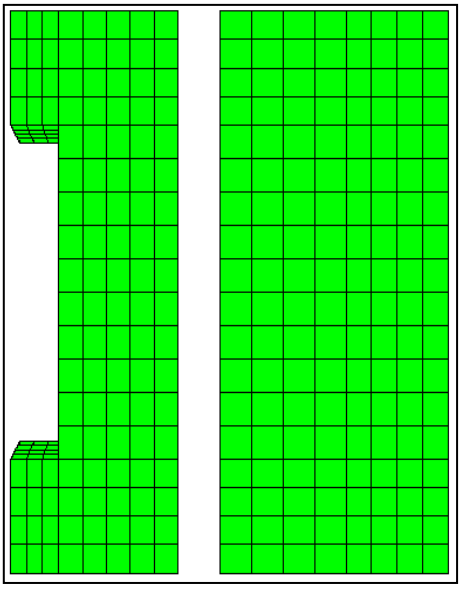

(g)

3.3.4 Cycle description

The cycle in the simulation is divided into several steps:

1. At the beginning a thermal analysis is run for dies inserts, and part for 10 cycles to allow the temperature distribution in the machine parts to reach close to its steady state. The thermal cycle is given in Table 3.1.
2. A coupled thermal-mechanical analysis is run using the temperature distribution from the thermal analysis as the initial condition. At the start point of the coupled analysis, the casting is inside the die cavity and the mechanical loads (i.e. the machine clamping and cavity pressure) and the thermal load (i.e. the heat transfer between the casting and the cavity surface) are applied.
3. At ejection, the casting is exported with its in-die displaced coordinates, temperature distribution and stress distribution.
4. The casting is then cooled in air of constant temperature equal to $30^{o}C$ and a heat transfer coefficient equal to 25 W/m^2K.
5. To investigate the effect of quenching, the previous step was repeated with water of constant temperature equal to $20^{o}C$ and a heat transfer coefficient equal to 200 W/m^2K.
6. To examine the effect of no residual stress distribution at ejection time, step 5 is repeated for the casting without any residual stress (i.e. at ejection, the casting is exported with its in-die displaced coordinates and temperature distribution only).

3.3.5 Model modifications for experimental work

Details about experimental work are given in Chapter 5. The simulation machine model was modified to include the load cells and their fixtures. Zhang C. [10] ran the first model of the machine including fixtures and load cells using the 8-noded brick elements. The results showed that the model could not predict the load on some of the load cells. The 8-noded brick element is a linear element; it was thought that the problem may be resulting from the shear locking. So the solid model was remeshed using the 10-noded quadratic tetrahedron element. The new mesh showed better results for the load cells. In addition, with this new mesh, the part model simplifications (section 3.3.1) were not needed, and the model was modified accordingly.

Another modification was to add the tie bars explicitly to allow comparing the tie bars strains to the experimental measurements. The last modification was to model the toggle mechanism as springs and apply the clamping load through displacement in the springs. This modification was to investigate the reasons of some differences between load cells loading predicted by the simulation and measured in the experimental work.

3. 4 Boundary Conditions

The test part is symmetric around one axis, hence only half of it – and of the machine – was modeled. The other half was replaced with symmetric boundary conditions. The clamping load was also applied as a boundary condition pressure on the back of the ejector platen as shown in Figure 3.4.

As explained before, the cavity pressure was applied as a boundary condition on the cavity surface. The cavity pressure was assumed to be constant value at 69MPa (10,000 Psi) and uniformly distributed over the cavity surface

Convection boundary conditions were also used in the model to represent the heat transfer between *dies & air, platens & air*, and between *the part & air* after ejection. The heat transfer coefficient to the air and the air temperature were assumed constant and equal to 25 $W/m^2.K$ and 30^oC respectively.

3.4.1 Heat Transfer Coefficient

Almost all the deformations and stresses in a casting are a result of variation of cooling rates in its different sections [3, 4]. Therefore the temperature history of the casting is very significant in the analysis. The interfacial heat transfer coefficient between the casting & inserts affects the temperature history of the casting. This effect may, or may not, be significant depending on thermal conductivity of casting and mold, casting geometry and solidification time. In this model, three different levels (A, B & C) of the interfacial heat transfer coefficient between the casting and the inserts were investigated, as shown in Table 3.2. In level A the heat transfer coefficient was a function of gap width between casting and inserts. There is very little in the literature about the effect of gap width on heat transfer coefficient in die casting. However we could use some values based on the research done in permanent mold casting [11, 23-25, 57]. Table 3.3 shows the heat transfer coefficient versus gap width. The heat transfer coefficient was assumed to change linearly between the given values.

In level B; the heat transfer coefficient was constant and equals to 5000 W/m^2K which is the maximum value in Table 3.3. This is the value at zero gap width. In level C the heat transfer coefficient was constant and equals to 2750 W/m^2K which is the median value in Table 3.3. The heat transfer coefficient between inserts/dies and inserts/platens were assumed to be constant and equals to 5000 W/m^2K.

Level	Interfacial heat transfer coefficient between the casting and inserts
A	Function of gap width as given in Table 3.2
B	Constant and equal to 5000 W/m^2K
C	Constant and equal to 2750 W/m^2K

Table 3.2: Levels for heat transfer coefficient between casting and inserts

Gap width (μm)	Heat transfer coefficient (W/m^2K)	Gap width (μm)	Heat transfer coefficient (W/m^2K)
0.0	5000	0.7	2500
0.2	4500	1.25	2000
0.35	4000	2	1500
0.5	3500	4	1000
0.55	3000	12	750

Table 3.3: The heat transfer coefficient between the casting and the inserts versus gap width, measured in permanent mold casting [11, 23-25, 57]

3. 5 Initial conditions

The initial temperature of the casting (molten metal injection temperature) is a very important factor, which affects the temperature history and hence affects the final part distortion and stresses. The pouring temperature of aluminum alloy 380 equals to 615-700^{o}C [58]. To depict the effect of the part initial temperature quantitatively, three different initial temperatures were used in the model as given in Table 3.4. Level A was selected to be just above the liquidus temperature (i.e. 593^{o}C). Levels B & C were selected to cover the working temperature range. The initial temperature of the other machine parts was imported from the thermal steady state analysis that was explained before in section 3.2.1.

Level	Part initial temperature (^{o}C)
A	600
B	650
C	700

Table 3.4: Levels for the effect of part initial temperature

3.6 Material properties

Accurate definition of material properties in the model is one of the important keys for reliable results. This includes both the physical and mechanical properties. For the casting material used in the simulation (i.e. aluminum alloy 380) most of properties are temperature dependent especially at elevated temperatures. This temperature dependency was considered in our model. The main problem was the unavailability of material properties data for the aluminum 380 alloy at high temperatures (over 200^{o}C). For this case we were able to use another aluminum alloy which is close in composition to aluminum alloy 380. This alloy contains 7.5%Si & .4%Mg and 92.1% Al. The composition of aluminum alloy 380 is shown in Table 3.5 [33]. Table 3.6 summarizes the physical properties used in the model to represent the casting material.

Component	Wt. %	Component	Wt. %	Component	Wt. %
Al	80.05 - 89.5	Mg	Max 0.1	Si	7.5-9.5
Cu	3.0 – 4.0	Mn	Max 0.5	Sn	Max. 0.35
Fe	Max 2.0	Ni	Max 0.5	Zn	Max. 3.0

Table 3.5: The composition of aluminum alloy 380 [33]

Temperature (C)	25	450	538	539	593	594
Density (Kg/m^3)	2760	2760	2660	2660	2460	2460
Thermal expansion Coefficient*	2.2E-05	2.2E-05	2.2E-05	4.0E-05	4.0E-05	2.2E-05
Thermal Conductivity (W/mK)	109					
Specific heat (J/KgK)	963					
Latent heat (KJ/kgK)	389					
Solidius temperature (^oC)	538					
Liquidius temperature (^oC)	593					

Table 3.6: The physical properties of aluminum alloy 380 used in the model [33 - 36]

*The value of thermal expansion coefficient as a function of temperature was modified to avoid sudden change at the start and end of mushy zone. This sudden change causes convergence problems.

The yield strength and modulus of elasticity are available for aluminum alloy 380 for temperatures up to 200^{o}C [33, 36]. Figure 3.6 shows the stress-strain curve for aluminum alloy 380 at 25^{o}C, 100^{o}C and 200^{o}C [36]. At temperatures over 200^{o}C, we used the mechanical properties of aluminum alloy (7.5%Si, 0.4% Mg); shown in Figure 3.7 [35]. Table 3.7 summarizes the mechanical properties used in the model to represent the casting material. Poisson's ratio was increased with temperature as shown in Table 3.7.

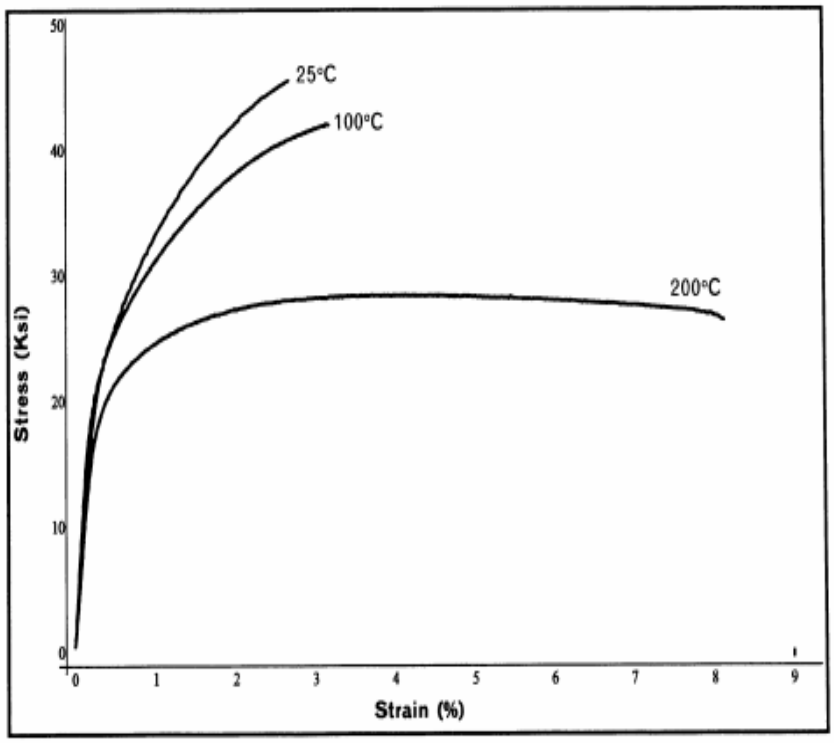

Figure 3.6: Stress-strain curves for aluminum alloy 380 at different temperatures [36]

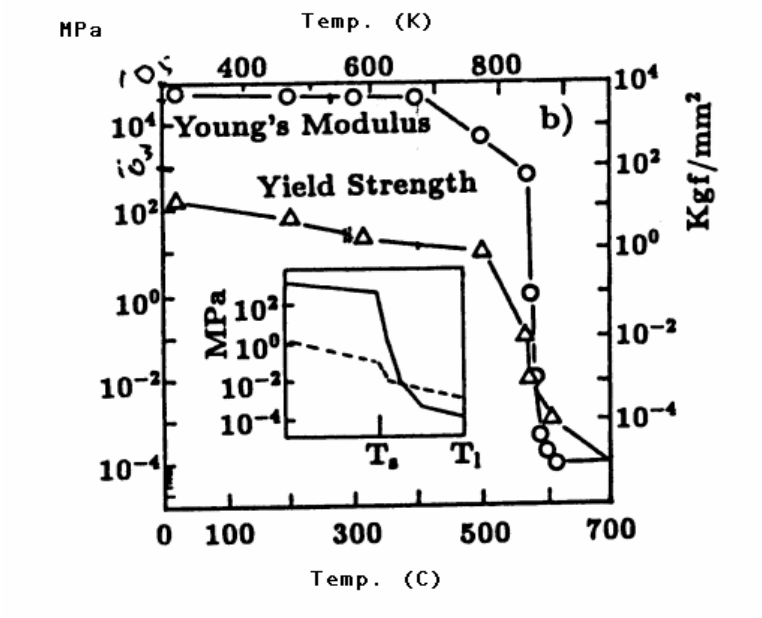

Figure 3.7: Yield strength and modulus of elasticity of al. alloy (7.5% Si, 0.4% Mg) versus temperature [35]

Temperature (^oC)	Modulus of Elasticity (MPa)	Yield Strength (MPa)	Poisson's ratio
25	70000	159	0.33
100	70000	159	0.33
200	64000	130	0.37
300	56500	80	0.39
400	5000	40	0.41
480	500	40	0.42
530	50	40	0.43
538	30	40	0.44
594	10*	40*	0.45

Table 3.7: Values of modulus of elasticity, yield strength and Poisson's Ratio of aluminum alloy 380 versus temperature (35, 36)

* At liquid state the modulus of elasticity and yield strength are approximately equal to zero, but due to convergence problems the values given in Table 3.8 were used.

Properties of H13 steel was used to represent the inserts, while properties of AISI 4140 steel were used to represent the dies and platens. For both steels all material properties, except the specific heat, was assumed to be constant over the expected temperature range. Table 3.8 shows the material properties for AISI H13 & AISI 4140 steels. The specific heat of both steel types versus temperature is shown in Table 3.9.

Material Property	AISI H13	AISI 4140
Modulus of elasticity (Gpa)	206.8	206.8
Poisson ratio	0.29	0.29
Density (Kg/m^3)	7820	7820
Thermal expansion coefficient	$1.17*10^{-5}$	$1.17*10^{-5}$
Thermal conductivity (W/m.K)	29	40

Table 3.8: AISI H13 and AISI 4140 steels material properties [33]

Temperature (C)	Specific heat of AISI H13 (J/Kg)	Specific heat of AISI 4140 (J/Kg)
23	459	473
200	518	473
400	587	519
600	726	561
700	905	N/A
800	885	N/A
900	747	N/A
1000	733	N/A

Table 3.9: AISI H13 and AISI 4140 steels specific heat values versus temperature [33]

3.7 Material Model

Most of the available commercial finite element packages allow the user to select the material model that fits his/her application. Several material models are being used to describe the behavior of the casting, and the accuracy of the results will differ consequently. In this research, and for the sake of comparison, we used three material models. These were *linear elastic*, *elastic-plastic* and *linear elastic-viscoplastic*.

By *elastic* analysis it is meant that the elastically deformed part can retain its initial (undistorted) shape after complete removal of the loads. Figure 3.8 shows a typical stress strain curve for a *linear elastic* model. Elastic analysis was used to model solidified parts in casting processes by several researchers [28, 55 and 56]

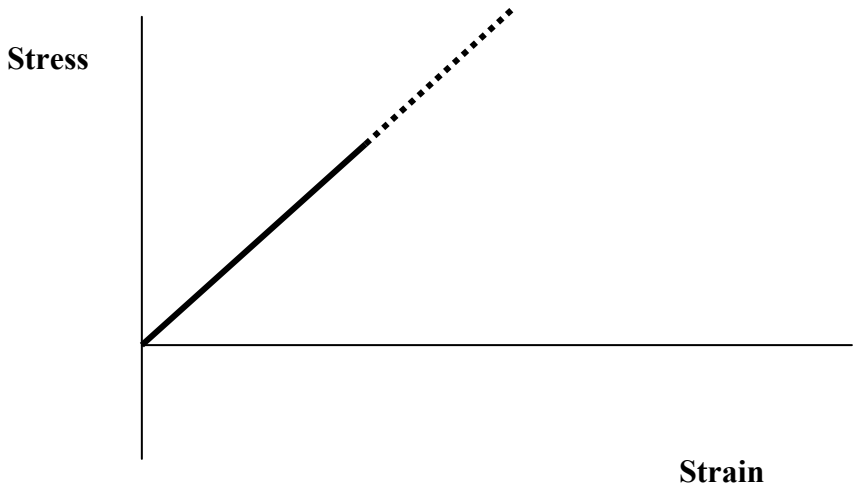

Figure 3.8: A typical stress-strain curve for linear elastic material model

In the *elastic-plastic* analysis, the deformation consists of two parts, elastic and plastic. The elastic part of deformation is completely removed upon removing the applied loads, while the plastic part of deformation is permanent. Elastic-plastic material model have been widely used in casting modeling [30, 35, 46 and 47].

Two elastic-plastic models were used in the analysis. The first one was the *linear elastic-perfect plastic* model, where the yield strength does not change with the value of applied strain. The second one was the *linear elastic-plastic model with isotropic strain hardening*, where the yield strength was a function of applied strain. Figures 3.9 and 3.10 show typical stress strain curves for the two models.

Three levels were given to the value of yield strength to explore its effect on the results. In level A, the yield strength was a function of temperature, and its values are given in Table3.10. In level B, the yield strength was constant and equals to the room

temperature value (i.e. 159MPa) which is the maximum value in level A. The yield strength in level C was constant and equal to the average of the yield strength values in level A over the temperature range (i.e. 88 MPa). This value is very close to the median value of yield strength which equals to 80 MPa. These levels are summarized in Table 3.10.

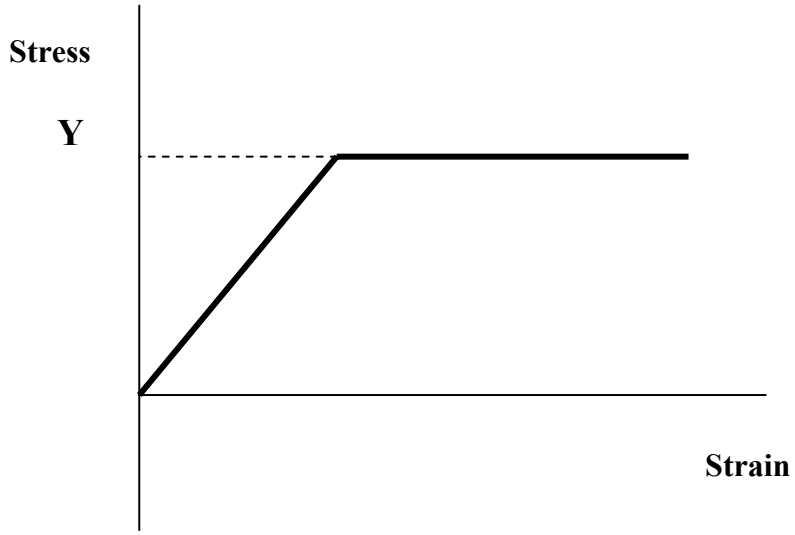

Figure 3.9: A typical stress-strain curve for “linear elastic-perfect plastic” material model

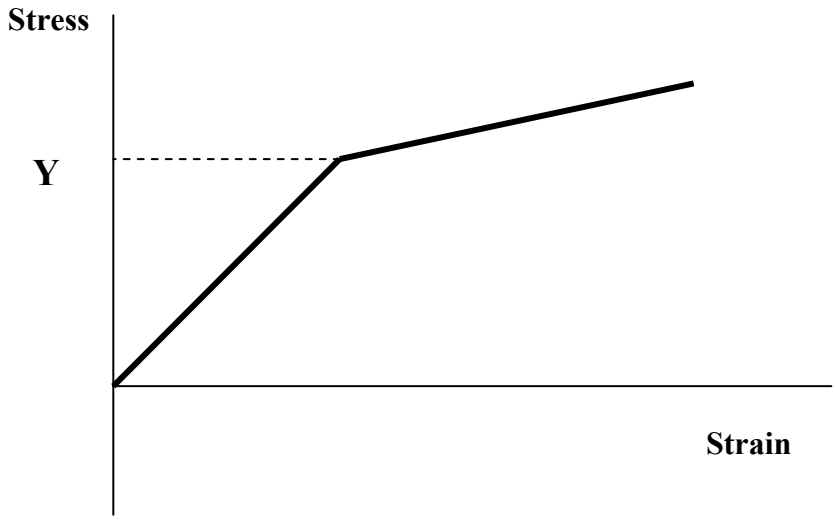

Figure 3.10: A typical stress-strain curve for linear elastic-plastic with isotropic strain hardening

Level	Yield strength
A	Variable, Table 3.5
B	Constant and equals to 159 MPa
C	Constant and equals to 88 MPa

Table 3.10: Levels for yield strength of aluminum alloy 380

To investigate the effect of strain hardening on the model, three level of strain hardening were given in different runs, as given in Table 3.11. In level A there is no strain hardening, and the yield strength values are as given in Table 3.9. The yield strength was given as a function of temperature and strain for Levels B & C. Tables 3.12 & 3.13 show the yield strength values for both levels as a function of temperature and strain. There is not much information about the strain hardening of aluminum alloys, and the given values in Tables 3.12 & 3.13 are hypothetical values which are used to demonstrate the strain hardening effect on the final part.

Level	Effect of strain hardening on yield strength
A	No strain hardening
B	Small effect: Table 3.10
C	Big effect: Table 3.11

Table 3.11: Levels for the effect of strain hardening on yield strength of aluminum alloy 380

Temperature (C)	Strain (%)	Yield Strength (MPa)	Temperature (C)	Strain (%)	Yield Strength (MPa)
25	0.0	159	300	0.0	80
	0.02	161		0.02	82
	0.04	163		0.04	84
	0.06	165		0.06	86
	0.08	167		0.08	88
	0.1	169		0.1	90
100	0.0	159	400	0.0	40
	0.02	161		0.02	42
	0.04	163		0.04	44
	0.06	165		0.06	46
	0.08	167		0.08	48
	0.1	169		0.1	50
200	0.0	130	600	0.0	40
	0.02	132		0.02	42
	0.04	134		0.04	44
	0.06	136		0.06	46
	0.08	138		0.08	48
	0.1	140		0.1	50

Table 3.12: Yield strength values for aluminum alloy A380 with **low** strain hardening effect

Temperature (C)	Strain (%)	Yield Strength (MPa)	Temperature (C)	Strain (%)	Yield Strength (MPa)
25	0.0	159	300	0.0	80
	0.02	169		0.02	90
	0.04	179		0.04	100
	0.06	189		0.06	110
	0.08	199		0.08	120
	0.1	209		0.1	130
100	0.0	159	400	0.0	40
	0.02	169		0.02	50
	0.04	179		0.04	60
	0.06	189		0.06	70
	0.08	199		0.08	80
	0.1	209		0.1	90
200	0.0	130	600	0.0	40
	0.02	140		0.02	50
	0.04	150		0.04	60
	0.06	160		0.06	70
	0.08	170		0.08	80
	0.1	180		0.1	90

Table 3.13: Yield strength values for aluminum alloy A380 with **high** strain hardening effect

In the *linear elastic-viscoplastic* material model, the stress strain relation depends on both the strain rate and the strain value. Figure 3.11 shows a typical stress-strain curve for *linear elastic-viscoplastic* model. The use of this model is increasing noticeably due to the marvelous advances in the computational powers for relatively low cost. The main problem that faces this type of analysis is the unavailability of accurate description of thermal and mechanical governing equations at a particular situation [27]. Several researchers have used elastic-viscoplastic model to describe casting process [18, 27, 29, 44, 45 and 57].

The hyperbolic-sine constitutive law was used to describe the creep behavior of the casting. This constitutive law was used successfully in previous research for modeling pure aluminum casting in continuous casting [29]. The constitutive equation is given in the next section. Unfortunately, the aluminum alloy mechanical properties that are needed for this constitutive law, are not available and hence the material constants of pure aluminum, shown in Table 3.13, were used [29].

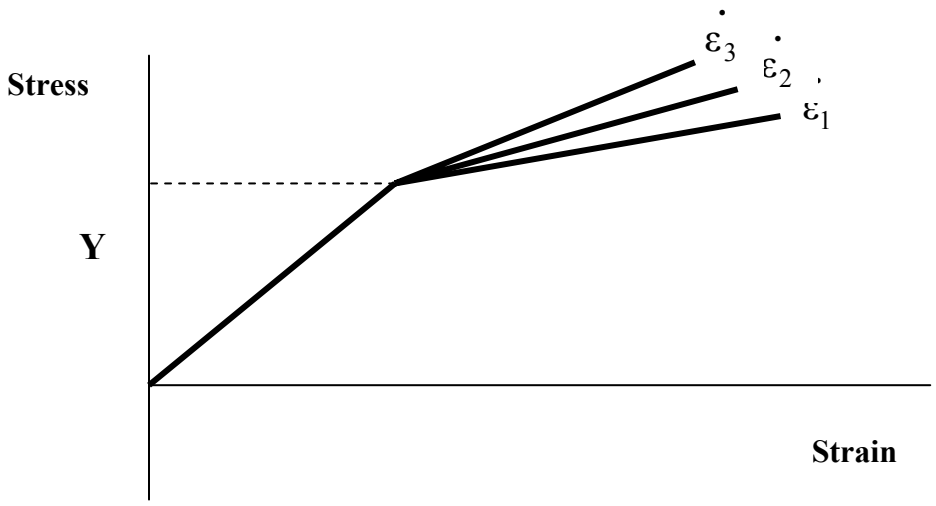

Figure 3.11: A typical stress-strain curve for “linear elastic-viscoplastic” material model

Variable	Value
A	0.382E12
B	0.037E-6
C	18849
n	3.84

Table 3.14: Values represent creep effect in the *linear elastic-viscoplastic* model [29]

3.8 Governing Equations

The casting model simulation involves thermal and stress analysis. The thermal analysis requires solving the energy balance equation (2). This equation must be solved for the casting and the mold to find the temperature history at every point in the casting, T[x,y,z,t].

$$\frac{\partial}{\partial x}\left(K_x \frac{\partial T}{\partial x}\right)+\frac{\partial}{\partial y}\left(K_y \frac{\partial T}{\partial y}\right)+\frac{\partial}{\partial z}\left(K_z \frac{\partial T}{\partial z}\right)+Q=\rho C_p\left(\frac{\partial T}{\partial t}+V_x \frac{\partial T}{\partial x}+V_y \frac{\partial T}{\partial y}+V_z \frac{\partial T}{\partial z}\right) \qquad (2)$$

Where:

K = Thermal conductivity

C_p = Specific heat

ρ = Density

Q = Heat source (including the latent heat)

V_x = Flow velocity in X direction

V_y = Flow velocity in Y direction

V_z = Flow velocity in Z direction

According to our assumptions, the molten metal flow was not considered; therefore all velocity terms are equal to "zero". The very small variation of the spatial terms – at the right hand side of equation (2) – justifies this approximation. We also assume an isotropic material; i.e. material properties are not position dependent. In the simulation the latent heat was assumed to be released linearly between solidus and liquidus temperatures. Under these assumptions equation 1 is simplified to equation (3):

$$\frac{\partial^2 T}{\partial x^2} + \frac{\partial^2 T}{\partial y^2} + \frac{\partial^2 T}{\partial z^2} + Q = \rho C_p \frac{\partial T}{\partial t} \tag{3}$$

The previous equations take care of the thermal analysis. For the stress analysis there are three types of equations that must be solved [5, 6]. First, the mechanical equilibrium equations, which relates the incremental applied forces to the resulted incremental stresses, second, the compatibility equations, which govern the incremental strains with incremental displacements and third, the constitutive equations that relate the incremental stresses and incremental strains.

These equations depend on the material behavior. For the linear elastic model the mechanical equilibrium equations, the compatibility equations and the constitutive equations are given by equations 4, 5& 6 respectively.

$$[L]^T \Delta\sigma = \Delta F \tag{4}$$

$$\Delta\varepsilon = [L]\,\Delta u \qquad (5)$$

$$\Delta\sigma = [D]\,\varepsilon_e \qquad (6)$$

Where:

$$[\mathbf{L}] = \begin{bmatrix} \partial/\partial x & 0 & 0 \\ 0 & \partial/\partial y & 0 \\ 0 & 0 & \partial/\partial z \\ \partial/\partial y & \partial/\partial x & 0 \\ 0 & \partial/\partial z & \partial/\partial y \\ \partial/\partial z & 0 & \partial/\partial x \end{bmatrix}$$

$\Delta\sigma = \{\Delta\sigma_x, \Delta\sigma_y, \Delta\sigma_z, \Delta\tau_{xy}, \Delta\tau_{yz}, \Delta\tau_{zx}\}$ is the incremental stress.

$\Delta\varepsilon = \{\Delta\varepsilon_x, \Delta\varepsilon_y, \Delta\varepsilon_z, \Delta\gamma_{xy}, \Delta\gamma_{yz}, \Delta\gamma_{zx}\}$ is the incremental strain.

$\Delta F = \{\Delta F_x, \Delta F_y, \Delta F_z\}$ is the external force increments.

$\Delta u = \{\Delta u_x, \Delta u_y, \Delta u_z\}$ is the displacement increments.

The incremental total strain vector, $\Delta\varepsilon$, is given by the following equation:

$$\Delta\varepsilon = \Delta\varepsilon_e + \Delta\varepsilon_t \qquad (7)$$

Where:

$\Delta\varepsilon_e$ = the elastic strain increment.

$\Delta\varepsilon_t$ = the thermal strain increment.

$$[\mathbf{D}] = \frac{E}{(1+\nu)(1-2\nu)} \begin{bmatrix} 1-\nu & \nu & \nu & 0 & 0 & 0 \\ \nu & 1-\nu & \nu & 0 & 0 & 0 \\ \nu & \nu & 1-\nu & 0 & 0 & 0 \\ 0 & 0 & 0 & (1-2\nu)/2 & 0 & 0 \\ 0 & 0 & 0 & 0 & (1-2\nu)/2 & 0 \\ 0 & 0 & 0 & 0 & 0 & (1-2\nu)/2 \end{bmatrix}$$

Adding the inelastic part of the constitutive equation modifies equation 7 to the form of equation 8 [26]:

$$\Delta\varepsilon = \Delta\varepsilon_e + \Delta\varepsilon_t + \Delta\varepsilon_{pl} + \Delta\varepsilon_c \qquad (8)$$

Where:

$\Delta\varepsilon_{pl}$ = The plastic strain increament

$\Delta\varepsilon_c$ = The creep strain increament

The plastic strain rate is calculated using equation 9, and the creep strain rate is calculated using equation 10:

$$\dot{\bar{\varepsilon}}_{pl} = D\left(\frac{\bar{\sigma}}{\sigma\circ} - 1\right)^p \quad \text{for } \bar{\sigma} \geq \sigma\circ \qquad (9)$$

Where :

$\dot{\bar{\varepsilon}}_{pl}$ = The equivalent plastic strain rate

$\bar{\sigma}$ = The yield strenght at non - zero plastic strain rate

$\sigma\circ$ = The static yield strength

D & p are material constants

$$\dot{\varepsilon}_c = \frac{3}{2}\frac{A(\sinh B\bar{\sigma})^n}{\bar{\sigma}}\exp\left(-\frac{C}{T+273}\right)S \qquad (10)$$

Where:

$\dot{\varepsilon}_c$ = the inelastic strain rate

$\bar{\sigma} = \frac{3}{2}\sqrt{S.S}$ = *the* effective stress

S = The deviatoric stress

T = Temperature (^oC)

A,B, C and n, material constants.

CHAPTER 4

SIMULATION RESULTS

The simulation model was run first using the three material models, elastic, elastic-plastic and elastic-viscoplastic. These models are explained briefly in Chapter 3. A comparison between the simulation results using the three material models is given in the first section of this chapter. The comparison includes the differences in ejection temperature, residual stresses and casting distortion patterns.

Using the second model –i.e. the elastic-plastic-model- a *Design of Experiment (DOE)* was conducted to evaluate the effect of four modeling parameters. The elastic-plastic model was selected to avoid problems with the elastic and visco-plastic models. More details on the reasons for using the elastic-plastic model for the DOE are given in section 4.2.

An experimental work was conducted to validate and verify the simulation model results. The experimental measurements were categorized as machine related measurements and casting related measurements. In the third section of this chapter a comparison between the casting measurements and the simulation predictions is presented. Details about the experimental work and the machine related measurements are given in Chapter 5.

4.1 Material Model Comparison

4.1.1 Casting Ejection Temperature

Cycle time is one of the most important factors for die casters. Shorter cycle time means more productivity and hence more profit. The cycle time is estimated to be enough to allow the casting to solidify and cool down to a temperature where the strength of the part is high enough to withstand the ejection and trimming loads.

The ejection temperature, hence, is a very important output from the simulation model. The ejection temperature is also one of the important factors that affect the final distortion and stresses in the part. Figure 4.1 shows the temperature distribution in the casting at ejection. As expected there was no difference in the ejection temperature patterns or values among the three material models. Figure 4.1, although resulted from the elastic model, represents also the ejection temperatures from the plastic and viscoplastic models.

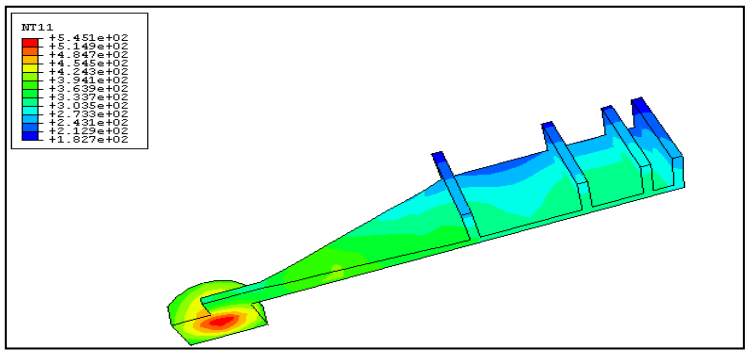

Figure 4.1: Casting ejection temperature, (the elastic material model)

Table 4.1 gives the ejection temperatures in the casting at three locations using the three material models. The locations are given in Figure 4.2. Again the results show no difference between the three material models in the ejection temperature.

Material Model	Location		
	1	2	3
Elastic	277	325	303
Elastic-Plastic	277	325	303
Elastic-Viscoplastic	277	325	303

Table 4.1: Ejection temperatures at different locations in the casting

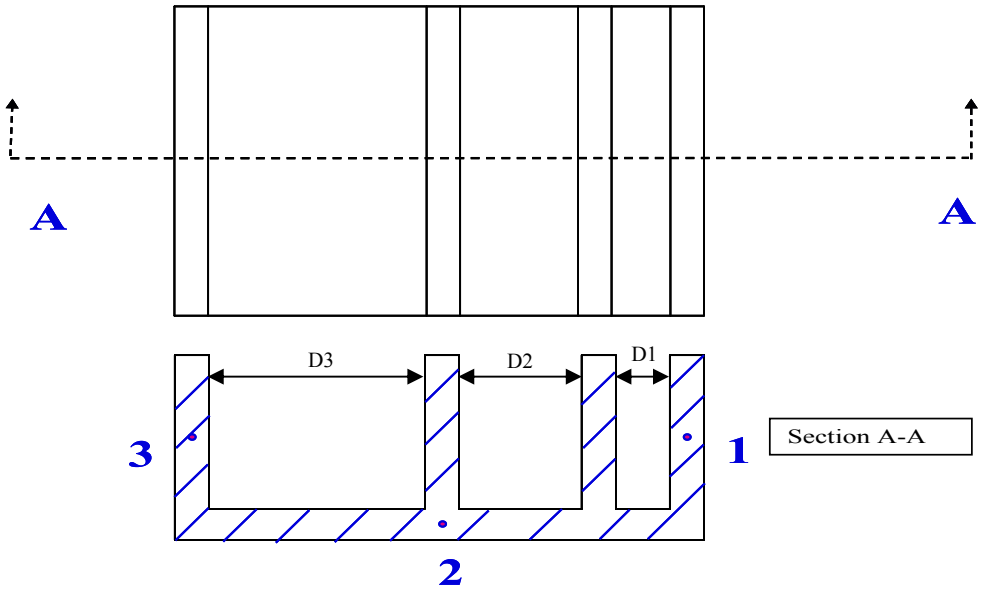

Figure 4.2: Picked locations for ejection temperature and residual stress comparison

Related to the ejection temperature is the gap formation between the casting and the inserts. The gap formation will decrease the heat transfer coefficient between the casting and the inserts, and hence increases the ejection temperature.

Figure 4.3 shows the gap formed between the casting and the inserts instantaneously before ejection using the elastic model. The gap patterns are basically the same in the three material models and Figure 4.3 can represent the gap formation in the other two models also. The gap is formed only on the biscuit and a small area of the runner.

Practically no gap is expected in the biscuit area, since the biscuit is always under pressure by the plunger piston. The gap formed in the biscuit area in the model is an artificial effect of the boundary conditions, since the plunger is not included in the model. This artificial gap on the biscuit surface is a drawback of applying the cavity pressure as a boundary condition on the cavity surface and not as a hydrostatic pressure through the casting. More details about this issue were given in sections 3.1 and 3.3.4.

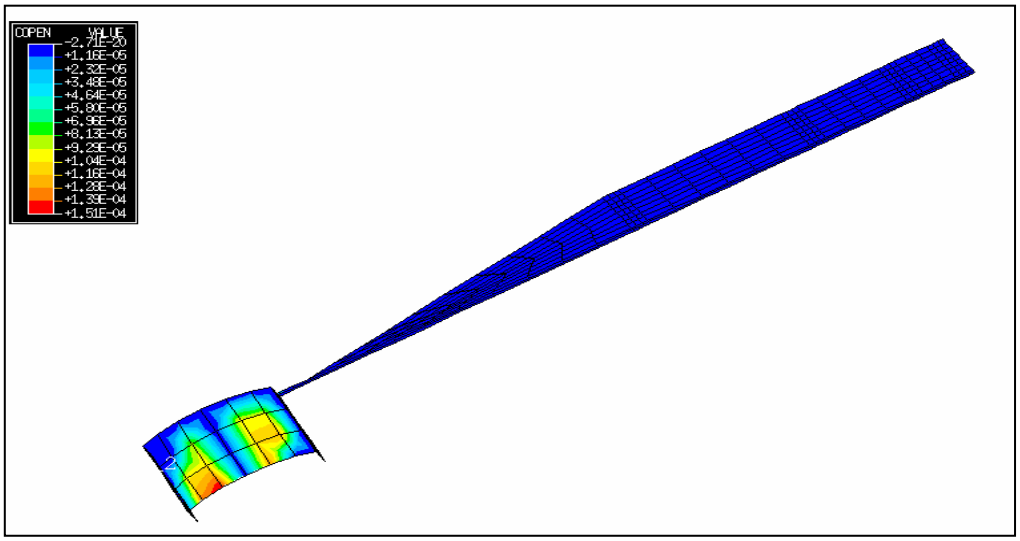

(a)

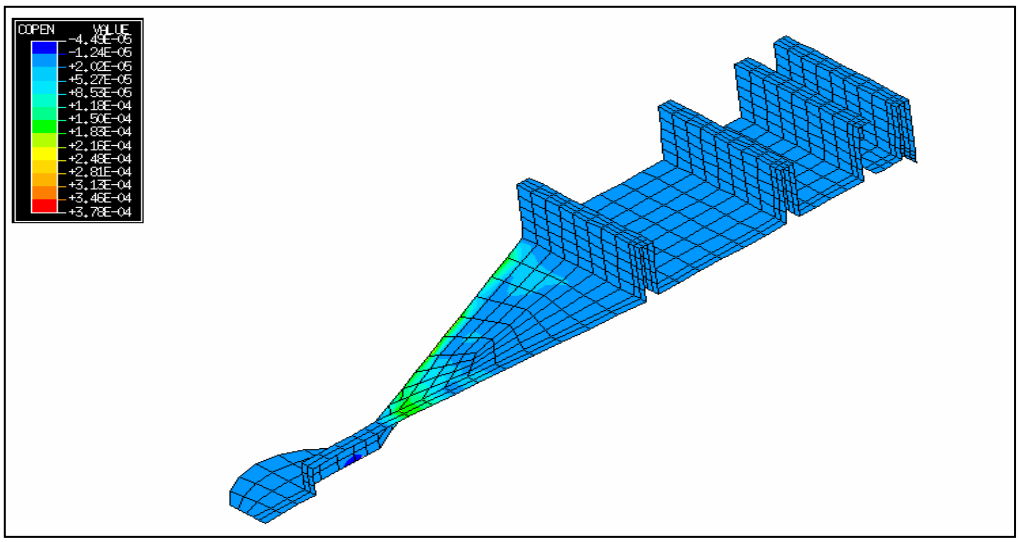

(b)

Figure 4.3: Gap formed between the casting & cover insert (a), and the casting & ejector insert (b), instantaneously before ejection (the elastic material model)

4.1.2 Residual Stresses

Table 4.1 shows the residual Von Mises stresses at room temperature at the locations shown in Figure 4.2. The values in the table demonstrate that the residual stresses are significantly affected by the material model. The stress at room temperature using the elastic model is five to eight times higher than the plastic model which in turn is two to four times higher than the viscoplastic one. These results are expected since adding the plasticity to the material model allows the part to relax both inside and outside the die. The creep property adds another relaxation factor to the part and allows it to relax further and therefore the part ends up with lower residual stresses. The over estimation of stresses given by elastic model is a well known problem and was addressed in literature [27]. Figures 4.4 and 4.5 show the residual stresses at ejection and at room temperature respectively for the tested material models. Figure 4.6 shows the stress history at the three locations given in Figure 4.2 starting at injection and ending at room temperature.

Material Model	At ejection			At room temperature		
	1	2	3	1	2	3
Elastic	78	150	85	566	383	545
Elastic-Plastic	23	27	10	61	43	47
Elastic-Viscoplastic	6	6	6	22	25	17

Table 4.2: Residual Von Mises stresses (MPa) at ejection and room temperature at locations 1, 2 and 3 shown in Figure 4.2

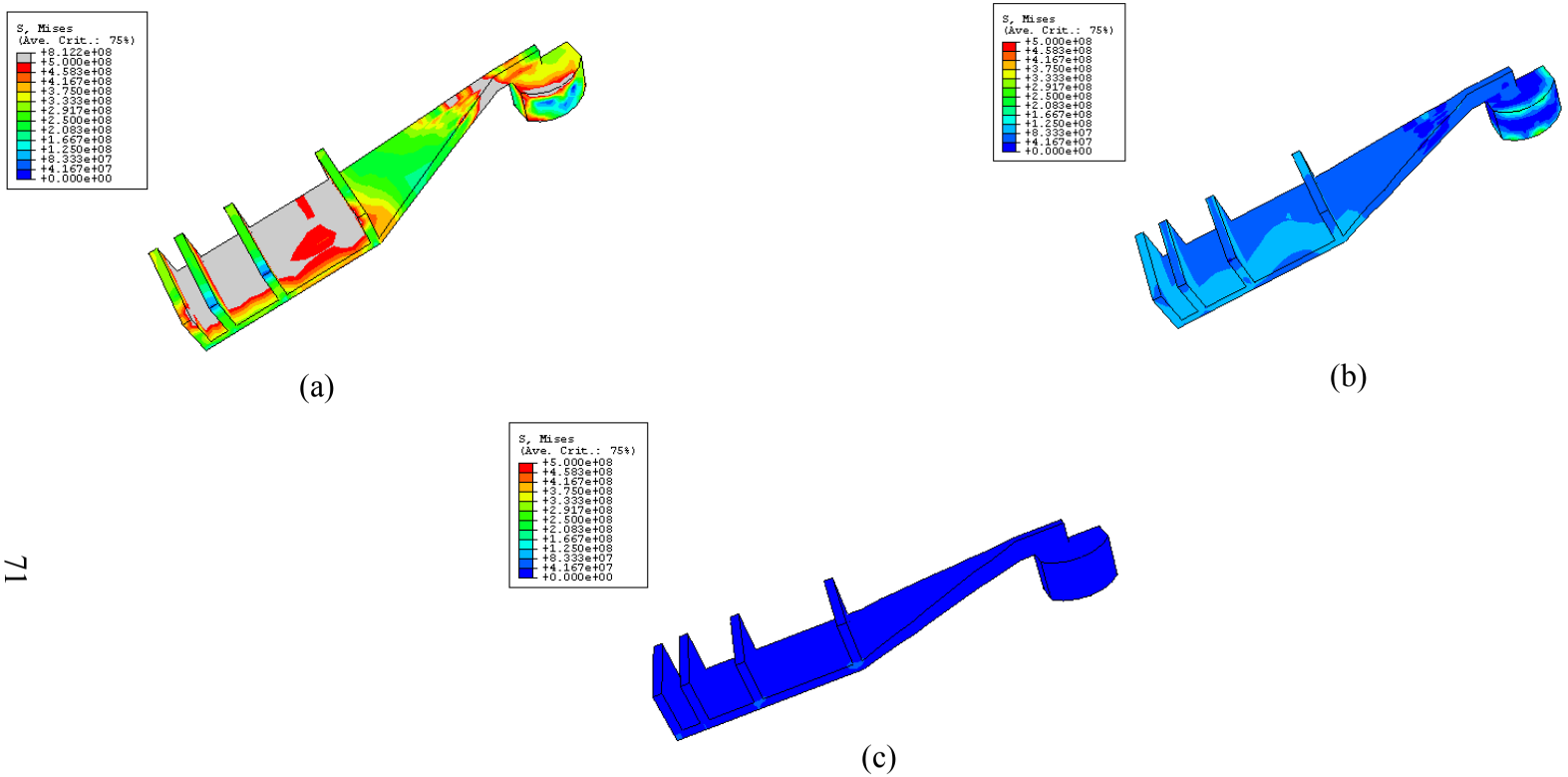

Figure 4.4: Residual Von Mises stresses in the casting at ejection for elastic model (a), elastic-plastic model (b) and elastic-viscoplastic model (c), using the same scale

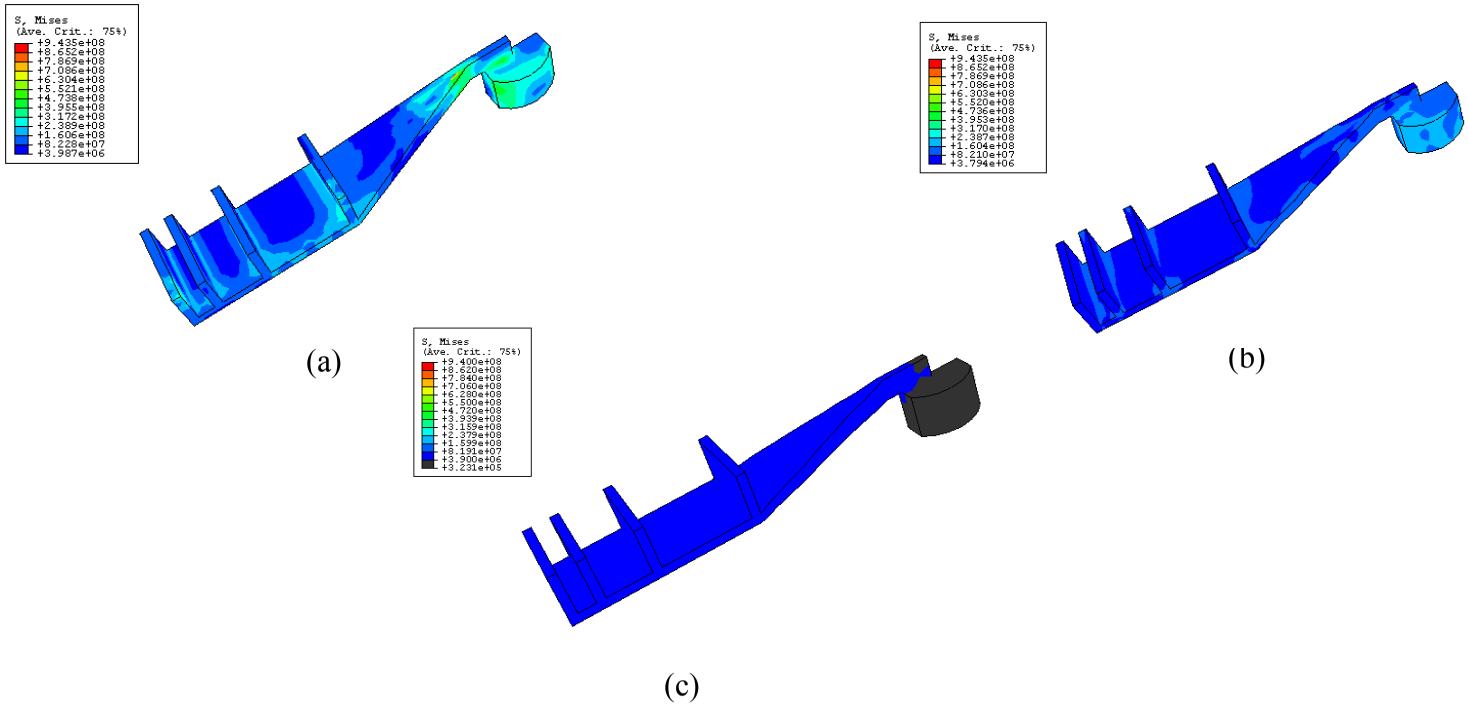

Figure 4.5: Residual Von Mises stresses in the casting at room temperature for elastic model (a), elastic-plastic model (b) and elastic-viscoplastic model (c), using the same scale

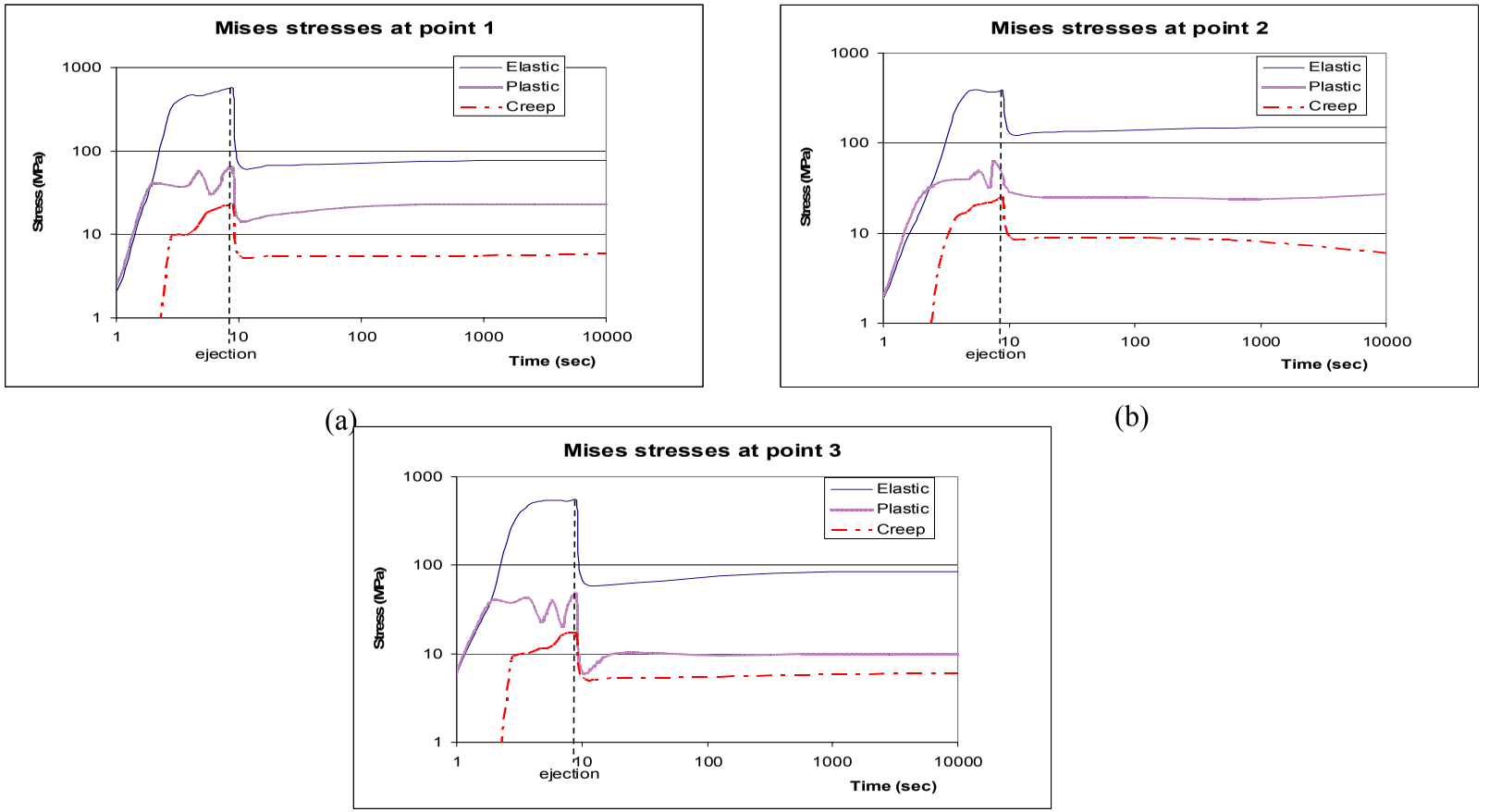

Figure 4.6: Stress history at three locations in the casting using the elastic, elastic-plastic and elastic-viscoplastic models at locations 1 (a), 2 (b) and 3 (c) defined in Figure 4.2

The stress history at the three locations has basically the same trend. The stresses starts at zero at the beginning of the simulation, then with solidification and cooling the stresses start to build up till it reaches its maximum value before ejection. At ejection the stresses in the casting release quickly then start to increase very slowly till the casting reaches the room temperature. The effect of yielding is obvious in the wavy pattern of the elastic-plastic curves.

From Figure 4.6 it is clear that the elastic material model always predicts higher stresses than the elastic-plastic model, which in turn is higher than the elastic-viscoplastic model. It is also noticeable that, despite which model is used, the stresses at ejection are significantly higher than the stresses at room temperature. This proves that restriction the casting inside the die is the main source of stresses. This information was addressed before in the literature [5]

4.1.3 Part Distortion

The distortion patterns of the three models are very similar at ejection. Figure 4.7 shows the distortion pattern of the casting at ejection using the elastic material model. The figure can also represent the other two material models. The figure shows that the distortion inside the die is trivial. The red color shows the original casting shape (i.e. before any distortion), while the white color shows the final casting shape. The difference between the original and final shapes of the casting is due to the shrinkage. Recalling the gap predications, Figure 4.3, we can conclude that the thermal growth of the die is almost the same as the thermal shrinkage of the casting. The wavy shape of the runner is clearly an artificial effect of a coarse mesh rather than a result of distortion.

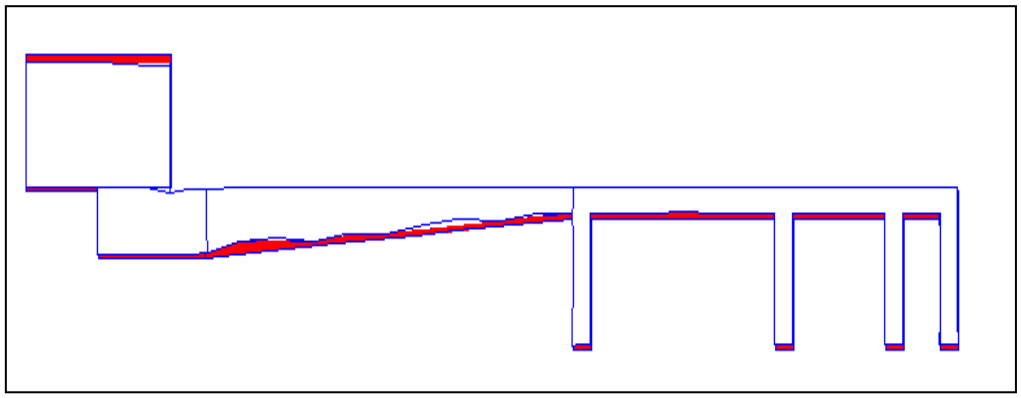

Figure 4.7: Distortion pattern in casting at ejection

Figures 4.8-4.10 show the distortion patterns in the casting at room temperature for the elastic, elastic-plastic and elastic-viscoplastic material models respectively. Figures 4.9 and 4.10 demonstrate that there is no difference between the distortion patterns resulting from the plastic and viscoplastic models. Figure 4.8 shows a slight difference in the distortion at the back of the casting, while the other parts did not show a significant difference.

The distances between fins were measured to quantitatively compare the results from the three models. Figure 4.2 shows the measured dimensions which are D1, D2 and D3. Details of measuring these dimensions are given later in section 4.2.3. Table 4.3 shows the dimensions D1, D2 and D3 at ejection and at room temperature. The solid model dimensions for D1, D2 and D3 are 10.16, 25.4 and 50.8 mm respectively.

Material Model	Dimension D1		Dimension D2		Dimension D3	
	At ejection	At room temperature	At ejection	At room temperature	At ejection	At room temperature
Elastic	10.187	10.106	25.435	25.165	50.826	50.330
Elastic-Plastic	10.179	10.052	25.424	25.188	50.418	50.400
Elastic-Viscoplastic	10.177	10.071	25.421	25.231	50.812	50.492

Table 4.3: Dimensions D1, D2 and D3 at ejection and room temperature (mm)

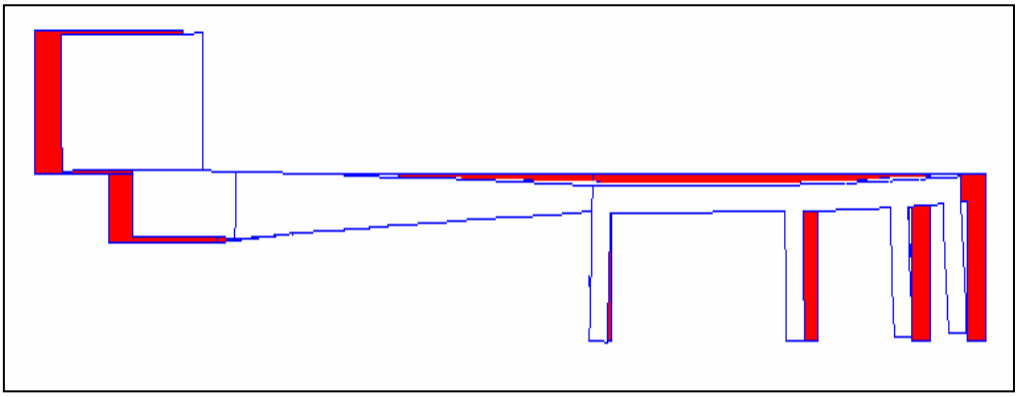

Figure 4.8: Distortion pattern in casting at room temperature, elastic model

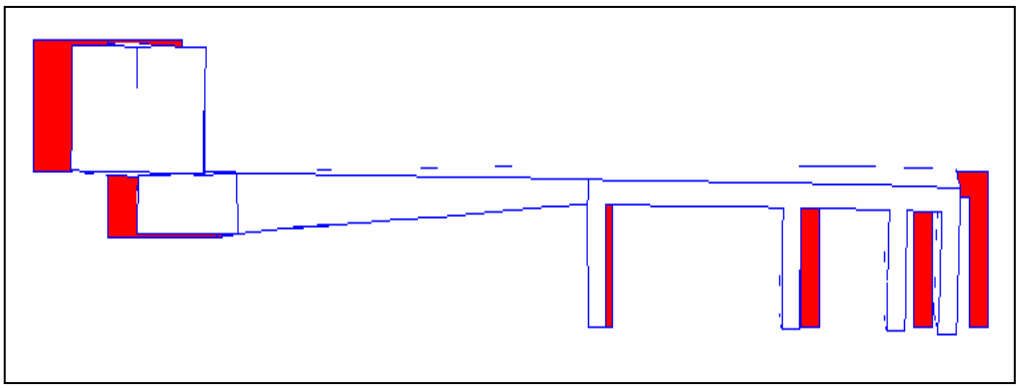

Figure 4.9: Distortion pattern in casting at room temperature, elastic-plastic model

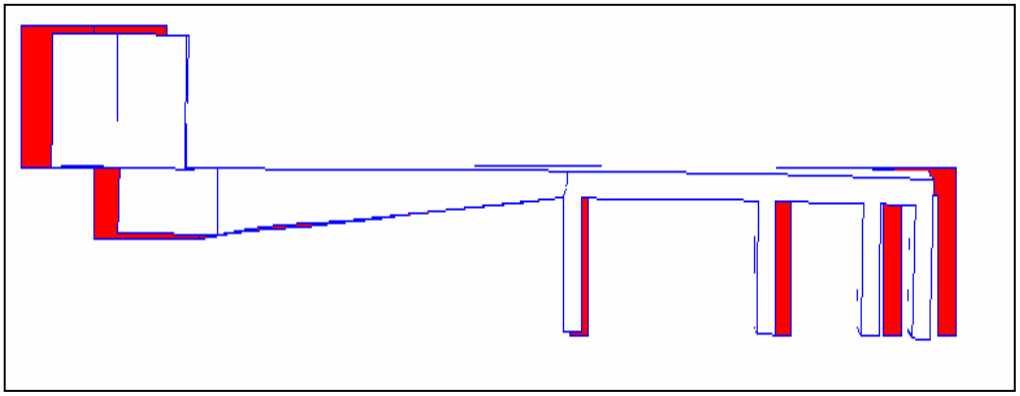

Figure 4.10: Distortion pattern in casting at room temperature, elastic-viscoplastic model

4.2 Design of Experiment

The comparison between the elastic, plastic and visco-plastic models showed that the elastic model exhibits overestimated stresses that may exceed the yield and even the ultimate strength of the casting material, which is not reasonable. On the other hand the visco-plastic model suffers from the lack of material properties data needed to run the model effectively. Also the tractability of the viscoplastic model is very poor. The viscoplastic simulation needed six weeks of continuous run to provide the final results. Recalling that the used viscoplastic material properties were for pure aluminum, and there is no reason to believe that it fits our aluminum alloy, it did not make sense to obtain such a computationally expensive solution with doubtful results.

Due to these reasons the elastic-plastic model was used to investigate the effect of four parameters on predicted results from the simulation model. These parameters are:

- Heat transfer coefficient between casting and inserts (HTC).
- Yield strength value (YS).
- Strain hardening (SH).
- Injection temperature (IT).

Three levels were given to each parameter as explained in Chapter 3. Calculating the degrees of freedom for such an experiment is given in Table 4.4 [59]. For each factor the number of degrees of freedom equals to number of levels for this factor minus one. Table 4.5 shows the orthogonal array that was used to enable efficient determination of the effect of each one of the studied factors [59].

Factor	Degrees of Freedom
Overall mean	1
HTC, YS, SH and IT	4 * (3-2) = 8
Total	9

Table 4.4: Degrees of freedom for the orthogonal array [59]

CASE	HTC	YS	SH	IT
1	A	A	A	A
2	A	B	B	B
3	A	C	C	C
4	B	A	B	C
5	B	B	C	A
6	B	C	A	B
7	C	A	C	B
8	C	B	A	C
9	C	C	B	A

Table 4.5: The orthogonal array [59]

4.2.1 Ejection Temperature

Figure 4.11 shows the main effect plots of the ejection temperature. The plots show that the ejection temperature is only a function of the injection temperature and the heat transfer coefficient between the casting and the inserts. Increasing the injection temperature increases the ejection temperature. Also decreasing the heat transfer coefficient decreases the amount of heat transferred from the casting to the inserts, and hence increases the ejection temperature.

The yield strength and strain hardening did not have any effect on the ejection temperature at the three locations. The only way that these two factors would affect the ejection temperature, is, if they affect the gap width at these three locations. But according to the simulation results described in section 4.1.1, there is no gap in the whole casting area. So it was expected that these two factors do not affect the ejection temperature of the casting.

Figure 4.12 shows the interaction plot of the heat transfer coefficient and the injection temperature at location 1. The parallel lines in the figure exhibit that there is no interaction between them. This is the case also for location 2 & 3.

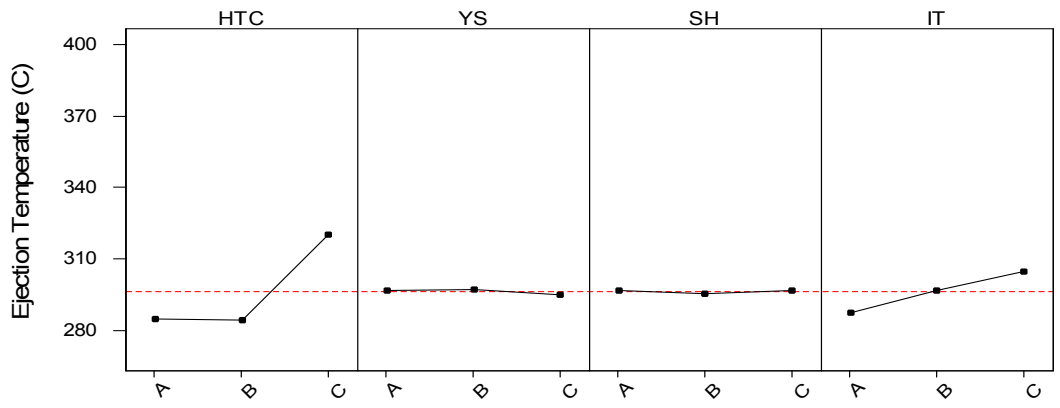

(a)

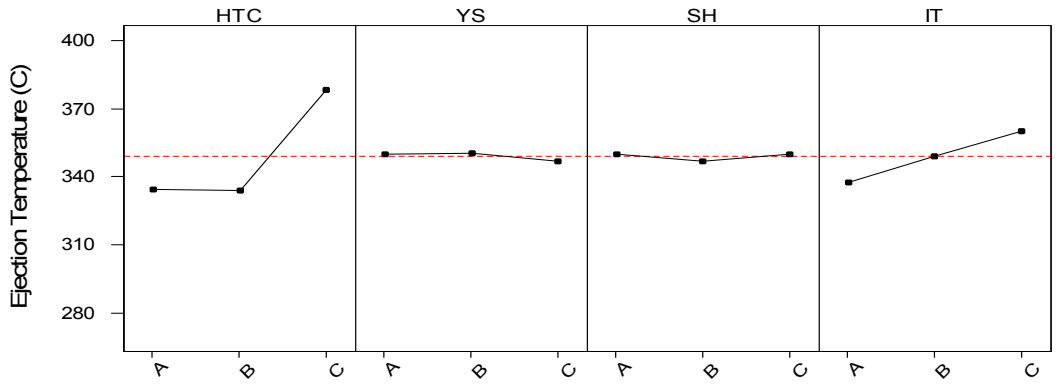

(b)

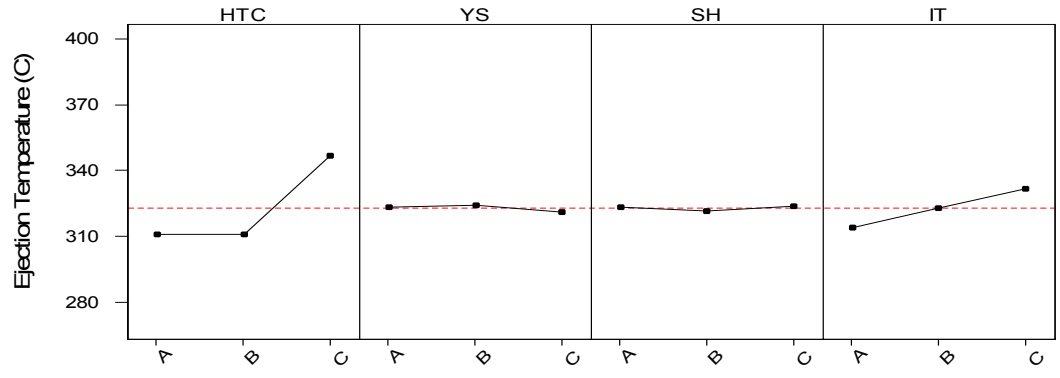

(c)

Figure 4.11: Main effect plots of HTC, YS, SH and IT on the ejection temperature at location 1(a), location 2 (b) and location 3 (c)

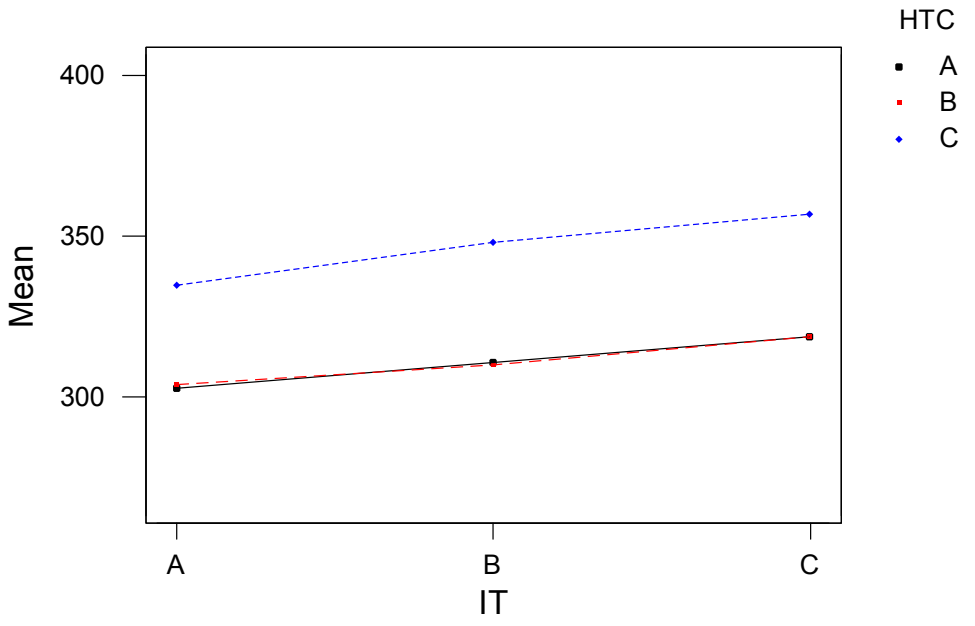

Figure 4.12: Interaction effect plot of HTC & IT (c) on the ejection temperature at location 1

4.2.2 Residual Stresses

Figures 4.13-4.15 show the main effect plot for the four studied factors (heat transfer coefficient (HTC), yield strength (YS), strain hardening (SH) and injection temperature (IT) on the residual stresses at locations 1, 2 and 3 respectively. The main effect plots are given at ejection and at room temperature.

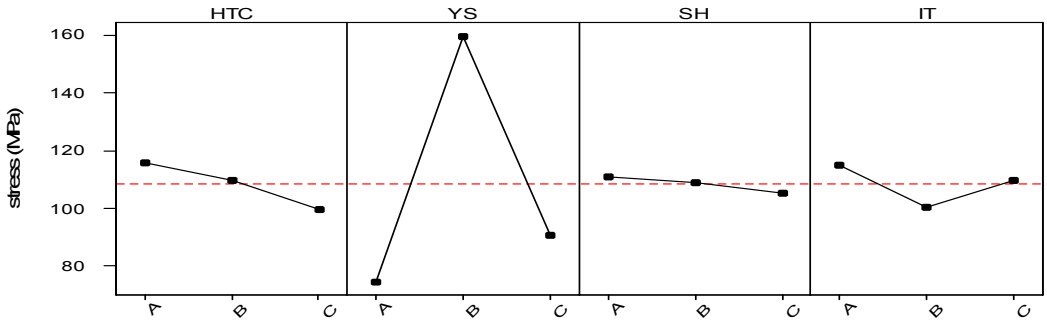

(a)

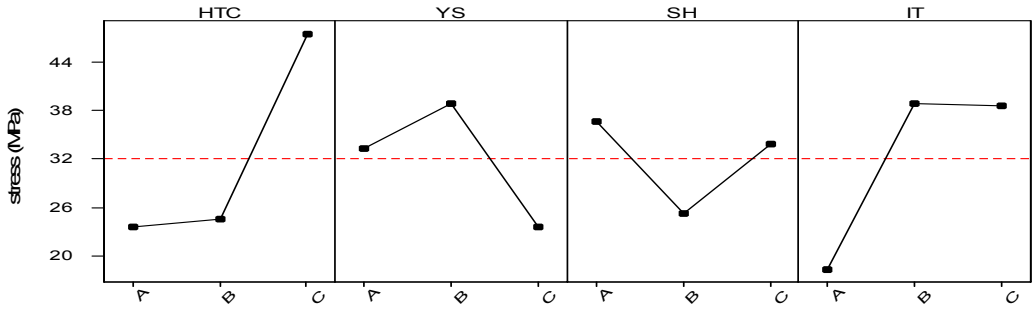

(b)

Figure 4.13: Main effect plot of HTC, YS, SH and IT on residual stresses at location 1, at ejection (a) and at room temperature (b)

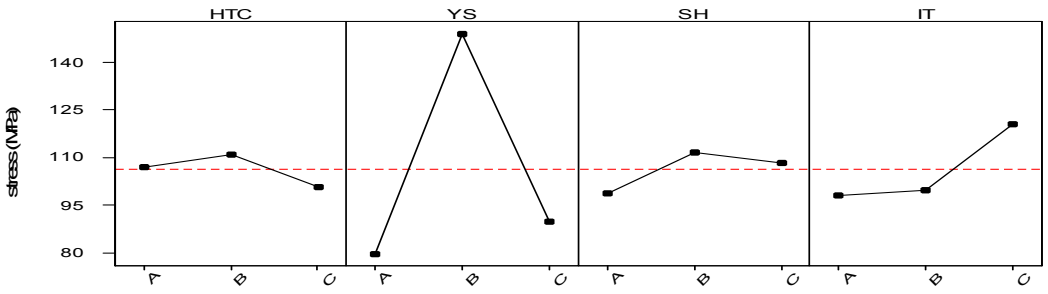

(a)

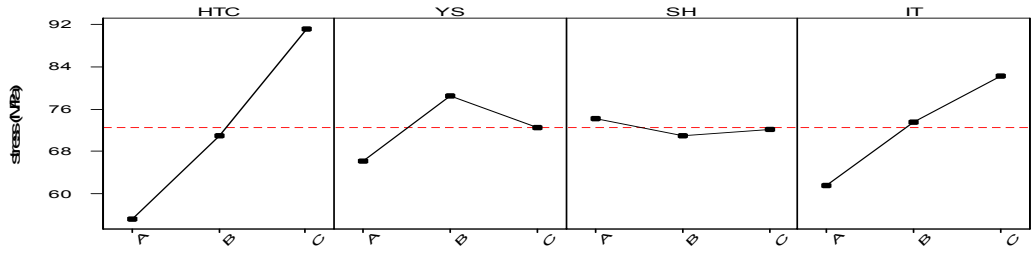

(b)

Figure 4.14: Main effect plot of HTC, YS, SH and IT on residual stresses at location 2, at ejection (a) and at room temperature (b)

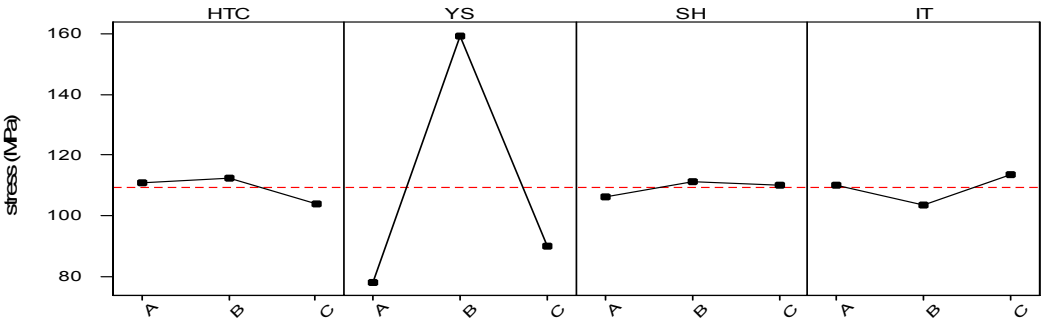

(a)

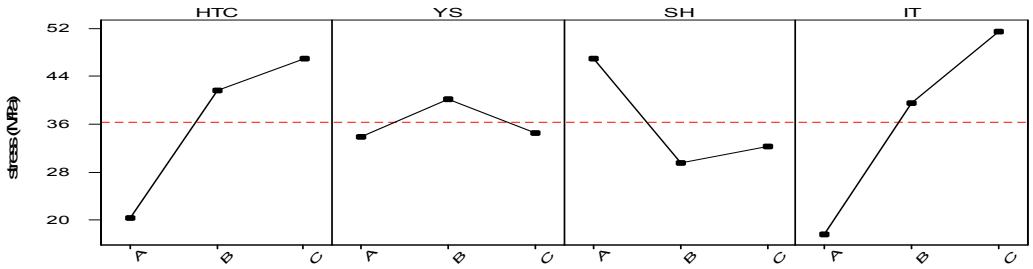

(b)

Figure 4.15: Main effect plot of HTC, YS, SH and IT on residual stresses at location 3, at ejection (a) and at room temperature (b)

Studying Figures 4.13- 4.15 demonstrates that the yield strength had the greatest effect on the residual stresses at ejection, while the effects of the other factors were not significant. The high yield strength (level B) resulted in the highest residual stresses at ejection at the three locations. While the variable yield strength (level A) and the constant average value of yield strength (level C) resulted in very close ejection stresses. The strain hardening, although related to yield strength, did not have any effect on the stresses at ejection. The reason is that inside the die the strains were very low and strain hardening was not effective.

At room temperature, the residual stresses results do not make the same clear sense. While it was expected that the yield strength would have greatest effect, it did not. The heat transfer coefficient and the injection temperature were the main sources of variability in the stress results. Generally the higher injection temperature resulted in higher stresses. This is reasonable, since the more heat content leads to more thermal stresses. The yield strength effect pattern worked in a similar pattern to the stresses at ejection, but with smaller effect. At room temperature the strain hardening had some effect at location 1 & 3. The greatest effect came from the heat transfer coefficient which was not expected. Generally the lower heat transfer coefficient ended with a higher residual stress. At ejection the heat transfer coefficient had a small effect on the results with a trend that was opposite to the one at room temperature. The expected reason for these unexpected results is the plastic relaxation of stresses after ejection. The cases that were ejected with stresses higher than the yield strength relaxed instantaneously and lost most of the stresses, while the cases that was ejected with stresses lower than the yield strength, did not relax and started to build up thermal stresses upon ejection. The

relaxation resulted in the higher stresses at ejection leading to the lower stresses at room temperature. This was an artifact of the stress-strain curves that had a sharp transition between the elastic and plastic regions. The conclusion is that very smooth transitions in stress-strain curves are required rather than sharp transitions that were used in this model.

Figure 4.16 plots the interaction between the yield strength and both the heat transfer coefficient and the injection temperature. The figure shows a significant interaction between the yield strength and the heat transfer coefficient (particularly at level C). The figure also shows a significant interaction between the injection temperature and the yield strength. The DOE needs to be modified to include the interactions between the factors.

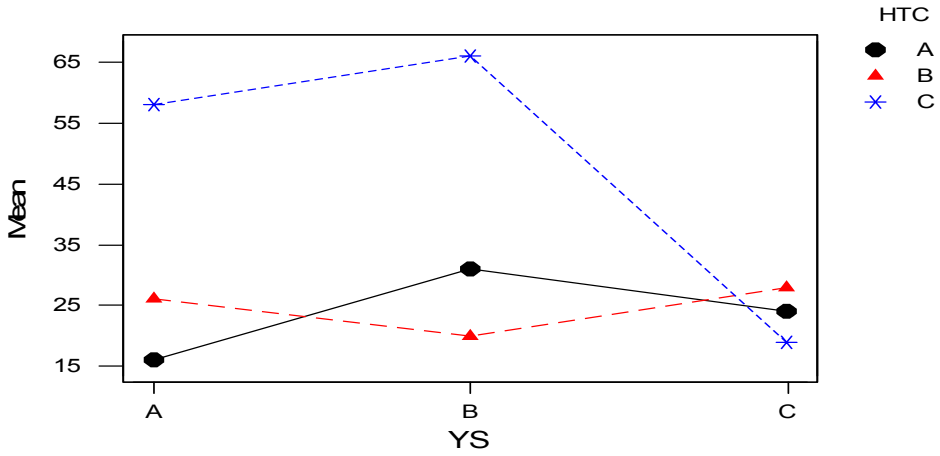

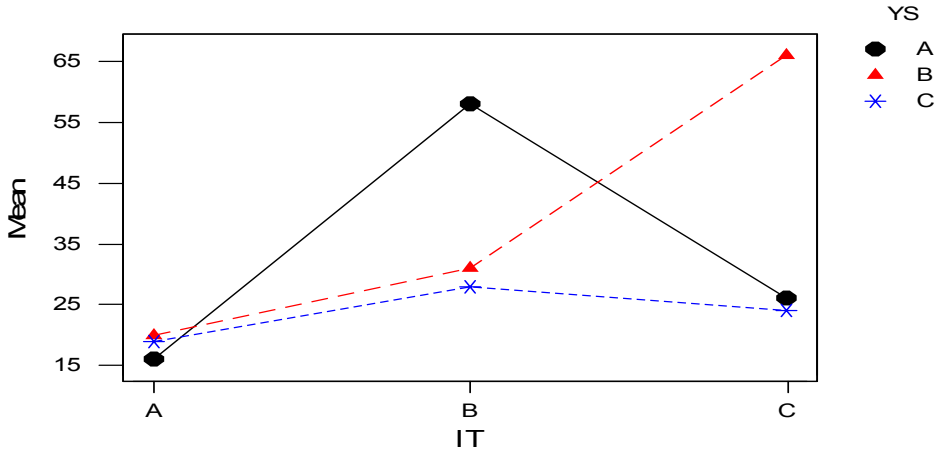

(b)

Figure 4.16: Interaction plot of HTC & YS (a), IT and YS (b) on the room temperature residual stresses at location 1

4.2.3 Distortion

Three dimensions were measured in the casting to quantitatively define the distortion in each case. The dimensions are the distances between the fins (D1, D2 and D3). Figure 4.17 shows the locations of the measured dimensions. The three dimensions (i.e. D1, D2 andD3) are located along the parting plane in the ejector die.

Dimensions D1, D2 and D3 were measured at a distance 5.08mm (0.2in) from the top of the fin to avoid the roundness on the fin corner. Each dimension was measured at five locations on the fin and the average of the five measurements was used for the comparison between the cases. In the next section of this chapter these dimensions will be compared to the experimental measurements. Due to the approximations and simplifications done with the solid model of the casting, it is not possible to compare the dimensions directly. To avoid this problem the *change in dimension* will be considered in the comparison rather the dimension itself. The term "*change in dimension*" means the difference between the dimension of the die and the correspondent dimension of the casting (ex. *change in dimension D1*=$D1_{die}$-$D1_{casting}$).

The dimension H, shown in Figure 4.17 is the height of the casting and is located across the parting plane. The variability of dimension H is expected to be a function of die separation during the casting process rather than a casting distortion. So the dimension H will be used only to compare with the experimental measurements.

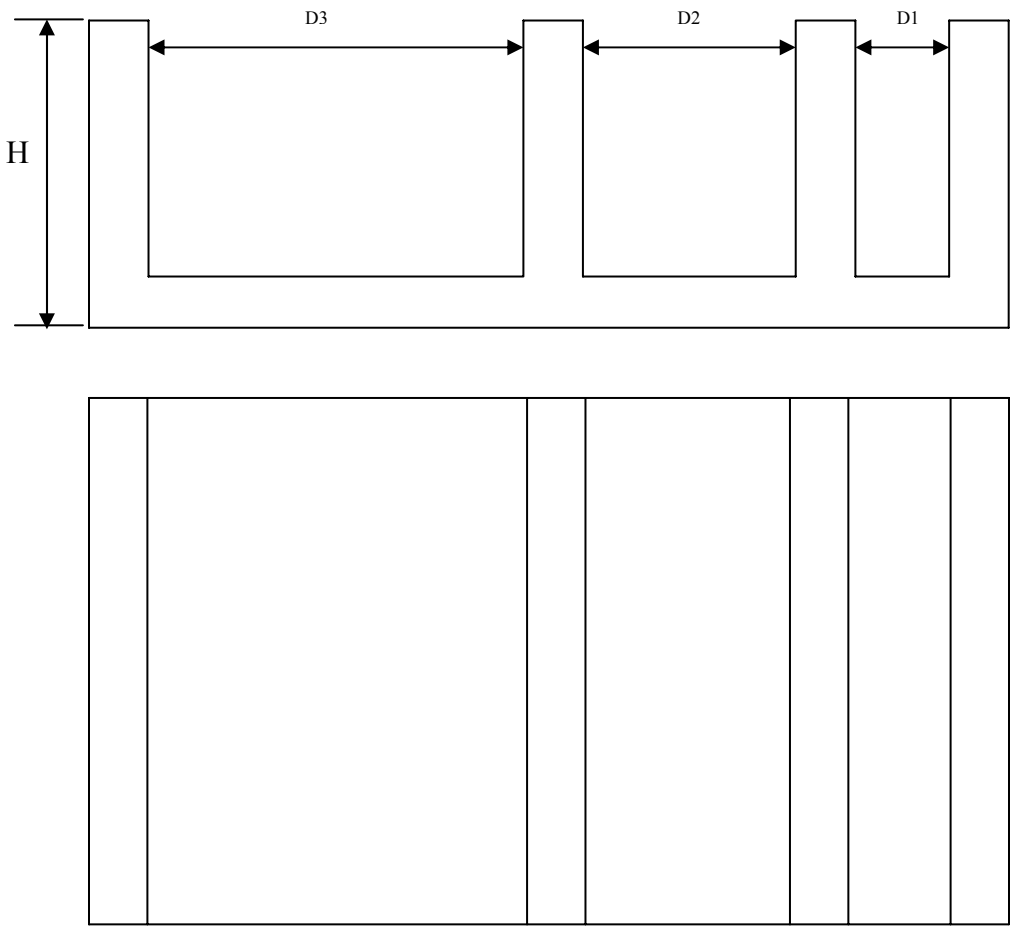

Figure 4.17: Casting dimensions used for comparing casting distortion

Figures 4.18 - 4.20 show the main effect plot of heat transfer coefficient (HTC), yield strength (YS), strain hardening (SH) and injection temperature (IT) on the dimensions D1, D2 and D3 respectively, at ejection (a) and at room temperature (b). The same scale is used for plots a & b in each figure.

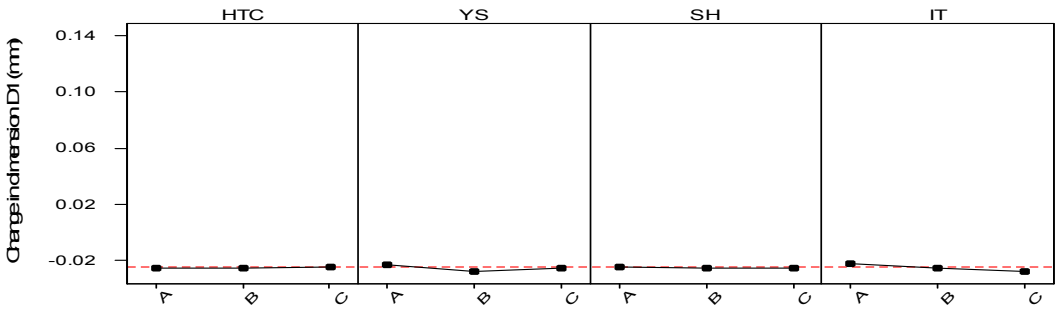

(a)

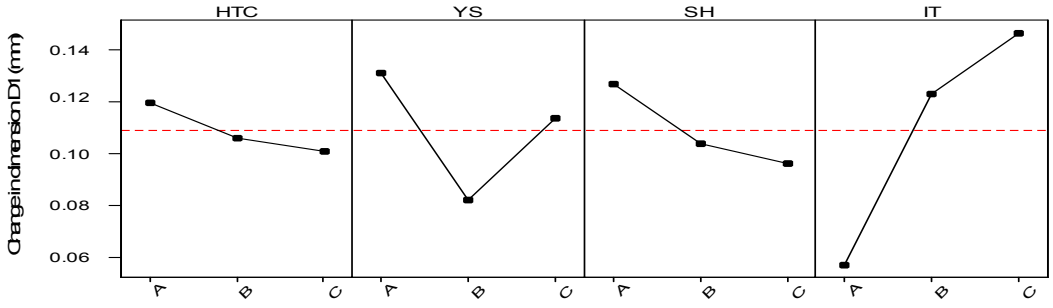

(b)

Figure 4.18: Main effect plot of HTC, YS, SH and IT on dimension D1 at ejection (a) and at room temperature (b)

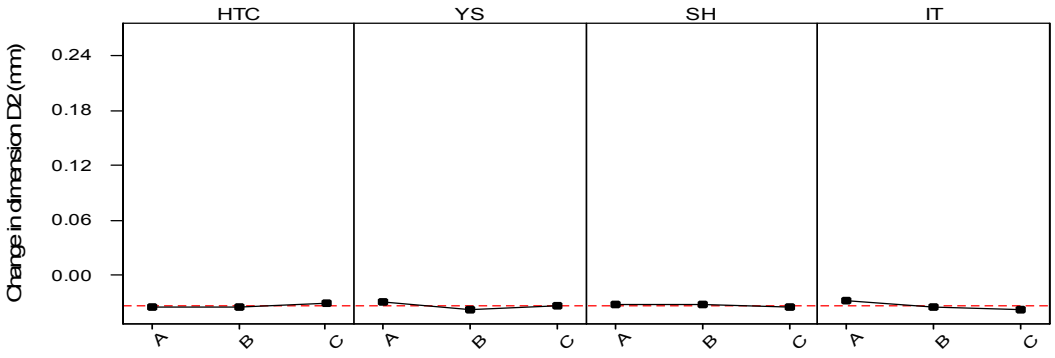

(a)

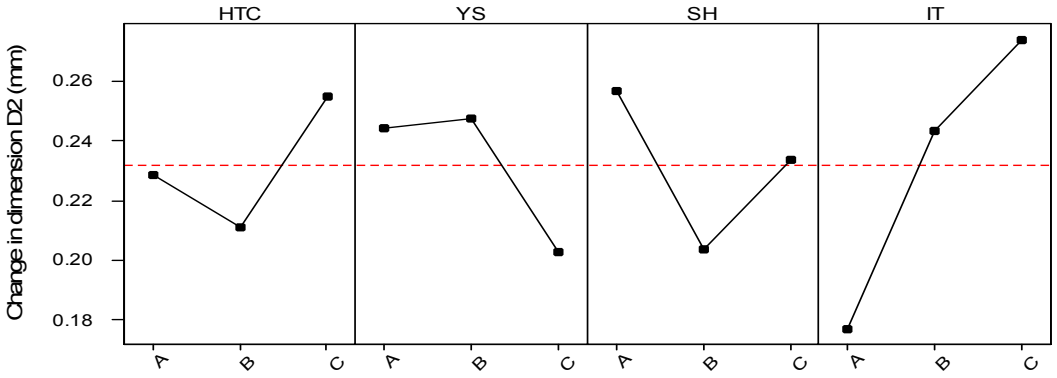

(b)

Figure 4.19: Main effect plot of HTC, YS, SH and IT on dimension D2 at ejection (a) and at room temperature (b)

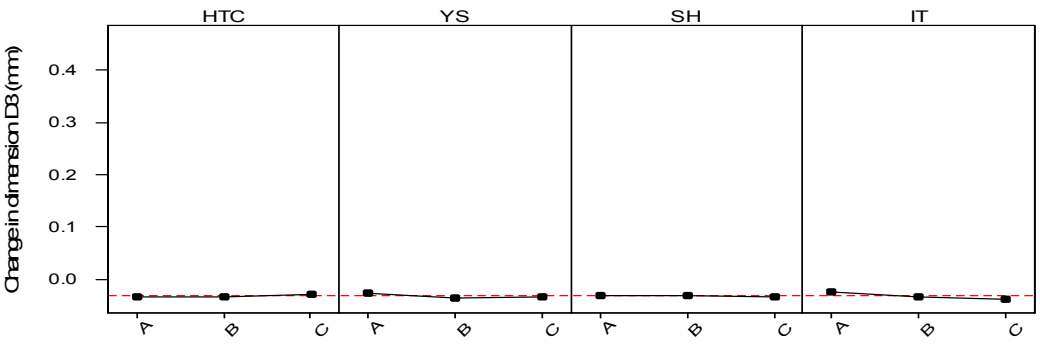

(a)

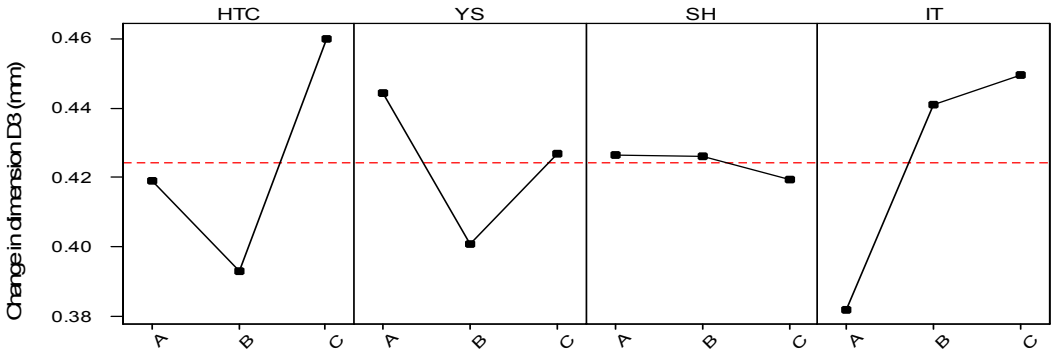

(b)

Figure 4.20: Main effect plot of HTC, YS, SH and IT on dimension D3 at ejection (a) and at room temperature (b)

Figures 4.18-4.20 demonstrate that the casting distortion at ejection is very small, compared to the final distortion, and is not affected by the different factors. These results matches the distortion patterns discussed in the first section of this chapter.

At room temperature, the final casting distortion is greatly affected by the different studied factors. The dimension D1 is affected mainly by the injection temperature followed by the yield strength, while the heat transfer coefficient and the strain hardening had non-significant effect. The dimension D2 was actually affected by all the factors as seen in Figure 4.19. However, like the dimension D1, the injection temperature had the greatest effect.

Dimension D3 was affected with all the factors except the strain hardening. As the other two dimensions, the main effect came from the injection temperature. The second main effect came from the heat transfer coefficient and the yield strength.

The results show that the higher injection temperature leads to higher distortion at all cases. Physically, this result is very reasonable, since more heat means more shrinkage and hence more thermal strains.

Other than the injection temperature, the other three factors did not have a common pattern of dimensions variability. This leads to the previous conclusion that the interaction between the ejection temperature and the ejection stresses is the controlling factor for final distortion results.

4.3 Comparison with Experimental Results

A comparison between the distortion, measured experimentally, and the simulation predicted distortion is vital in validating the adequacy of the model. In this section several comparisons between the simulation distortion predictions and the castings measurements are given. In all cases the comparison will be between the change in dimension, rather than the dimension itself as mentioned in the previous section

4.3.1 Dimensions Comparison

The four dimensions (D1, D2, D3 and H) shown in Figure 4.17 were measured from actual castings. The procedure to measure dimension D1, D2 and D3 was explained in section 4.3.2. This procedure was used both in the simulation and experimentally. The height of the casting (dimension H) was measured on the two fins close to the gate using a micrometer. It was measured at two points on each fin and the average of the four measurements was used for the comparison with the simulation data.

A comparison was set up between the changes of the measured dimensions experimentally and computationally. Figure 4.21 shows box plots for the changes in the four measured dimensions from both the simulation and the experimental work.

Figure 4.22 shows the simulation predictions in comparison with the measurements ranges. The measurements range was calculated as the mean value of the measurements ± 2 S, where S is equal to the standard deviation of the measurements.

Figure 4.21 demonstrates that the computational variability of dimensions D1, D2 and D3 is higher than experimental measurements. This is due to the effect of residual

stresses and temperature distribution at ejection. The nine cases had significant differences in ejection temperature and stresses, while the experimental castings did not have this variability. However, there is an overlap between the simulation predictions and the experimental measurements.

The results of dimension H had a different trend. The experimental distortion values are higher than the computational ones. On the other hand, the variability of dimension H measured experimentally is very close to the simulation variability. The first expected reason is the dynamic load during the injection and intensification. Different dynamic loads during different runs leads to different separation between dies and hence different dimensions across the parting plane. The dynamic effects are not considered in the simulation model. The effect of the dynamic load is dependant on several factors:

- Clamping load: While clamping load is assumed constant during a running session, it is actually changing with die temperature. The hotter dies leads to higher clamping load. The clamping load is constant in the simulation model.
- Poured metal. The amount of poured metal defines the biscuit thickness and hence the location of the plunger stopping during injection. If the biscuit is too thick, the plunger will stop before reaching its highest speed and hence the dynamic load will decrease. Since the pouring was done manually, there was not much control on the amount of poured material.

The second reason, and may be the most important for simulation results, is that there is no hydrostatic pressure applied on the casting in the simulation model. In actual case, the casting will be under hydrostatic pressure and will tend to fill the separation between the

two dies. This does not happen in the model because of the lack of hydrostatic pressure and the fact that solid elements are used rather than liquid elements.

Figure 4.22 shows that only Cases 1 & 2 predicted distortion within the measurements range for the dimensions D1, D2 and D3. Looking at Table 4.5, the only similar factor between the two cases is the heat transfer coefficient. But from the effect plots, the heat transfer coefficient is not the most significant factor. Actually, the most significant factor was the injection temperature. The results again displays clearly that the interaction between the ejection temperature distribution and residual stresses controls the final part distortion.

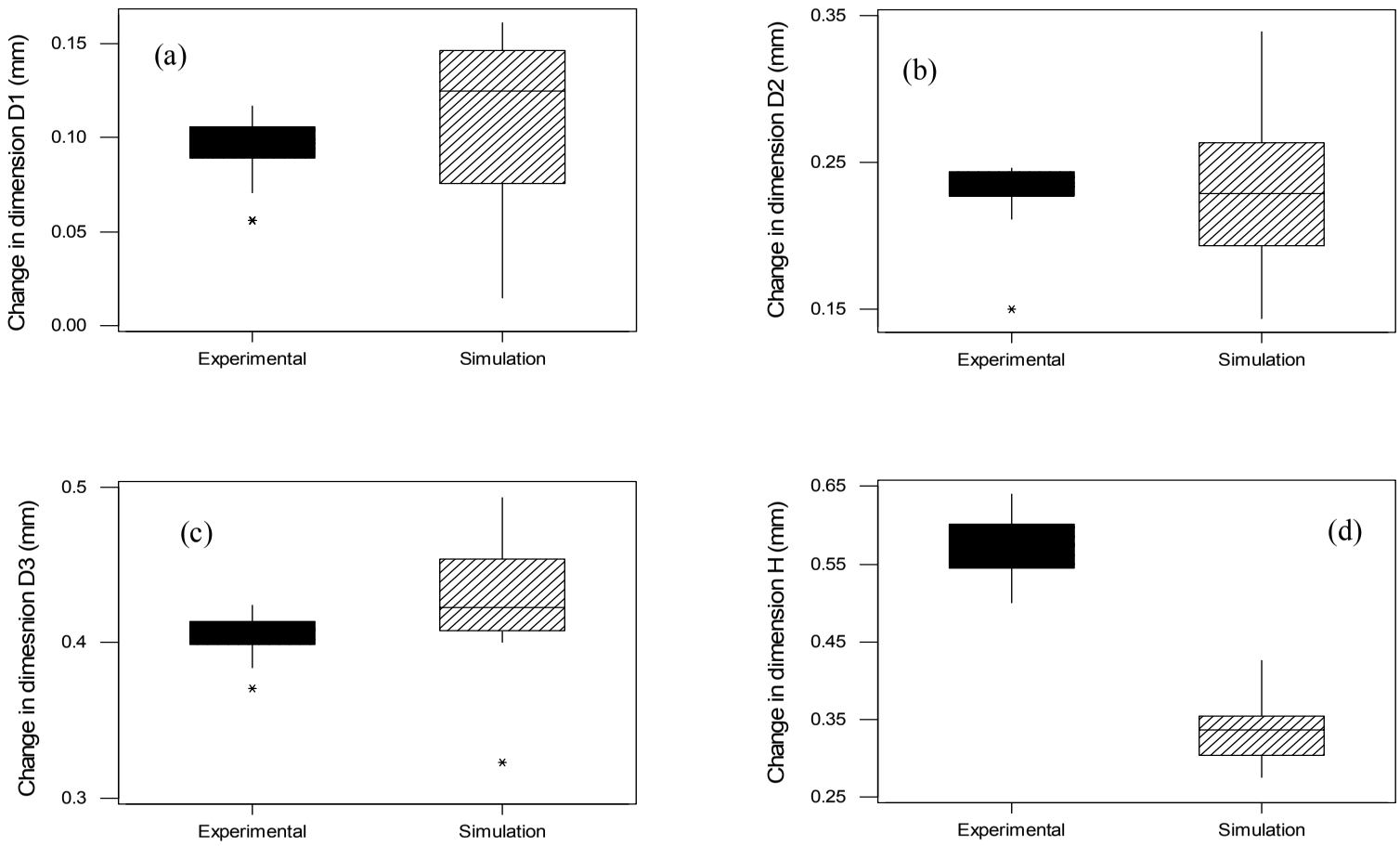

Figure 4.21: Comparison between the experimental measurements and the simulation prediction of the change in the casting dimensions D1 (a), D2 (b) D3 (c) and H (d)

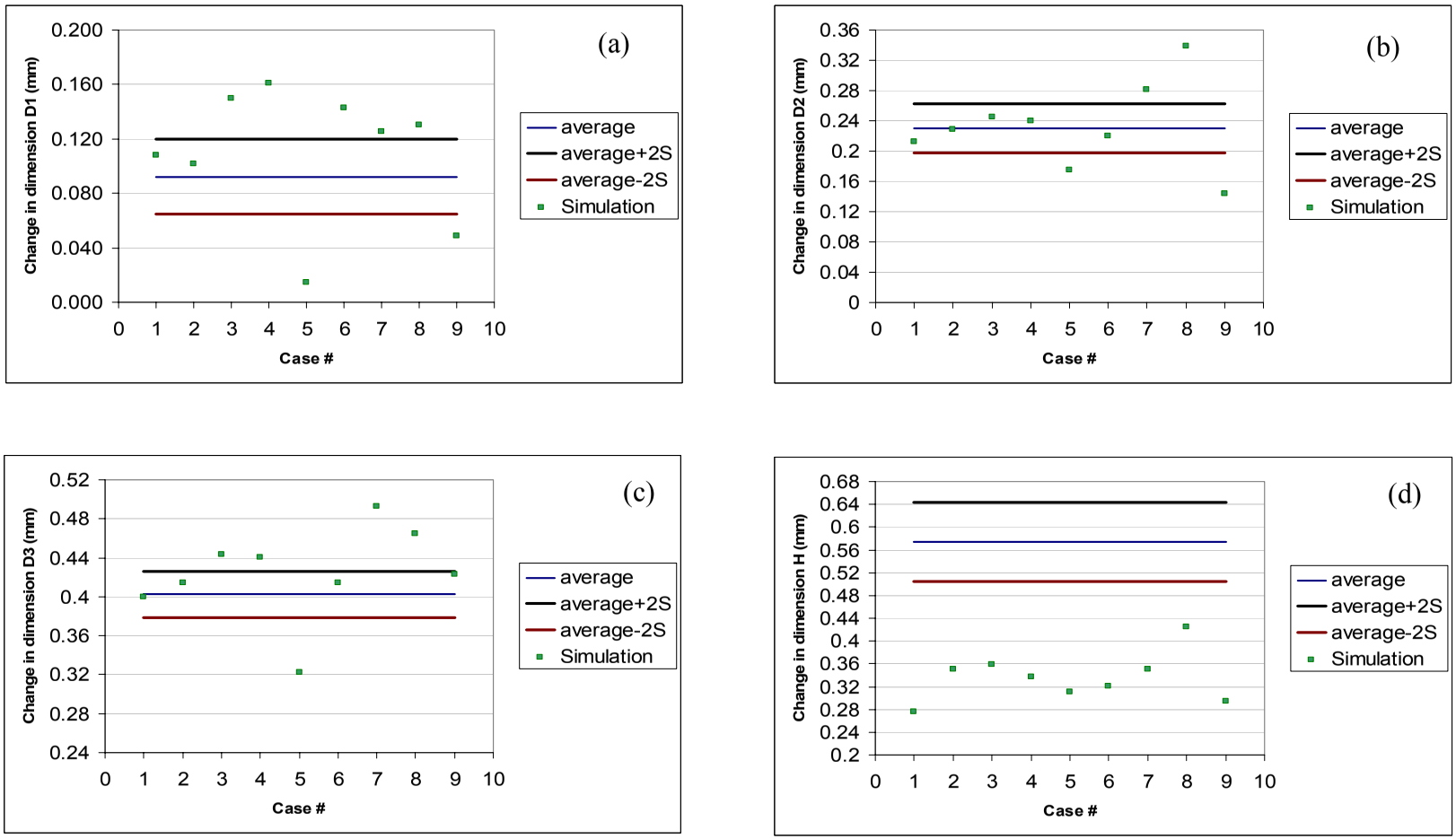

Figure 4.22: Simulation predictions as compared to the measurements of dimensions D1 (a), D2 (b), D3 (c) and H (d)

4.3.2 Flatness Comparison

The flatness was measured on the back surface of the casting, as shown in Figure 4.23. Experimentally, fifteen points were picked at the back of the casting and the coordinates of these points were measured using the CMM machine. A surface is then fitted between the fifteen points and the R-square value of the fitted surface was used as the flatness measurement of the surface. This process was repeated for all the castings. Figure 4.24 shows a scatter graph of the measurements of one of the castings.

To measure the flatness of the surface from the simulation, fifteen points were picked on the surface, and its coordinates were exported from the simulation results. A surface is then fitted between the points and the R-square value was used as the measurement of the flatness for the surface. This process was repeated for the nine cases.

Figure 4.25 shows a box plot comparison between the measured flatness (R square value) and the simulation predicted flatness. Figure 4.26 shows the R-square predicted by the simulation model compared to the R-square measured from the casting. The results showed that the simulation model under estimated the flatness defects compared to the experimental measurements. The reasons are the same for the under estimation of the variability of dimension H, that was discussed in the previous section. However the R-square values calculated from the simulation for the nine cases are within the measured values.

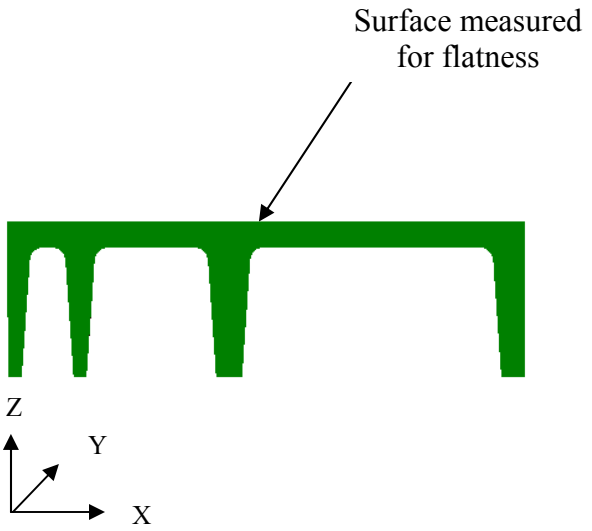

Figure 4.23: The casting surface measured for flatness

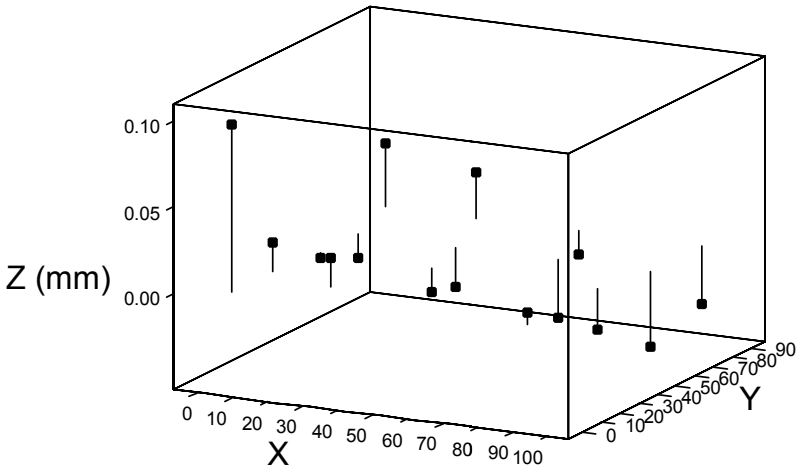

Figure 4.24: Scatter graph of the measurements of one of the castings

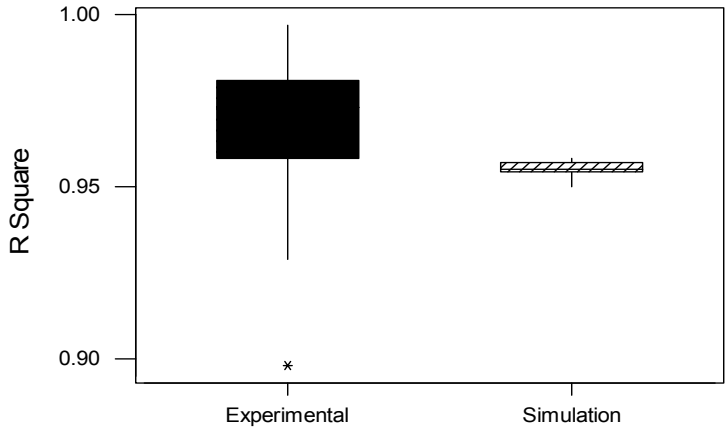

Figure 4.25: Comparison between the simulation predictions and the experimental measurements

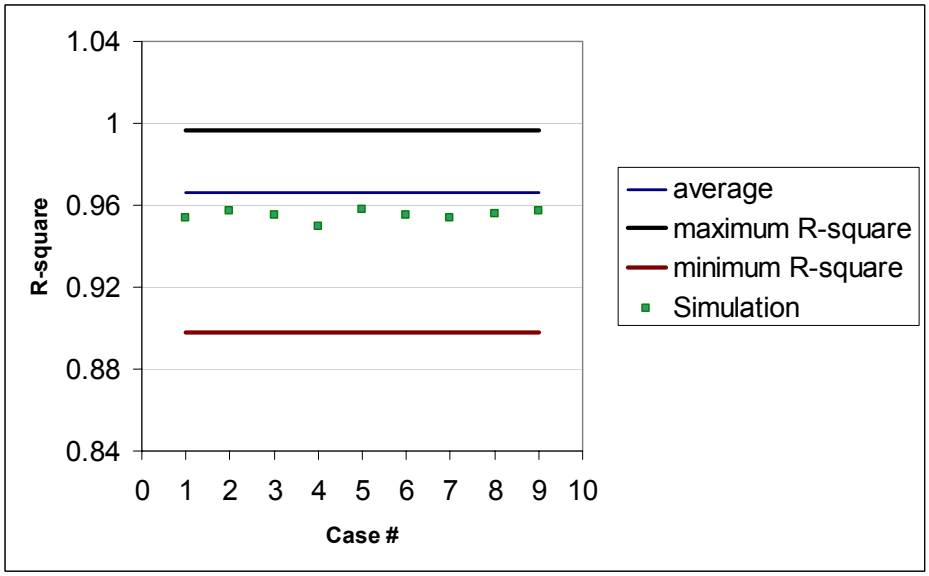

Figure 4.26: The simulation predicted flatness compared to the experimental measured range

4.3.3 Effect of quenching

Eleven castings were quenched in water after ejection to study the effect of quenching on the casting deformation. On the other hand, the simulation model was rerun with higher heat transfer coefficient to simulate the quenching process. Figure 4.27 shows comparison between air cooled castings and water cooled castings from experimental results and simulation predictions. The figure shows that there is an overlap between the box plots for the air cooled and quenched castings and therefore the quenching did not result in a significant effect on distortion. The measurements results were consistent with the simulation predictions.

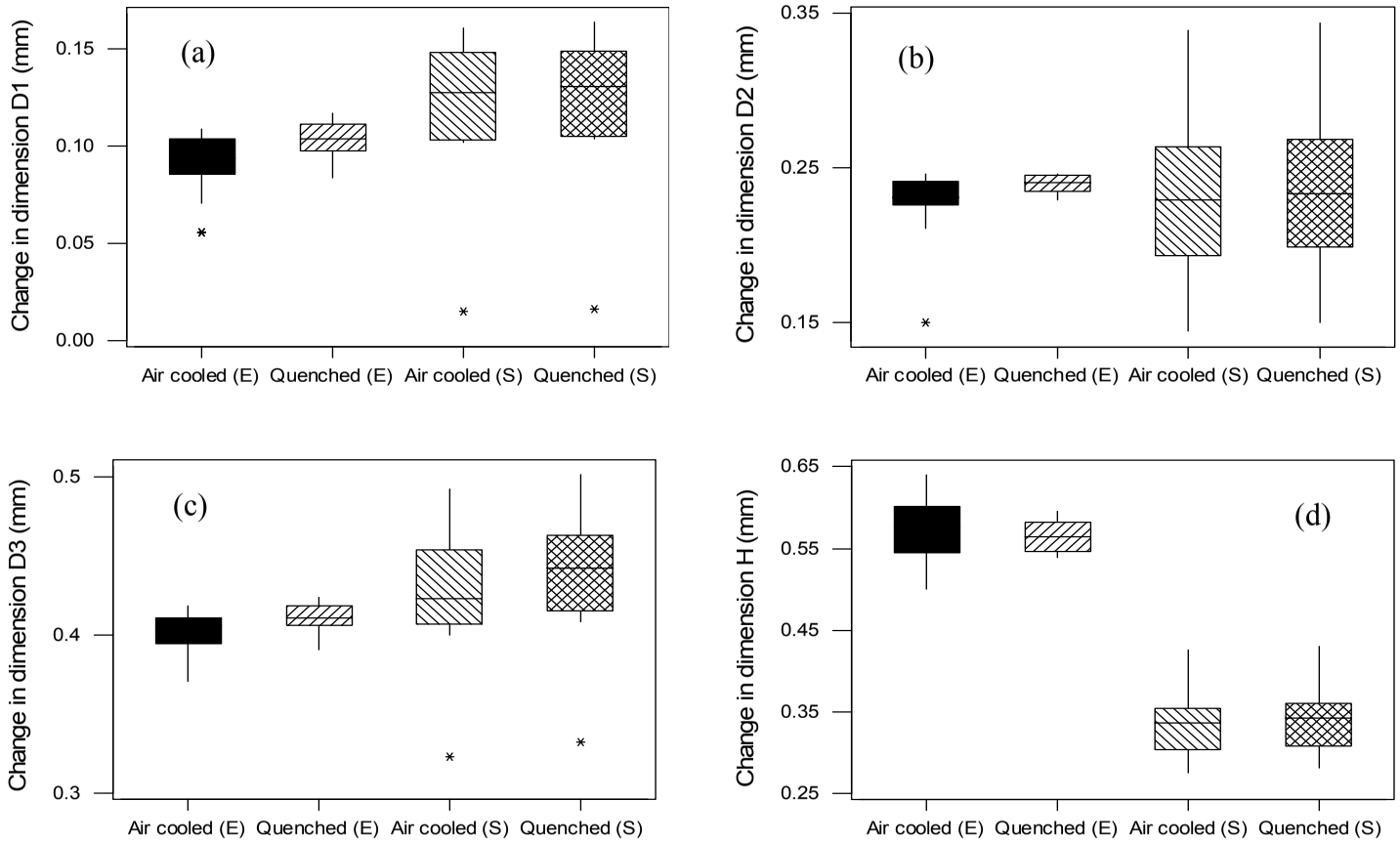

Figure 4.27: Comparison between air cooled and water cooled (quenched) castings for dimensions D1 (a), D2 (b), D3 (c) and H (d) from experimental data (E) and simulation (S)

4.3.4 Effect of residual stresses at ejection

The distortion of the casting after ejection is a function of its temperature and residual stress distribution at ejection time. The effect of residual stress on distortion is not trivial, and one of our research objectives is to demonstrate this effect. The same cases that are given in Table 4.5 were run again with stress free state at ejection. Thus the casting is ejected with only its temperature distribution and in-die distortion. The casting is then subjected to cooling at air. Figure 4.28 shows a comparison between the simulation predictions (stress free) and the experimental measurements range.

The results, given at Figure 4.28, show that there is no match between the predicted distortion and the experimental measurements. The predicted distortion is very small compared to the actual distortion. Recalling that the simulation predictions given in section 4.3.1 matched the experimental measurements in a very good manner, it is possible to conclude that the stresses at ejection are very important for predicting accurate distortion.

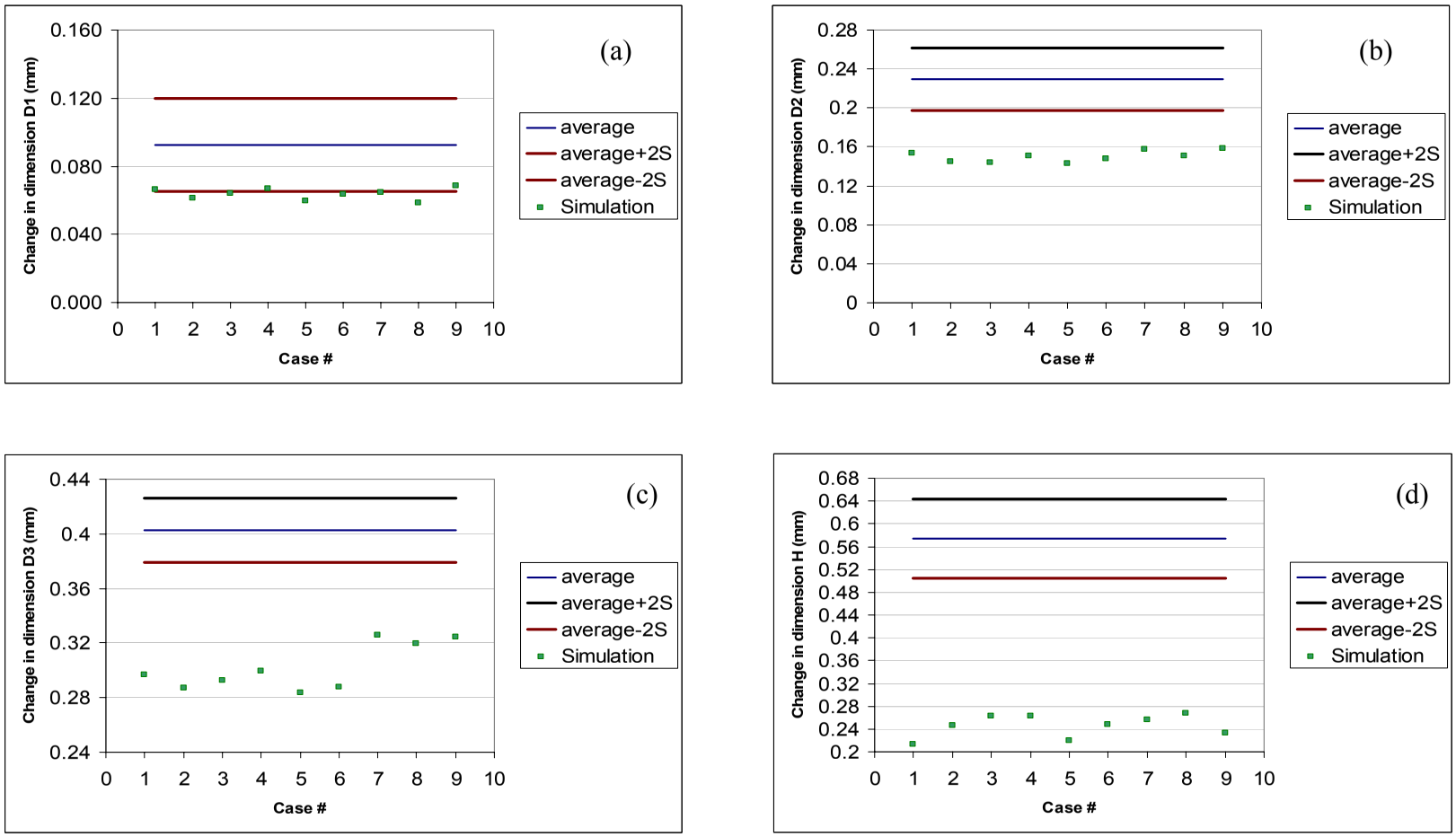

Figure 4.28: Simulation predictions (stress free) as compared to the measurements of dimensions D1 (a), D2 (b), D3 (c) and H (d)

CHAPTER 5

EXPERIMENTAL WORK

As mentioned in the second chapter, the process of modeling casting processes has increased for the last two decades due to the increase in the available computational powers. Finite element and finite difference methods are the main tools to build, solve and analyze simulation models that represent the different casting processes. Though the availability of computational powers makes it possible to run very comprehensive casting models, this is not always the case. The usual technique in building these models is to concentrate on few process characteristics and factors and assume -or neglect- the rest. So approximations and/or assumptions in the solid model, loads definition, process sequence, material physical and mechanical properties, etc. are very common.

Several reasons stand behind this attitude. One important reason is to get a cost effective solution even with sacrificing some generality and/or accuracy of the model. Another reason may be the lack of material information, especially at high temperatures. This is very clear when trying to define material properties in the simulation model. The lack of information may also extend to the boundary and initial conditions that should be included in the model. These boundary and initial conditions should represent the

working conditions and environment which are subject to change tremendously during different production sessions in the shop floor. For example the cleanness of die cooling lines in a die casting die can affect the heat transfer coefficient by order of magnitude. A third important reason is the limitations of the modeling packages. The only way to overcome short comings in the finite element or finite difference packages for the modeler is to develop his own solver and/or element. As a conclusion from the discussed points in the previous paragraphs, we can state that any simulation model needs to be verified.

In the previous chapter, a comparison between the casting distortion predicted from the simulation model and measured from actual castings was given. In this chapter more experimental work that was performed on the die casting machine, rather than the casting, is explained. All the experimentations were run on the die casting machine available in the Ohio State University. The machine is a Buhler SC-250 cold chamber horizontal die casting machine, with maximum loading capacity of 250 tons. This machine is the same one that was modeled in the simulation.

Several quantities have been measured in the machine and compared to the similar quantities from the simulation models. These quantities are: contact forces between dies and platens, strain in tie bars and temperature in the inserts. It was planned to measure the cavity pressure in the ejector side, but the pressure sensors did not work properly. Two loading conditions were examined, the first one is clamping load only with no casting, and the second one is normal casting operation. This chapter describes the experiment methodology, results, discussion and conclusions.

5.1 Experiment methodology

All the applied loads in the model are mechanical or thermal loads. The mechanical loads result from the machine clamping and reactions and from the applied intensification pressure. The thermal load comes from the heat transfer through casting/inserts interface, inserts & dies/cooling lines interface and the heat dissipated to the environment.

To test the contribution of the machine parts to the mechanical loads, the contact forces between the dies and platens were measured. Load cells were inserted between the dies and platens on both cover and ejector sides. Special fixtures were designed to hold the load cells.

The reactions in the machine were measured using uniaxial strain gages on the tie bars. Four strain gages were fixed on each tie bar and the average value was used to compare with simulation results. The die casting machine has the capability to give the total clamping load, but, unlike some die casting machines, it does not have the capability to give the load in each tie bar separately. Another important benefit from measuring the strain in the tie bars, besides comparing with the model predictions, was to assure that the tie bars are balanced and the clamping load is symmetric around the vertical axis that passes through the center of the die, as it was assumed in the model.

Strain gages were used to measure the strain in the dies. Uniaxial strain gages were fixed on the die steel –both cover and ejector sides- to measure the strains in the three directions (X, Y and Z).

To test the thermal loads, the temperature was measured in four locations in the cavity. Three thermocouples were inserted in the cover insert, while the fourth one was inserted in the ejector insert.

The simulation model was modified to allow for adding the load cells and their fixtures. The locations of the load cells were tested, after the first design, through the simulation by Zhang [10]. From the simulation test, some load cells were predicted to have high loads (very close to its maximum capacity), and consequently they would be in danger of damage. The design then was modified to overcome these problems. More load cells were added and locations were changed. The load cells placement explained later in this chapter is the final design.

5.1.1 Loading Conditions

Two different load conditions were applied during the experiment, as shown in Table 5.1. In the first load condition, only the clamping load was applied (in other words there was no actual casting process). This loading condition was very important for verifying the simulation model. It was also very useful in testing our equipment and designs. One important feature in this load condition is that, the clamping force is completely controlled by the machine controlling unit, and hence there were no unpredicted factors that may affect the comparison between the simulation model predictions and the sensors readings. Under the first loading condition, two clamping loads were examined, 1500 KN, which is the minimum clamping load allowed by the machine, and 2500 KN, which is the clamping load that would be used with our casting. During the first load condition, only the load cells and strain gages were active.

In the second load condition, an actual casting process was run and several castings were produced. Semi-automatic casting cycle was selected. In this type of cycle the die closing period and casting ejection period is controlled by the machine controlling unit, while the pouring, extracting and spraying are controlled by the operator. This cycle was selected because the pouring robot, spraying reciprocator and extractor did not work properly and manual pour and spray were used.

Several factors affect the results under the second loading condition. Some factors are completely controllable (for example: the clamping force, and die closing period). Other factors are partially controllable (for example: pouring temperature, spraying time and amount and overall cycle time). The cycle used was the same one given by Osborne M. [40], and it is as given in Table 5.2.

A Labview program was developed to collect the data from the sensors, see Appendix C. A sampling rate of 1000 samples per second (SPS) for each sensor was used. In some cases a sampling rate of 3000 SPS was used to catch the impact loads caused by the molten metal injection and intensification.

Load Condition		Active Sensors
Load Condition I	1500 KN Clamping	Load Cells & Strain Gages
	2500 KN Clamping	Load Cells & Strain Gages
Load Condition II	2500 KN Clamping + Casting	Load Cells, Strain Gages & Thermocouples

Table 5.1: Loading conditions

Cycle Segment	Time (Sec)
Ejector retract	1.5
Machine close	2.5
Machine lock	2.5
Pour charge	2.5
Metal injection	0.5
Solidification	8.0
Decompression	0.5
Machine open	3.0
Ejection	3.0
Casting removal	10.0
Spray release	4.5
Delayed closing	1.5
Total cycle time	40.0

Table 5.2: Cycle time [40]

5.1.2 Load Cells Placement

Diaphragm load cells were used to measure the contact force between the dies and platens. Eighteen load cells were inserted on the cover side and seventeen were inserted on the ejector side. Each load cell capacity is 444.8 KN (100,000 lbs). Properties of the load cells are given in Appendix B

As shown in schematic drawing, Figure 5.1, three steel plates were used, on each side, as a fixture for the load cells. Plate 1&3 were used to protect the platen and die, respectively, from the load cells footprints. Plate 2 was used to restrain the load cells from vertical and horizontal movement. As noticed in the figure, the thickness of plate 2 is less than the height of the load cells to allow the load cells to respond to the applied forces.

Plate 1 is clamped to the platen using standard die clamps. Plate 3 is bolted to the die and plate 2 is bolted to plate 3. Figures 5.2- a and 5.2- b show the load cells fixture plates on cover and ejector sides respectively. Detailed drawings of these plates are given in Appendix A. Figure 5.3 shows the load cells location and identification number in both cover and ejector sides.

Flatness of the fixture plates is very important to have good contact between the plates and the load cells. Using a CNC milling machine achieved flatness of 0.004 inch in the plates, but at the first run it was clear that this flatness was not good enough. The plates were then ground using a Blanchard Grinding Machine modifying the flatness to 0.001 inch. Even with this level of flatness we had some problems with contact. One load cell was shimmed –E16– because it was not in a perfect contact with the plates. This problem with contact was noticed because the reading from this load cell was very low

compared to the neighbor load cells. A feeler gage was then used to check if there is a gap between the load cell and the fixture plates. Depending on the gap size, an appropriate shim was inserted between the load cell and the plate.

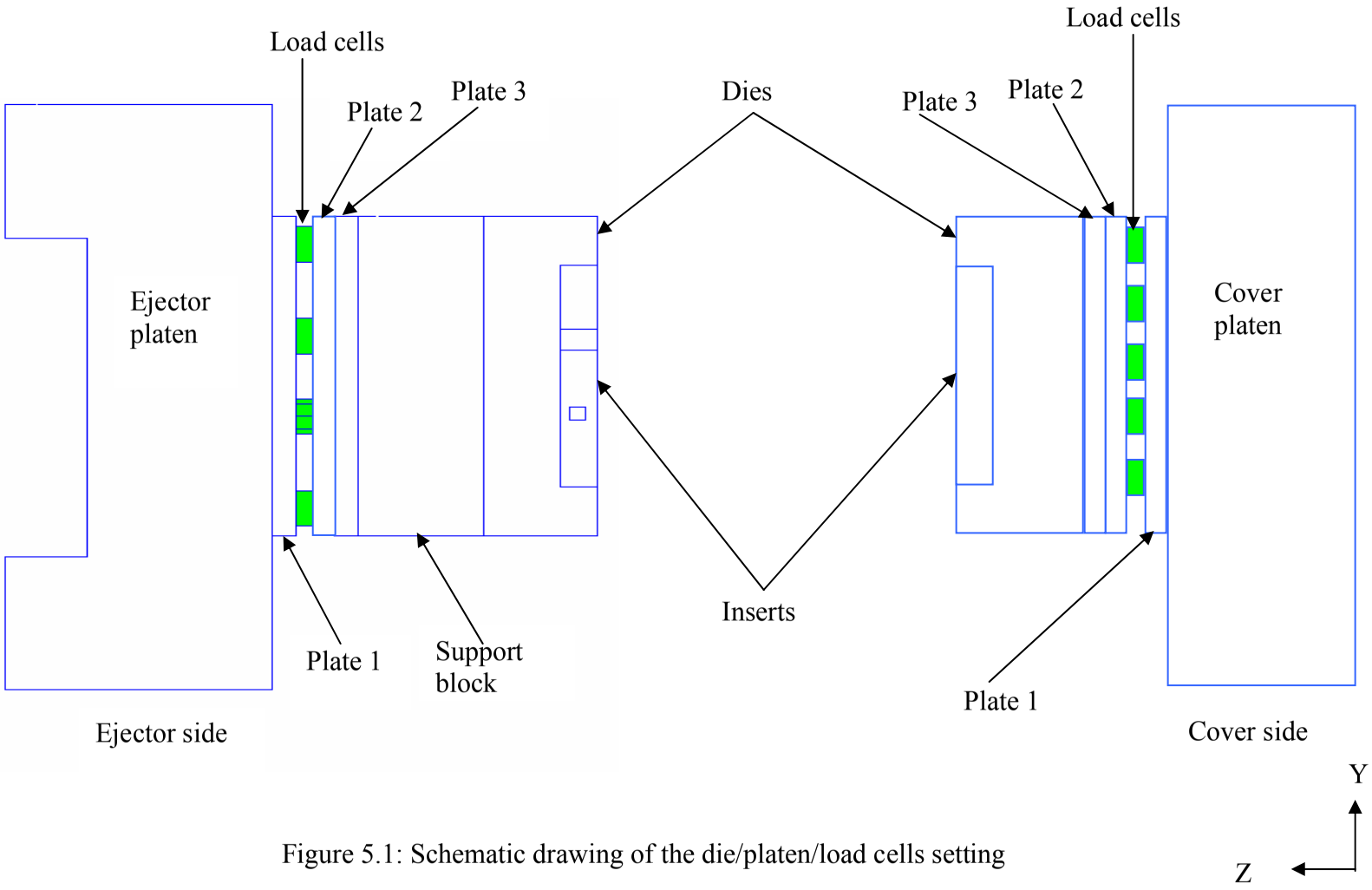

Figure 5.1: Schematic drawing of the die/platen/load cells setting

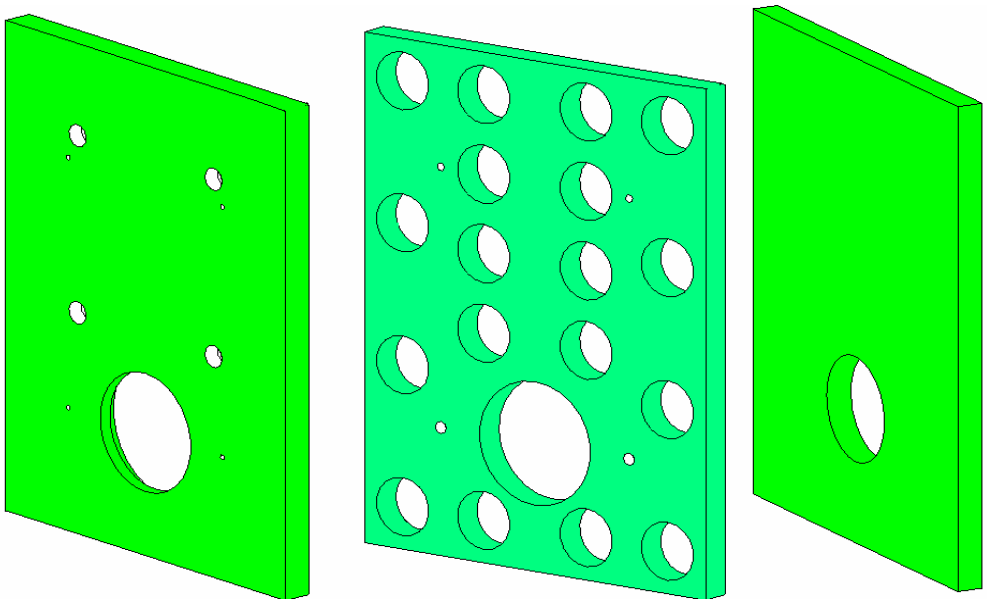

(a)

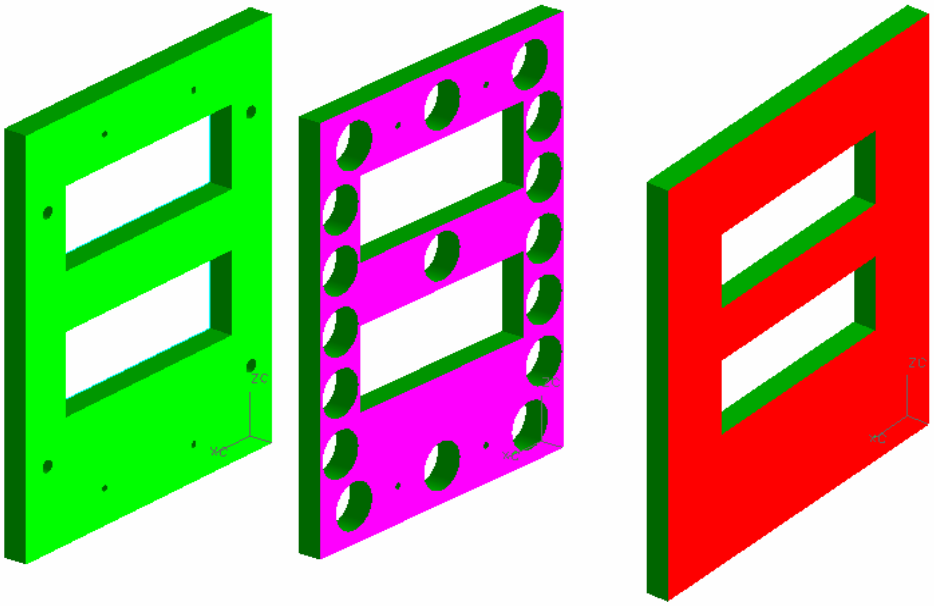

(b)

Figure 5.2: Load cells plates at: (a) cover side & (b) ejector side

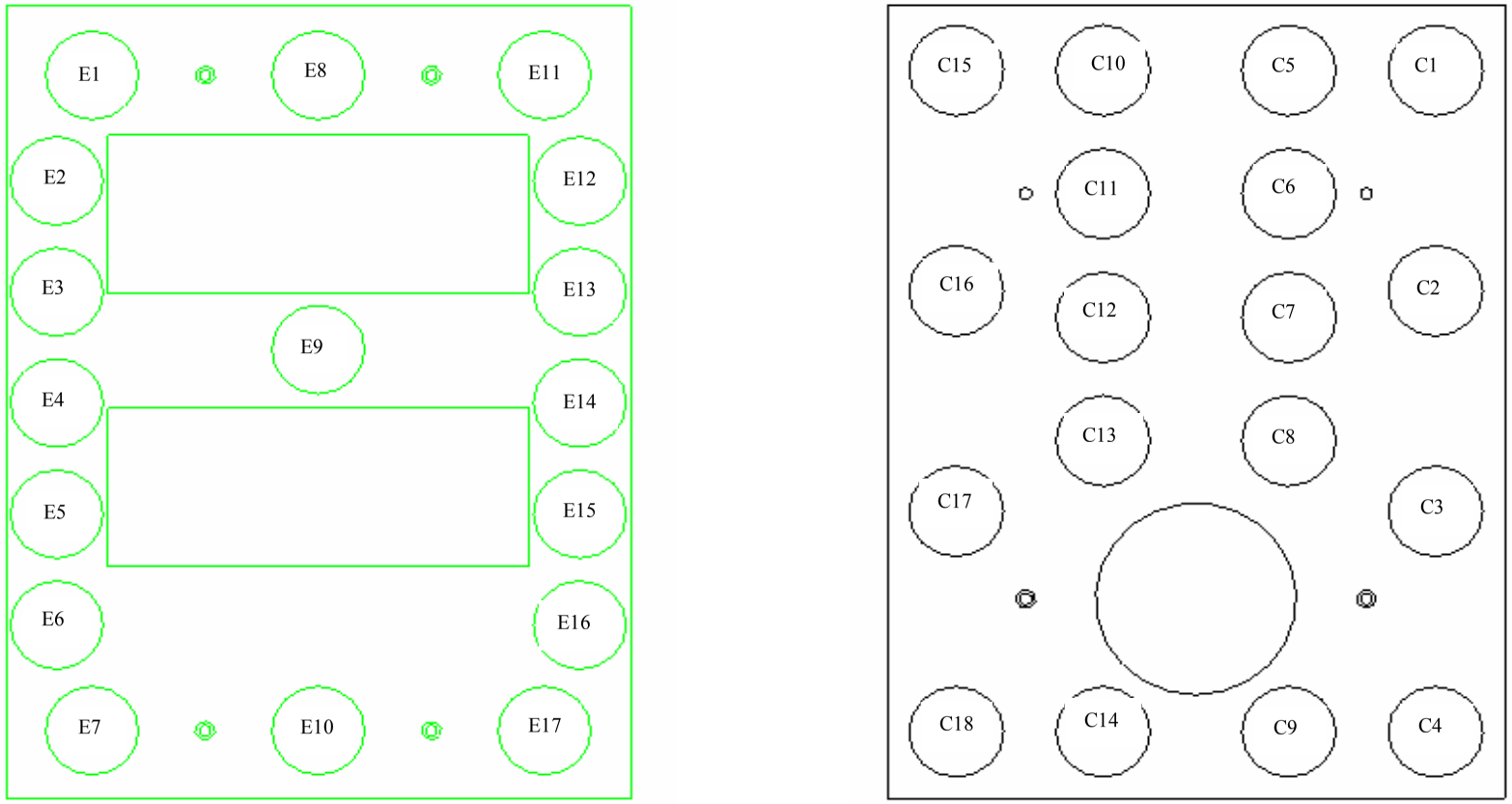

Figure 5.3: The load cells identification numbers

5.1.3 Strain Gages Placement

Uniaxial strain gages were attached to the machine tie bars to measure the longitudinal strain. Four strain gages were attached to each tie bar. Figure 5.4 shows the tie bars identification numbers with respect to the back of the cover platen and the locations of the strain gages on each tie bar. The strain gages were mounted on the tie bars at a distance of 267 mm (10.5 in) from the cover platen. At this distance the strain gages are in the middle between the two platens when the die is closed.

The strain gages were attached to the tie bars using a special type of glue. Details of strain gages and glue characteristics can be found in appendix B.

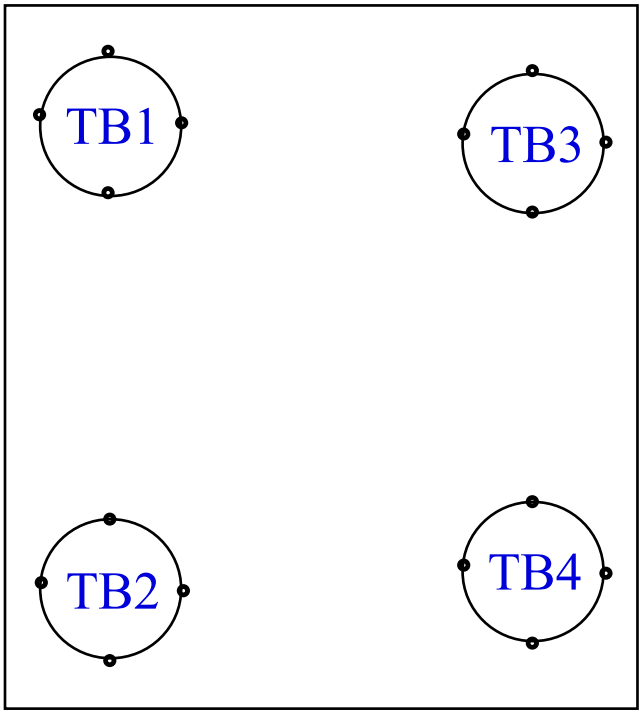

Figure 5.4: Tie bars identification numbers with respect to the cover platen

A total of 16 uniaxial strain gages were fixed to both cover and ejector dies. Figures 5.5 and 5.6 show the locations of the strain gages in the cover die and ejector die respectively. There are two strain gages at each location. Table 5.3 summarizes the strain gages directions at each location.

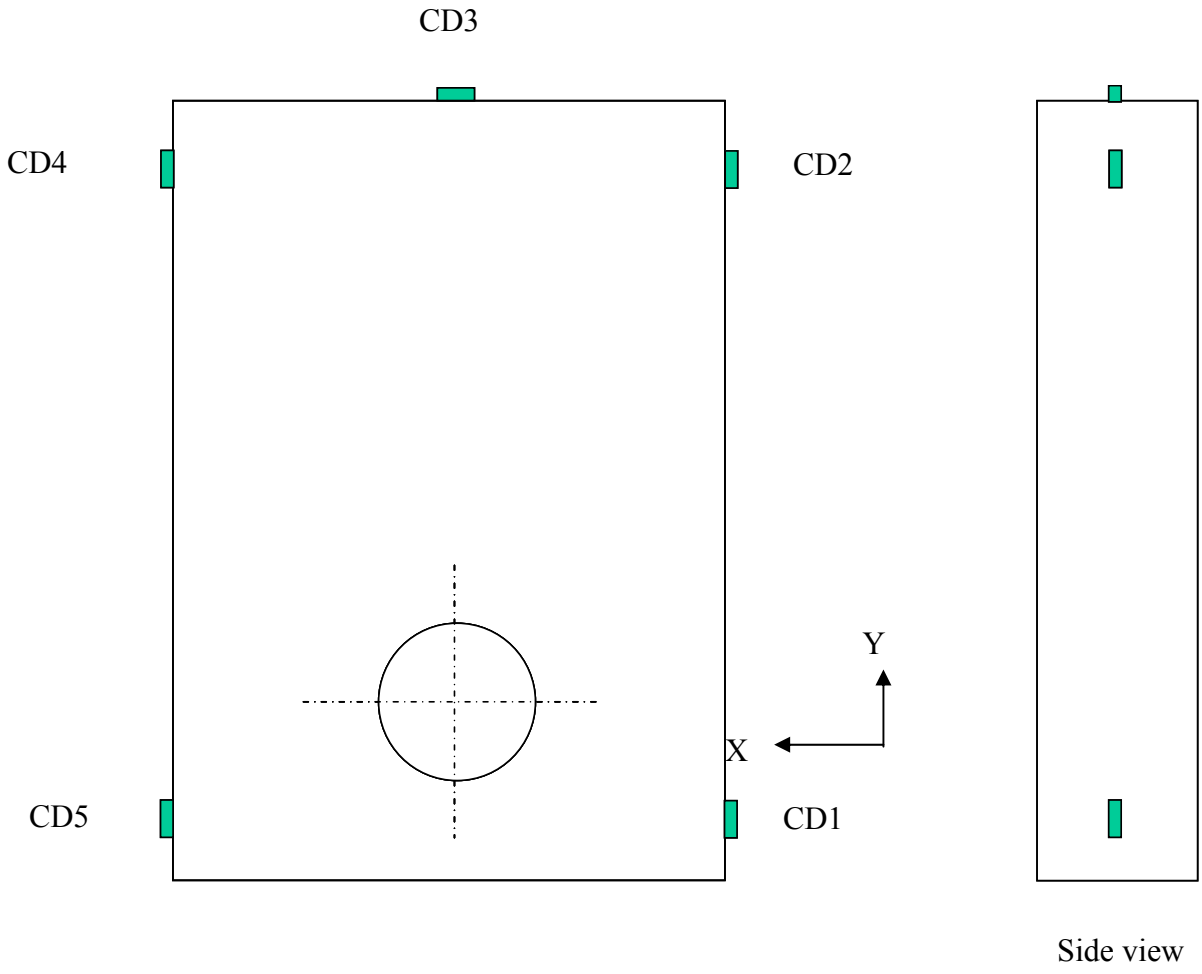

Figure 5.5: Locations of strain gages on the cover die

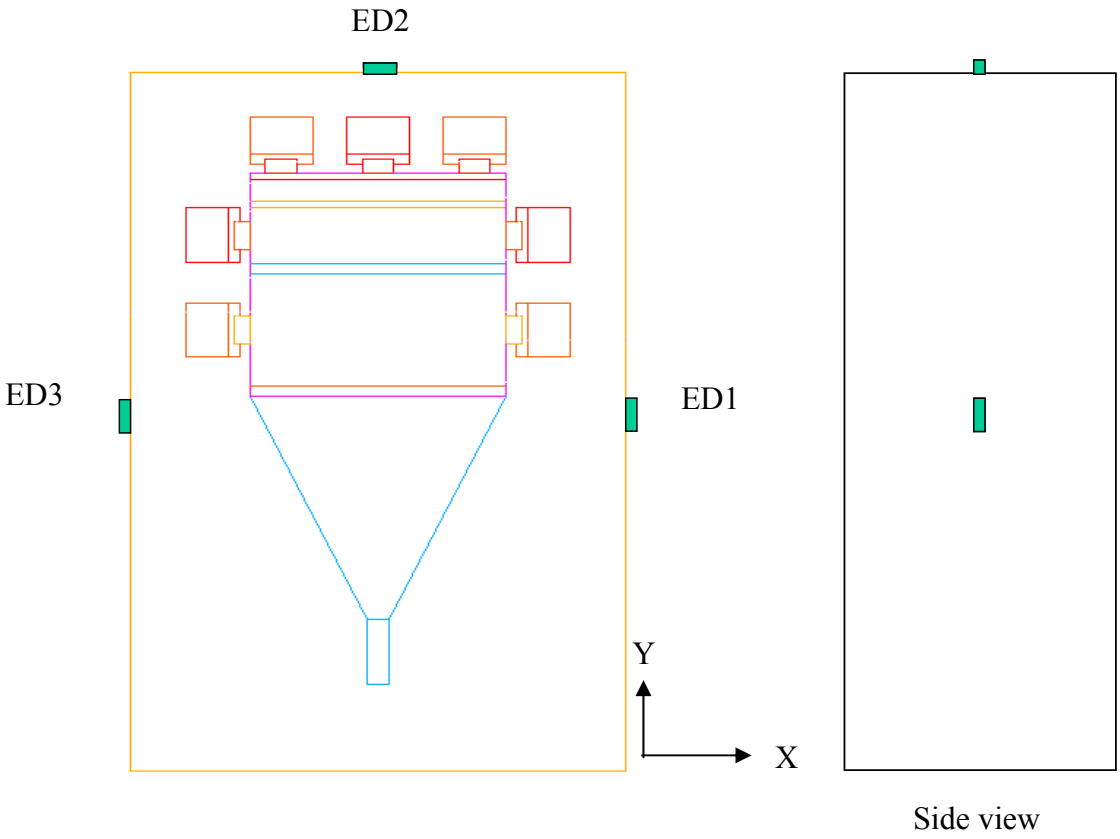

Figure 5.6: Locations of strain gages on the ejector die

Location	Strain gages directions	Location	Strain gages directions
CD1	Y&Z	ED1	Y&Z
CD2	Y&Z	ED2	X&Z
CD3	X&Z	ED3	Y&Z
CD4	Y&Z		
CD5	Y&Z		

Table 5.3: Strain gages directions at cover and ejector dies

5.1.4 Thermocouples Placement

Four K-type thermocouples were used to measure the temperature in four locations in the inserts. Three of them were on the cover side and one on the ejector side. The thermocouples were inserted at a distance of 12.5 mm (0.5 in) from the cavity surface.

The thermocouples were located in four existing holes in the cover and ejector inserts. These holes were made in previous research [40], to be used with thermocouples and pressure sensors interchangeably. Figure 5.7 shows the thermocouples locations in the cover and ejector inserts (denoted by T1 – T4). Special H 13 steel fixture was designed and made to mount each thermocouple. The fixture drawing is shown in Appendix A. Each thermocouple was cemented to the fixture using special high temperature cement. Details about the thermocouples and cement characteristics are given in Appendix B

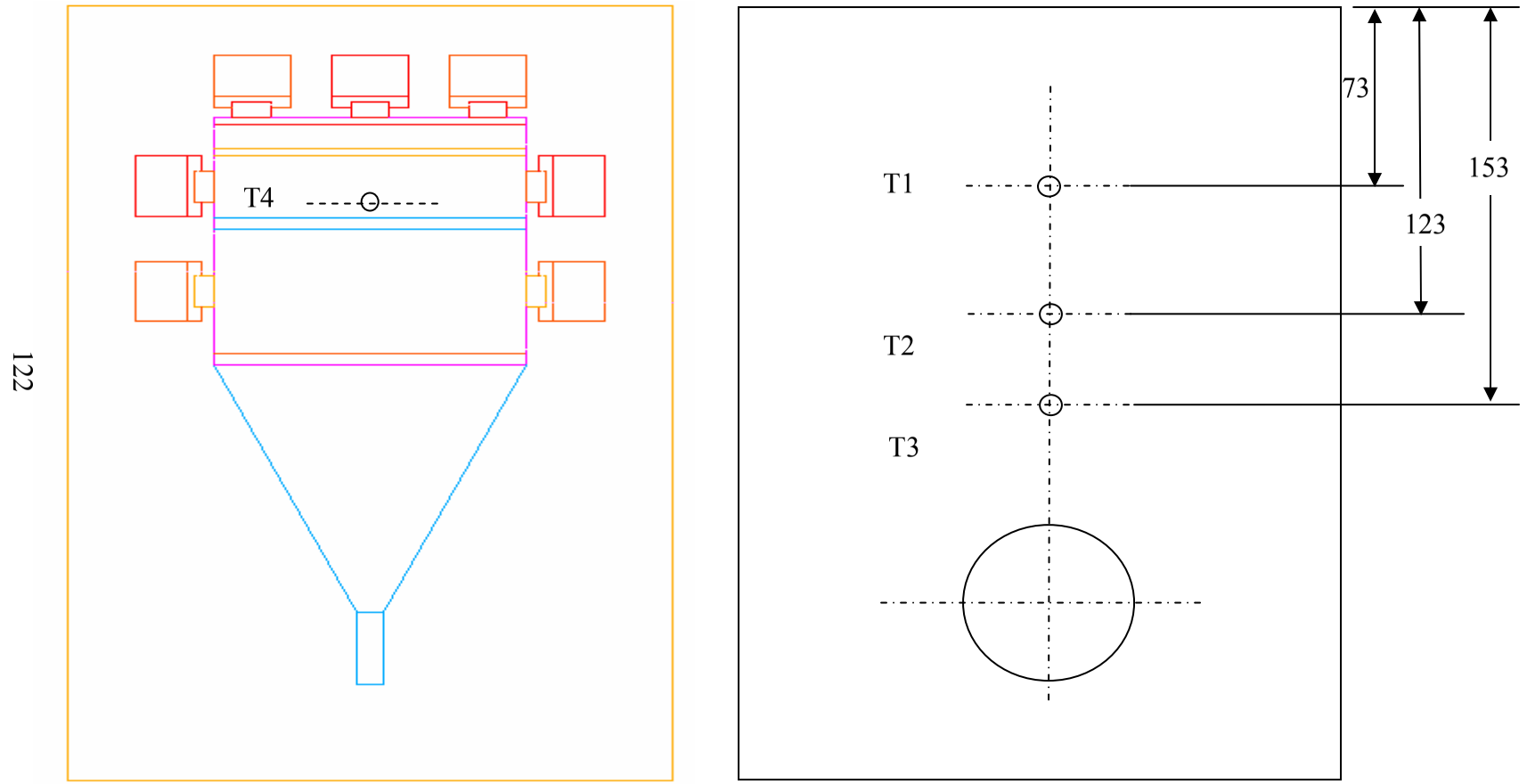

Figure 5.7: Thermocouples locations in the cover and ejector sides (dimensions in mm). The thermocouples were located at a depth of 0.5 inch from the cavity surface

5.2 Experiment Results

5.2.1 Load Condition I

5.2.1.1 Load cells

As mentioned before two clamping loads were applied in load condition I, these are 1500 KN and 2500 KN. The machine actually applies the load within preprogrammed tolerance. Due to this tolerance the machine clamping load readings were 1575 KN and 2452 KN. At each clamping loading twelve runs were conducted. The average of the twelve runs was used to compare test results with the simulation predicted values. Table 5.4 shows the average of the readings and the standard deviation for each load cell at the two clamping loads. Table 5.5 gives the load cells loading predicted by the simulation model. Examining the value of the standard deviation value for the load cells readings show that its value is very small compared to the average value. This shows that the repeatability of the measurements is high.

Figures 5.8 and 5.9 show comparisons between the simulation predictions and experimental measurements at a clamping load of 1575 KN for load cells at cover side and ejector side respectively. Figures 5.10 and 5.11 show comparisons between the simulation predictions and experimental measurements at a clamping load of 2452 KN for load cells at cover side and ejector side respectively.

To understand the Figures 5.8-5.11 one must recall that the die is symmetric around a plane that passes through the center of the shot sleeve hole and perpendicular to the parting plane. The symmetry is very clear in Figure 5.7. Due to this symmetry, only half of the die casting machine was modeled and, as a consequence, the similarity of load

cells readings around the symmetry plane was assumed. Load cells identifiers in Figures 5.8-5.11 are organized in a special order to show the simulation prediction, and the two measurements for the load cells that, in an ideal case, would be symmetric. The figures show also the error bar for each load cell which equals to 1% FSO (4.5 KN).

Figures 5.8 and 5.10 compare the cover side load cells readings from test and simulation at clamping loads of 1575 and 2452 respectively. The comparison leads to several conclusions:

- Good symmetry is achieved between load cells on both sides of die symmetry plane, except for load cells C8 & C13. Perfect symmetry was not expected due to slightly different tie bars loading and due to different flatness values on platen, die and fixture plate surfaces. As mentioned before the load cells are very sensitive to the flatness of the surfaces they are in contact with.
- At the low clamping load, load cell C13 reads zero, while at the high clamping load it reads very low value compared to C8. The reason is that, at no-load condition, it is noticeable that this load cell is not in perfect contact with the plate surface. And since it was impossible to reach this load cell after assembly we could not shim it.
- A good match is noticed between the simulation model predictions and the experimental measurements, except at load cells C1, C15, C5, C10 and C13. The maximum loading in the simulation was at load cell C1 – and by symmetry C15- while in the experiment, the maximum loading was at C5 and C10. This is because of difference in clamping conditions between the model and the actual set up in the machine. In the machine, standard die clamps are used to clamp the die

to the platen. These clamps are not modeled in the simulation due to the complexity of modeling them and the expected computational problems due to their contact with the die and the platen. In the simulation model clamps are replaced by tying the two surfaces in contact with each other. Considering modeling the die clamps explicitly may be a good idea in continuing this research.

Figures 5.9 and 5.11 compare the ejector side load cells readings from test and simulation at clamping loads of 1575 and 2452 respectively. The comparison leads to several conclusions:

- A good symmetry is achieved between load cells on both sides of die symmetry plane except for load cells (E6 & E16). The reasons for non-symmetry were discussed earlier.
- A good match is noticed between the simulation model predictions and the experimental measurements, except at load cells E8 and E9. As shown in the figures, the maximum predicted load –by simulation- was at load cell E1 and by symmetry E11. The experiment results showed the same thing. Also the minimum predicted load –by simulation – was at load cells E8, E9 and E10. Again the experiment results showed the same trend.
- A significant difference is noticed between the simulation and the test at load cells E8 and E9. The model under predicts the load at these two load cells. This is possibly due to the effect of the ejection mechanism on the ejector die. The ejector mechanism may carry some load from the ejector die back plate and

transfer it to the middle load cells. The ejector mechanism was not included in the simulation model.

Figures 5.12 & 5.13 illustrate the %error between the simulation predictions and the load cells readings for clamping load 2452 KN at cover and ejector side respectively. The %error equals to the absolute value of (predicted load-measured load) *100 / measured load.

	1575 KN Clamping Load		2452 KN Clamping Load	
Load Cell ID #	Average Load (KN)	Standard Deviation (KN)	Average Load (KN)	Standard Deviation (KN)
C1	72	0.07	141	0.51
C2	89	0.07	144	0.52
C3	112	0.09	174	0.72
C4	130	0.08	203	0.25
C5	205	0.05	269	0.32
C6	35	0.02	61	0.39
C7	33	0.05	51	0.13
C8	96	0.16	122	1.21
C9	68	0.04	103	0.65
C10	191	0.10	254	3.65
C11	19	0.03	43	0.20
C12	31	0.03	48	0.17
C13	0	0.00	8	0.04
C14	64	0.04	99	0.22
C15	98	0.11	170	0.37
C16	102	0.11	155	1.17
C17	110	0.06	171	0.60
C18	99	0.05	169	0.24

Table 5.4: Load cells readings at 1575 KN and 2452 KN clamping loads (Continued)

Table 5.4: continued

E1	146	0.24	229	2.10
E2	122	0.08	184	2.40
E3	78	0.04	132	0.15
E4	117	0.03	114	1.31
E5	126	0.06	178	0.93
E6	126	0.06	178	0.93
E7	97	0.10	154	0.42
E8	44	0.04	67	0.80
E9	36	0.02	50	0.45
E10	14	0.03	33	0.09
E11	160	0.46	243	2.61
E12	87	0.07	146	0.11
E13	103	0.05	153	1.20
E14	102	0.07	150	0.72
E15	85	0.06	130	0.14
E16	62	0.22	102	0.27
E17	87	0.06	145	0.27

Load Cell ID #	Expected Load (KN) at 1575 KN clamp	Expected Load (KN) at 2452 KN clamp	Load Cell ID #	Expected Load (KN) at 1575 KN clamp	Expected Load (KN) at 2452 KN clamp
C1	143	222	E1	156	242
C2	99	154	E2	136	221
C3	114	178	E3	104	252
C4	113	176	E4	88	210
C5	80	125	E5	83	189
C6	57	89	E6	89	154
C7	46	71	E7	85	161
C8	52	81	E8	22	120
C9	60	94	E9	8	158
C10	80	125	E10	10	136
C11	57	89	E11	156	242
C12	46	71	E12	136	221
C13	52	81	E13	104	252
C14	60	94	E14	88	210
C15	143	222	E15	83	189
C16	99	154	E16	89	154
C17	114	178	E17	85	161
C18	113	176			

Table 5.5: Expected load cells loading from the simulation model

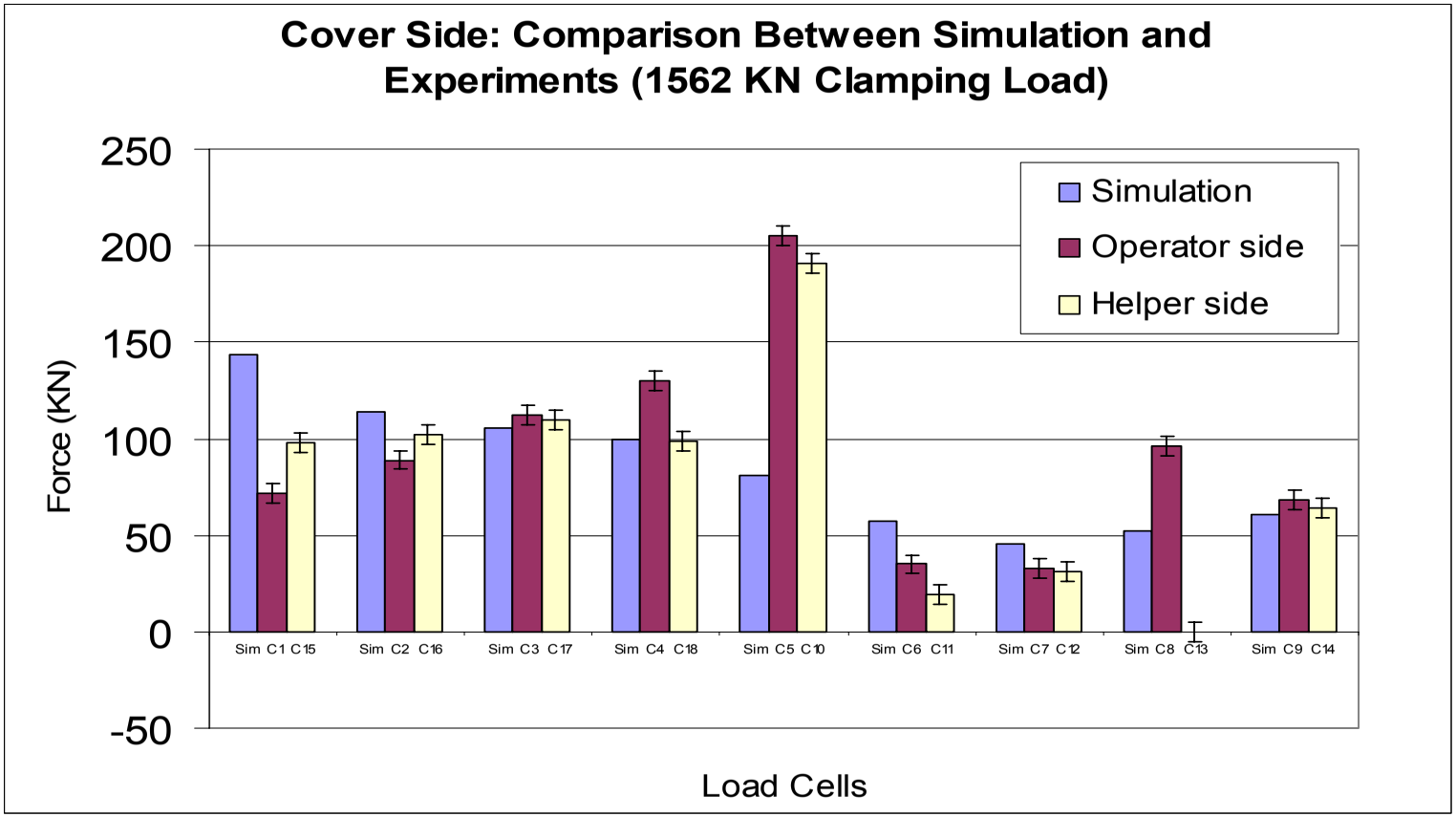

Figure 5.8: Comparison between measured and predicted load cells loading in cover side for clamping load 1575 KN

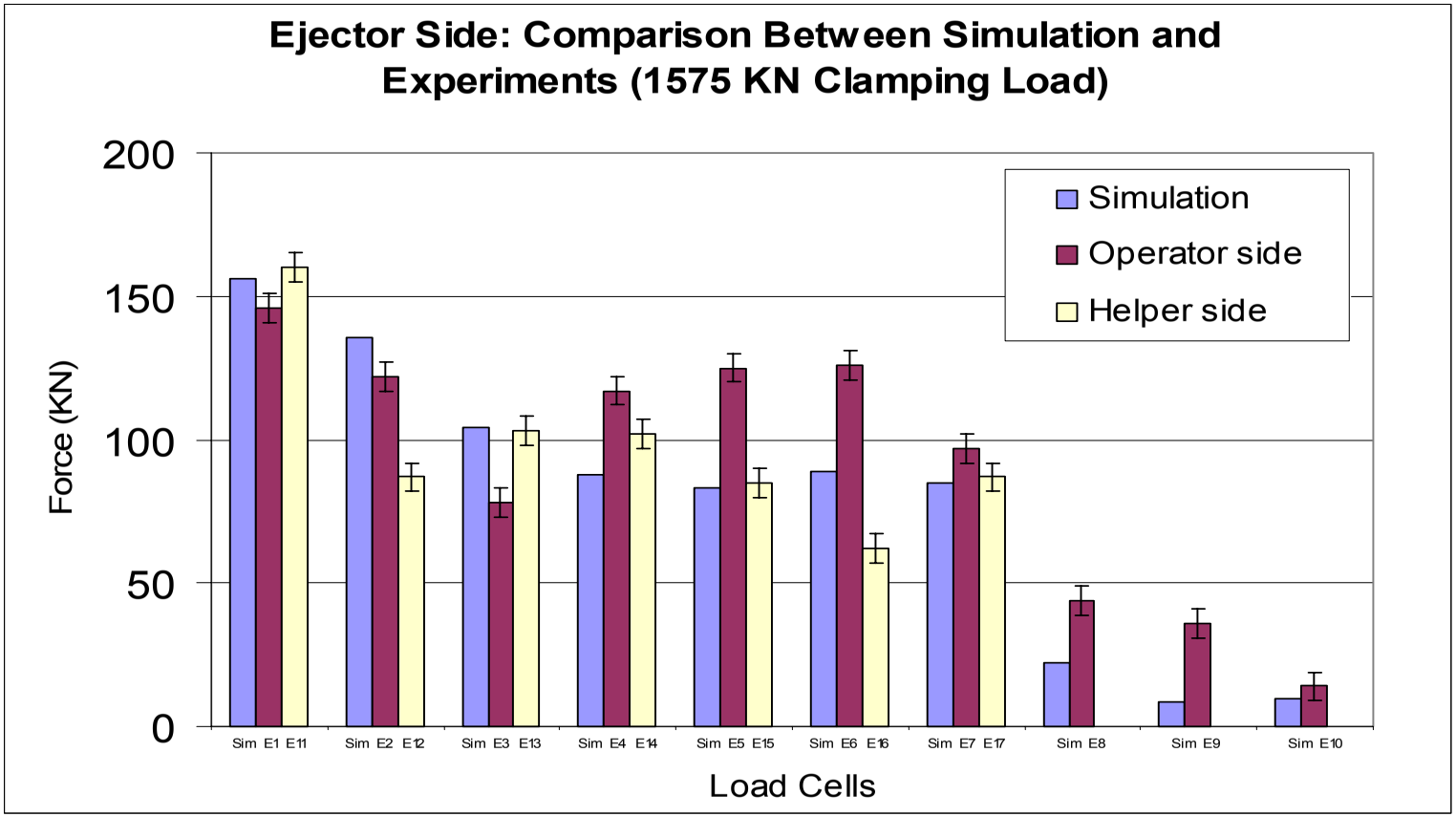

Figure 5.9: Comparison between measured and predicted load cells loading in ejector side for clamping load 1575 KN

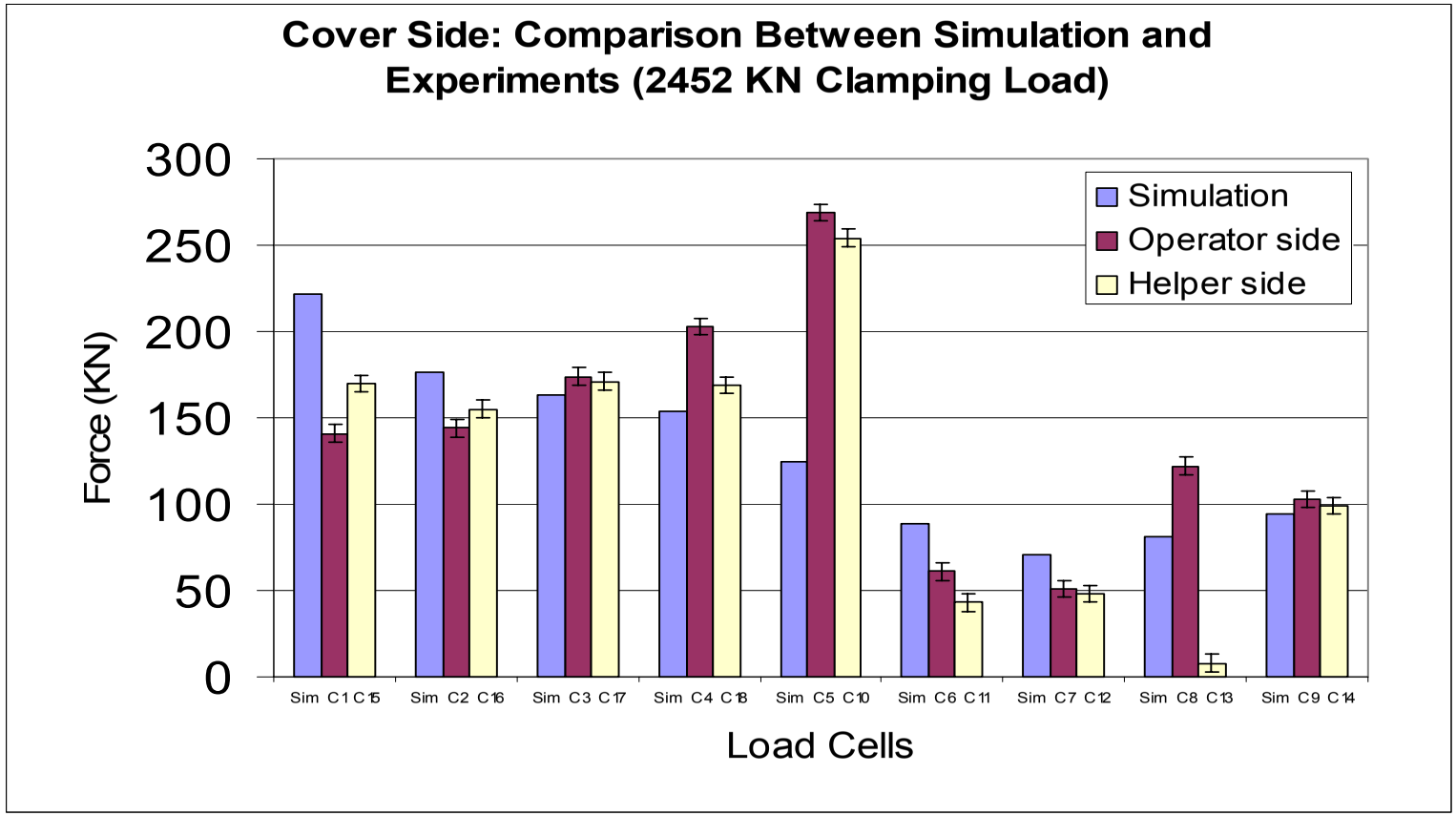

Figure 5.10: Comparison between measured and predicted load cells loading in cover side for clamping load 2452 KN

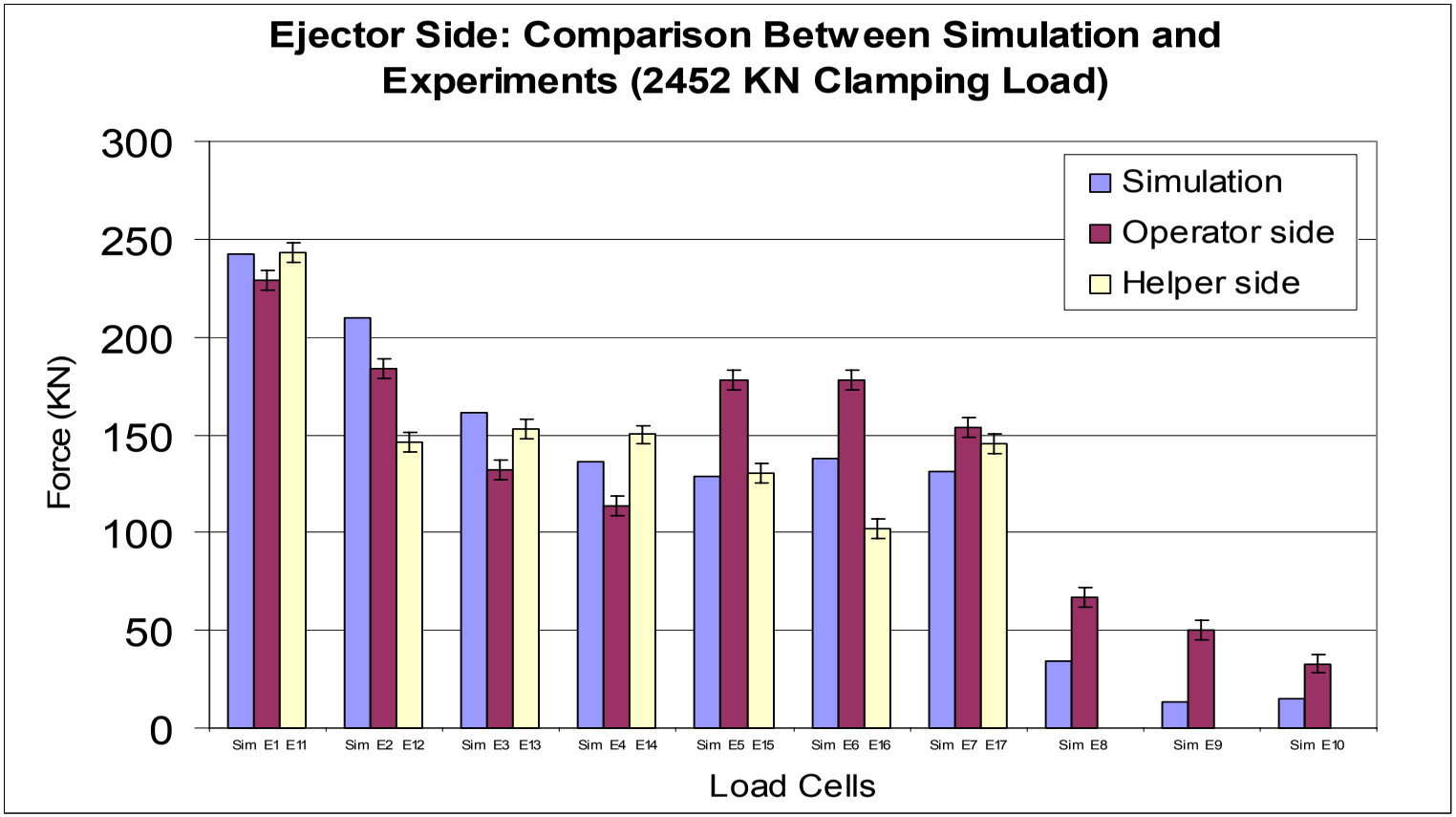

Figure 5.11: Comparison between measured and predicted load cells loading in ejector side for clamping load 2452 KN

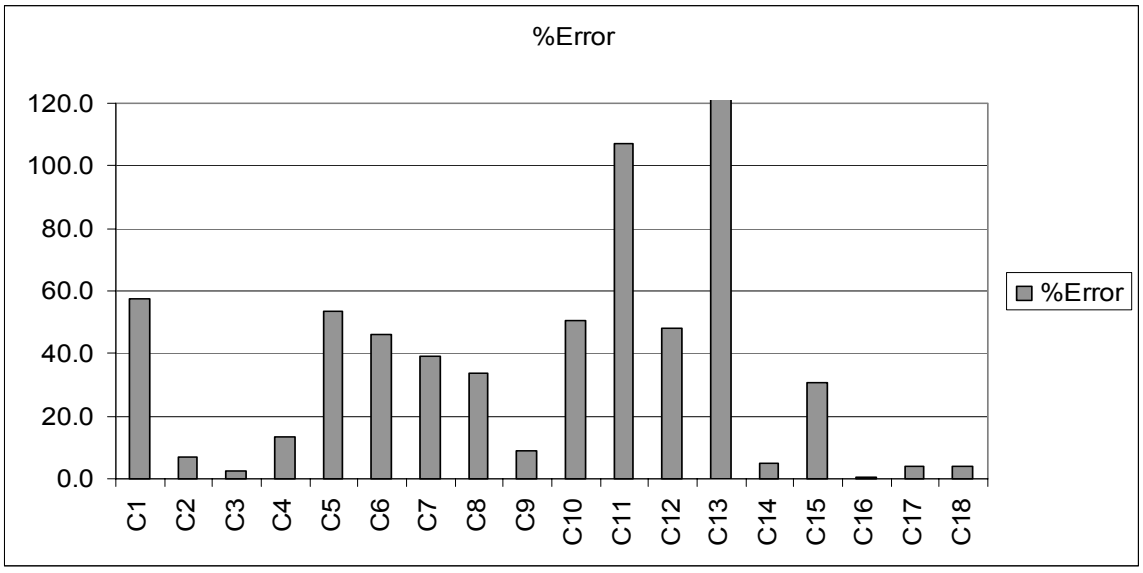

Figure 5.12: % Error for the cover side load cells at 2452 KN clamping load

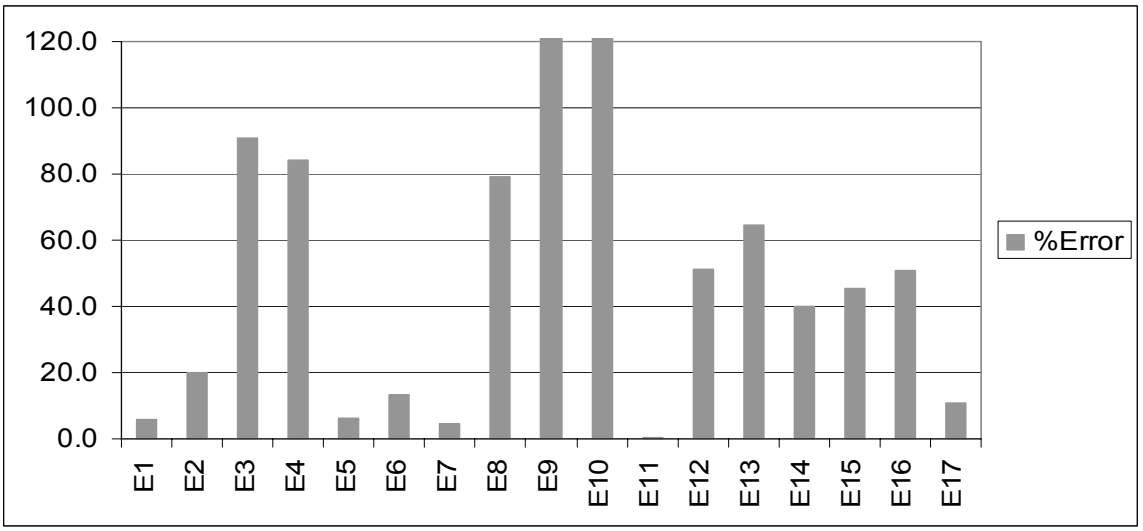

Figure 5.13: % Error for the ejector side load cells at 2452 KN clamping load

5.2.1.2 Tie bar strain gages

Table 5.6 shows the average of the readings and the standard deviation for the measured strains in each tie bar. The table also shows the simulation model predicted values for the longitudinal strains in the tie bars.

	Clamping Load 1562 KN			Clamping Load 2418 KN		
	Average measured strain (μ strain)	Standard Deviation (μ strain)	Simulation Prediction (μ strain)	Average measured strain (μ strain)	Standard Deviation (μ strain)	Simulation Prediction (μ strain)
TB1	261	0.42	233	386	0.57	361
TB2	259	0.39	275	404	0.57	426
TB3	244	0.17	233	367	0.82	361
TB4	265	0.37	275	409	1.25	426

Table 5.6: Strains at tie bars from strain gages and simulation model.

Figures 5.14 & 5.15 show comparisons between the simulation predictions and experimental measurements for tie bars strains at loads 1575 KN and 2452 KN respectively. The figures show very good symmetry between the tie bars on both sides of the symmetry plane. A very good match is also noticed between the simulation predictions and the experiment measurements.

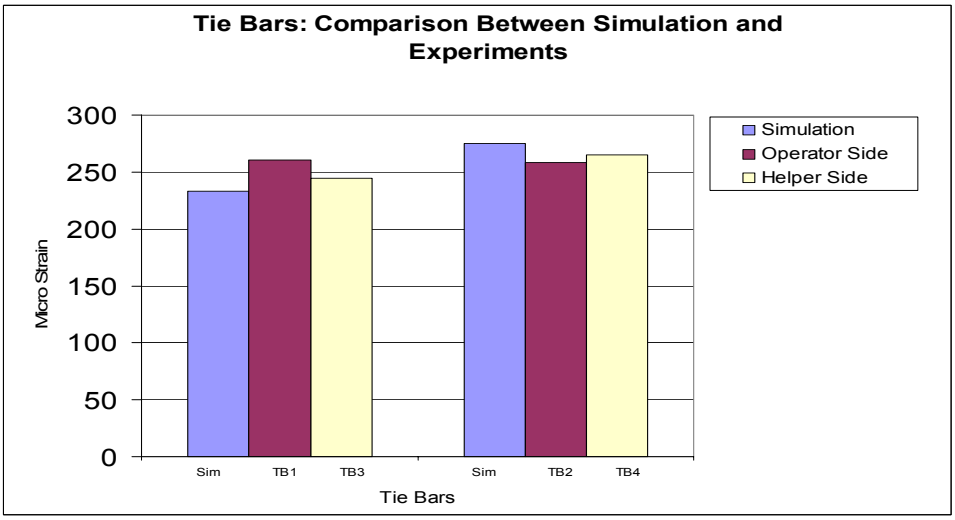

Figure 5.14: Comparison between measured and predicted longitudinal strains in tie bars at 1575 KN clamping load

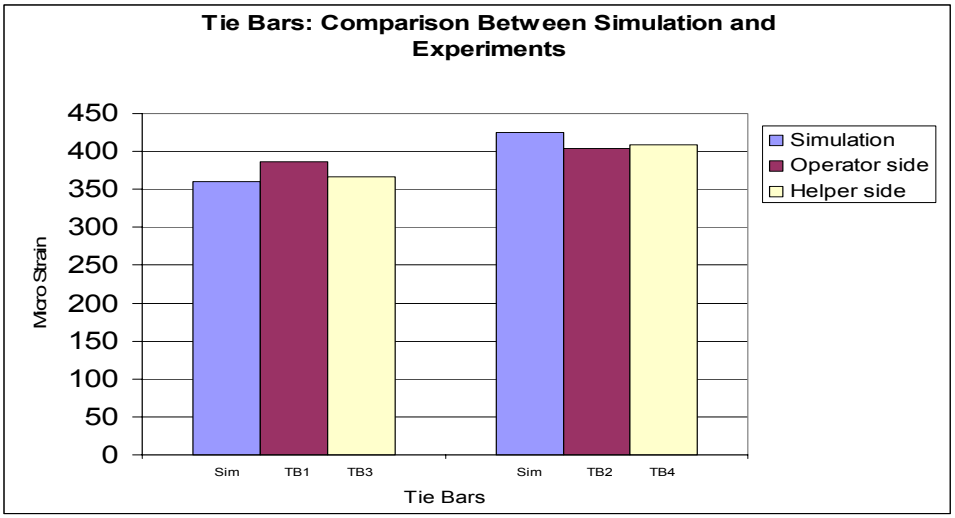

Figure 5.15: Comparison between measured and predicted longitudinal strains in tie bars at 2452 KN clamping load

5.2.1.3 Dies strain gages

Tables 5.7 & 5.8 show the dies strain gages readings and simulation model predictions respectively. Figures 5.16, 5.17 and 5.18 show a comparison between the predicted and measured strains in the dies for X, Y and Z directions.

Strain gage location	Direction	Measured strain (μ strain)	Strain gage location	Direction	Measured strain (μ strain)
CD1	Y	58	ED1	Y	11
	Z	-175		Z	-128
CD2	Y	46	ED2	X	97
	Z	-147		Z	-20
CD3	X	-93	ED3	Y	27
	Z	38		Z	-119
CD4	Y	51			
	Z	-47			
CD5	Y	44			
	Z	N/A			

Table 5.7: Measured strains in the cover and ejector dies at 2452 KN clamping load

Strain gage location	Direction	Simulation predicted strain (μ strain)	Strain gage location	Direction	Simulation predicted strain (μ strain)
CD1	Y	64	ED1	Y	32
	Z	-179		Z	-184
CD2	Y	67	ED2	X	100
	Z	-204		Z	-22
CD3	X	-45	ED3	Y	32
	Z	14		Z	-184
CD4	Y	67			
	Z	-204			
CD5	Y	64			
	Z	-179			

Table 5.8: Simulation predicted strains in the cover and ejector dies at 2452 KN clamping load

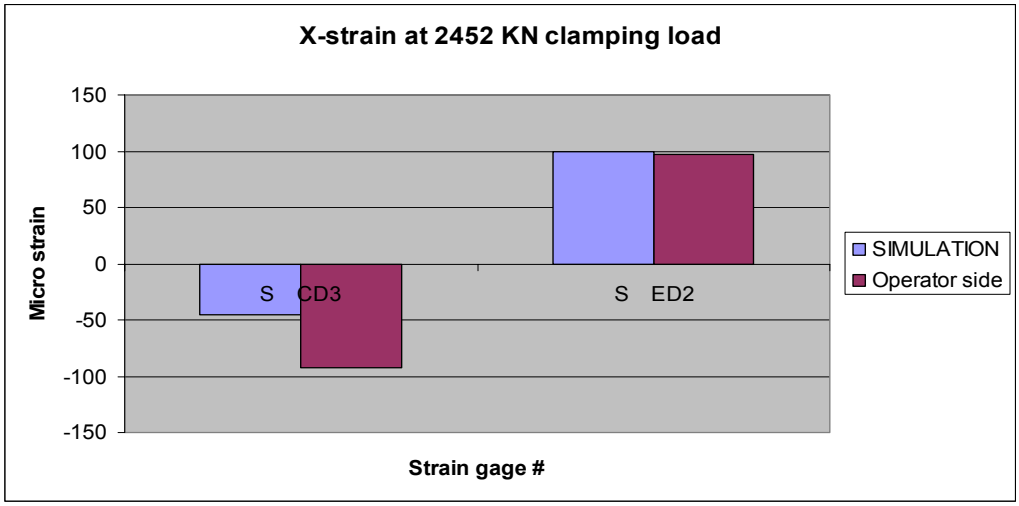

Figure 5.16: Comparison between measured and predicted strains in dies at 2452 KN clamping load (X-direction)

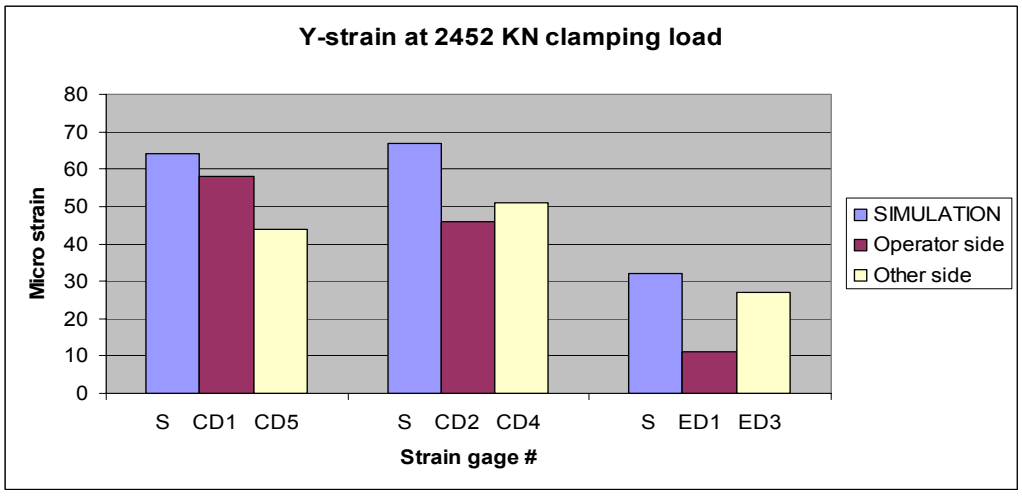

Figure 5.17: Comparison between measured and predicted strains in dies at 2452 KN clamping load (Y-direction)

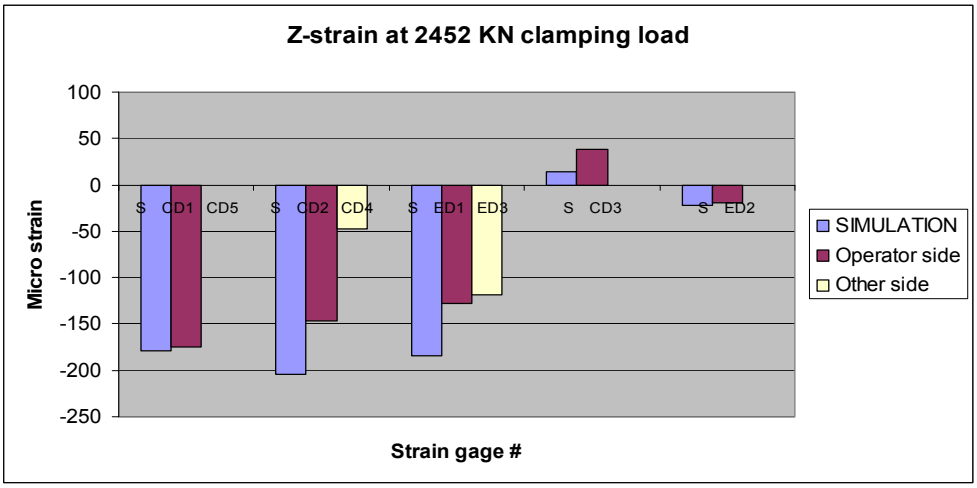

Figure 5.18: Comparison between measured and predicted strains in dies at 2452 KN clamping load (Z-direction)

Figures 5.14-5.16 show a generally good match between the simulation predictions and the strain gages readings. All the strain gages show the same strain patterns, although the values are different. Figure 5.14 shows a very good match between the simulation predictions and the strain gages readings at the ejector side. The reading at the cover side, though showing the same strain pattern, has a significant different value from the simulation prediction. For the Y-direction strains, given by Figure 5.15 all the strain gages show a good match except ED1. For the Z-direction strains, given by Figure 5.16 a good match is noticed except for strain gages CD3 and CD4. CD5 strain gage did not work.

Comparing the results from tie bars and from dies we can conclude that the strain gages readings on tie bars match the simulation predictions much better than the die strain gage readings. Several reasons may contribute to this fact. The first expected

reason is the high surface finish of tie bars compared to the rough surface finish of the dies. The surface finish is a very important factor for the strain gage mounting and hence its accurate reading. A second reason is that, the model assumes that the die casting machine is symmetric around one plane and hence only half of the machine is modeled. Although the tie bars strains proves that the machine is symmetric, the dies may not be that symmetric and hence different readings are expected. The third reason is that, in the simulation model the dies are very much affected by the boundary conditions than the tie bars. The type of contact definition between the dies and platens can cause artificial effects on the strains in the dies.

5.2.2 Load Condition II

At this load condition, actual casting process took place. 67 castings were produced. These castings are the same ones used for comparison with the simulation results in chapter 4. The clamping load was 2500 KN, and the intended cycle time was given in Table 5.1. Since pouring, spraying and extraction were done manually, the actual time was different than 40 seconds. However, most of the cycle times ranged between 40 and 60 seconds.

5.2.2.1 Load cells

Figures 5.19 and 5.20 show the readings from four load cells at each side during one cycle. The figures also show the simulation prediction for the same load cells. The selected load cells are a very good representation for the other load cells

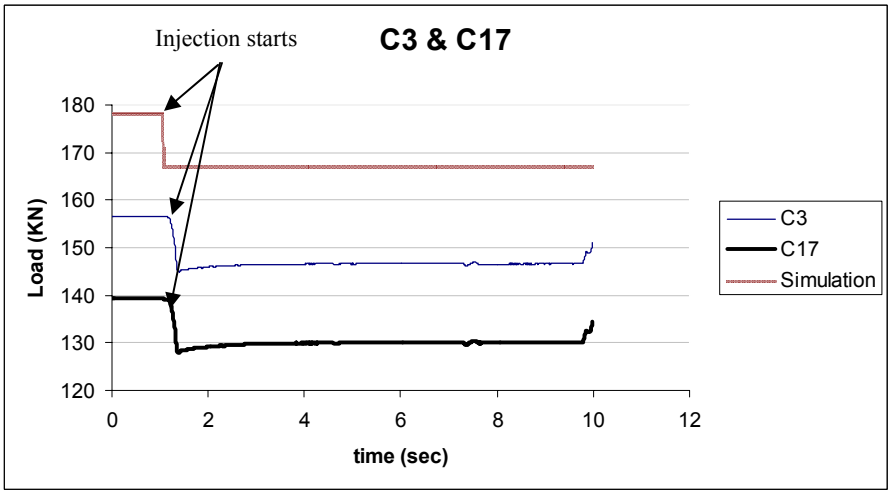

(a)

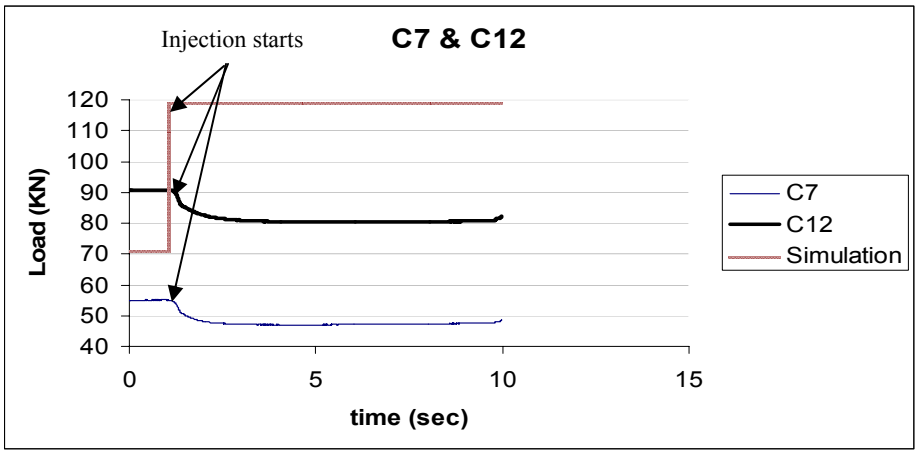

(b)

Figure 5.19: Load pattern at load cells C3, C17, C7 and C12 during one cycle

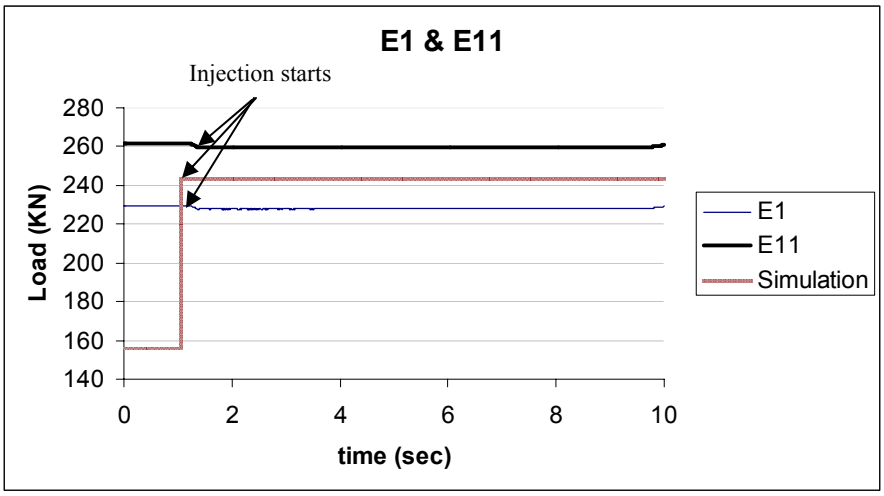

(a)

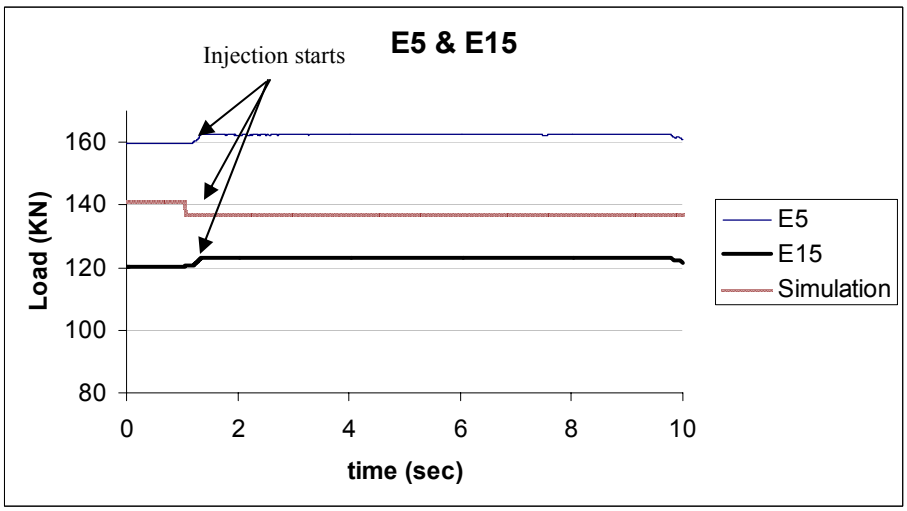

(b)

Figure 5.20: Load pattern at load cells E1, E11, E5 and E15 during one cycle

Figure 4.19 demonstrates that the load cells readings at the cover side decreases after intensification. This applies to all load cells on the cover side. The summation of the readings of the load cells at the cover side decreased by 10% after intensification. On the other hand the simulation results showed different patterns. The load cells behind the cavity predicted more load after intensification, while the load cells far from the cavity predicted less load. The summation of the load cells predicted loads by the simulation is constant and it is not affected by the intensification pressure.

The pattern in the ejector side was different than on the cover side, as shown in Figure 4.20. The load cells readings reflected no significant change in the readings after adding intensification. Again the simulation predictions were different. The upper load cells of the die predicted more load after intensification, while the lower load cells predicted less load. In the simulation and the experiment the summation of the load cells reading at the ejector side did not change after intensification.

The main reason for the differences between the simulation and experimental measurements patterns, after intensification, is the stiffness of the machine. In the model the machine is stiffer than what it is actually. Figure 5.21 shows a schematic drawing and a free body diagram for the machine. In the machine the tie bars and the toggle system are attached to a third platen at the back of the machine. The deformation of this platen due to the intensification pressure relaxes the load slightly on the cover platen and stretches the tie bars. In the simulation the rear platen is not modeled. The tie bars and toggle system are completely restrained at their ends in the space and hence no deformation occurs at their ends.

Another difference between the machine and the model is the support frame behind the cover platen. Three support bars transforms the load from the cover platen to the support frame, Figure 5.21. The support frame also carries the reaction force from the piston during intensification. The support frame and the three support bars are not modeled.

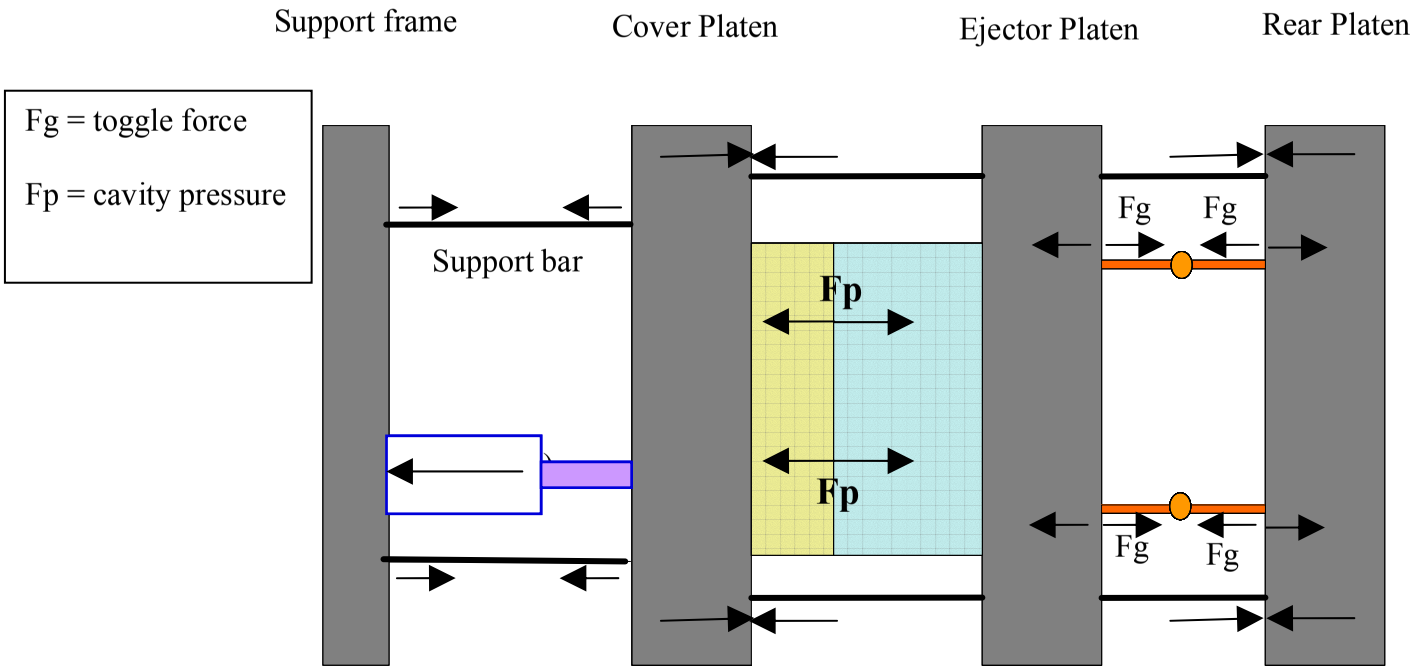

Figure 5.21: A schematic drawing and a free body diagram of the machine

5.2.2.2 Tie bars strain Gages

Figure 5.22 shows the strains measured in the tie bars and the strains predicted by simulation for one casting. The figure shows a very good match between the simulation model predictions and the strain gage readings. The figure also shows that the strain in the tie bars increases after intensification. The reason for this attitude is was explained in the previous section.

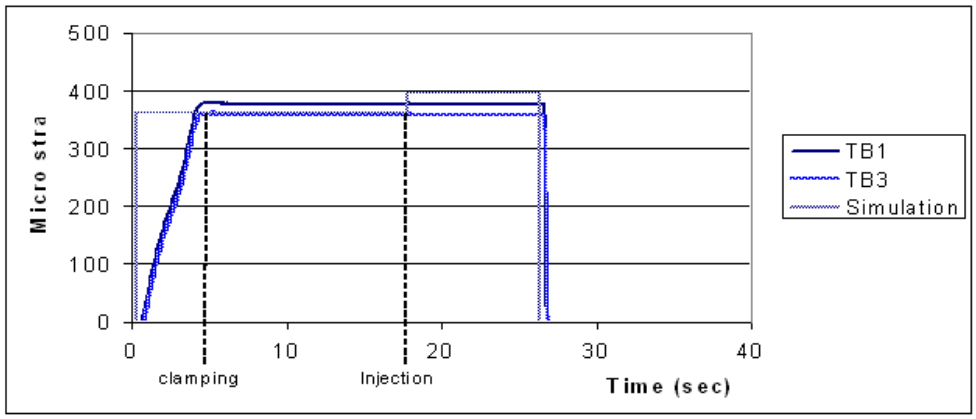

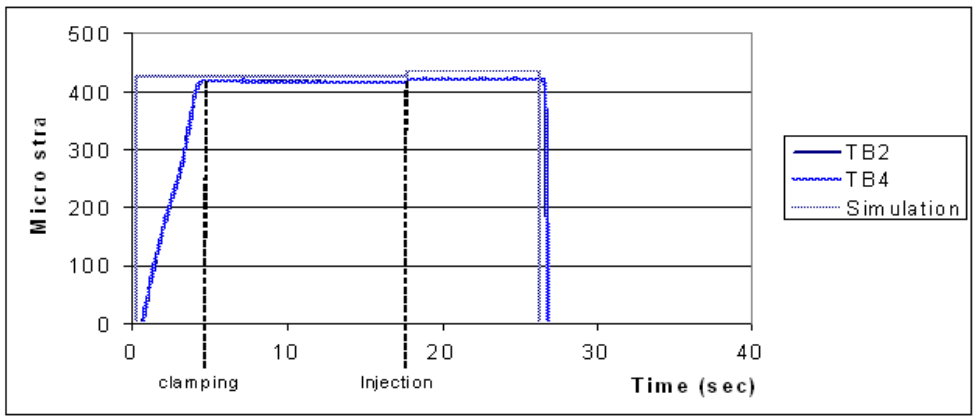

Figure 5.22: Strain pattern at tie bars TB1&TB3 (a) and TB2&TB4 (b) during one cycle

5.2.2.3 Dies strain gages

Figures 5.23, 5.24 and 5.25 show a comparison between the measured strains in the cover and ejector dies and the simulation predictions for X, Y and Z directions respectively. The figures show that there is good match at some locations, while some other locations show completely different patterns between simulation and experiments. The reasons for the different readings in the die strain gages were discussed before in section 5.2.1.3. Another factor for noise results predicted by the simulation is the interaction between the stress analysis and the temperature distribution. The large differences that can be seen in Figure 5.23 and 5.24 occurred in the simulation due to the effect of temperature. This looks like a numerical error rather than an actual change in the strain.

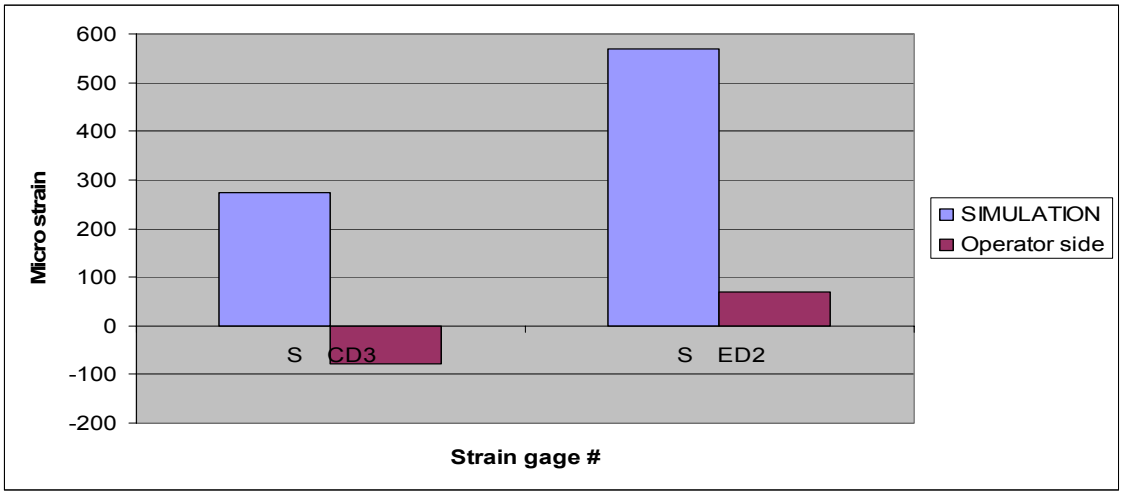

Figure 5.23: Comparison between measured and predicted strains in dies at load condition II (X-direction)

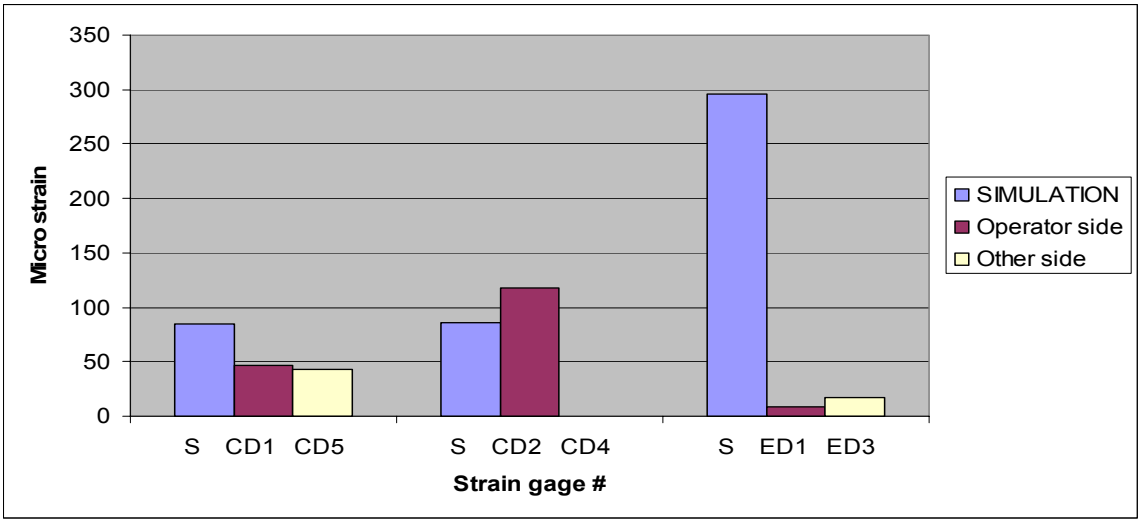

Figure 5.24: Comparison between measured and predicted strains in dies at load condition II (Y-direction)

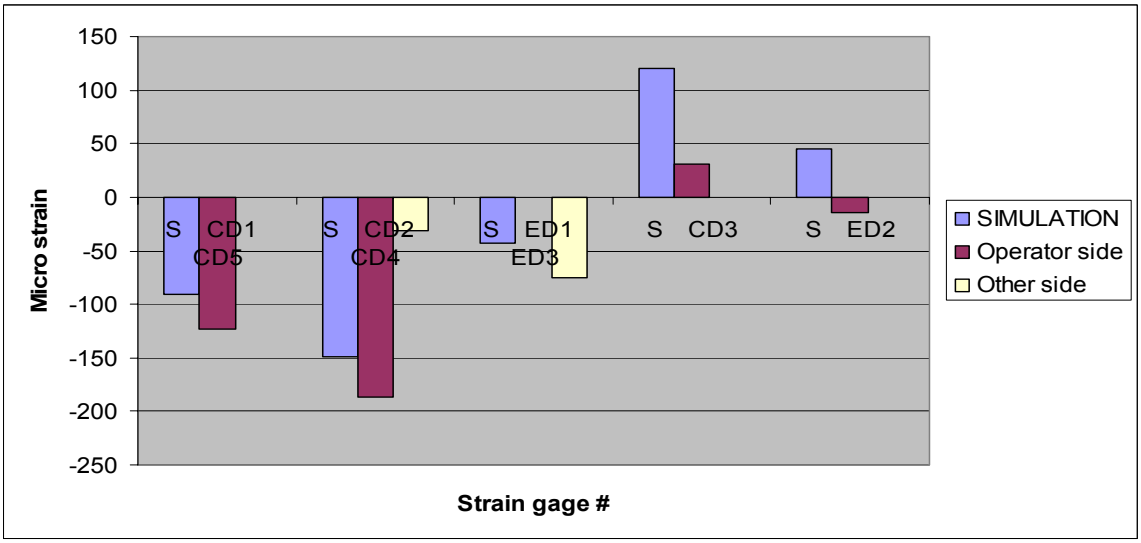

Figure 5.25: Comparison between measured and predicted strains in dies at load condition II (Z-direction)

5.2.2.4 Thermocouples

As mentioned earlier in this chapter, four thermocouples were inserted in both dies to measure the temperature inside the die steel. The locations of the thermocouples are given in Figure 5.7. Due to problems with the cement used to fix the thermocouples in the fixtures, they did not work as intended. Only thermocouple T3 worked correctly. Figure 5.26 shows the readings of thermocouple T3 for 14 cycles. Figure 5.27 shows the simulation predictions of temperatures for the same thermocouple. A very good match in the pattern is shown between the two figures although some differences in the values are noticed. Simulation predictions are 30^{o}C lower than the thermocouple measurement after the same number of cycles. Many reasons may contribute to this difference. The first expected reason is the furnace temperature. The furnace used in the die casting facility is old and controlling its temperature is a challenge. It is very likely that the pouring temperature was higher than what was expected. The second reason is the manual control of the pouring and idle time periods. These two time periods are constant in the simulation, while in the actual casting they change significantly. The third reason is related to the model where the heat transfer coefficient between casting/inserts, inserts/dies and inserts/air may vary from the values during the experiment. Considering all these sources of variability, the simulation predictions are considered very consistent with the experimental measurements.

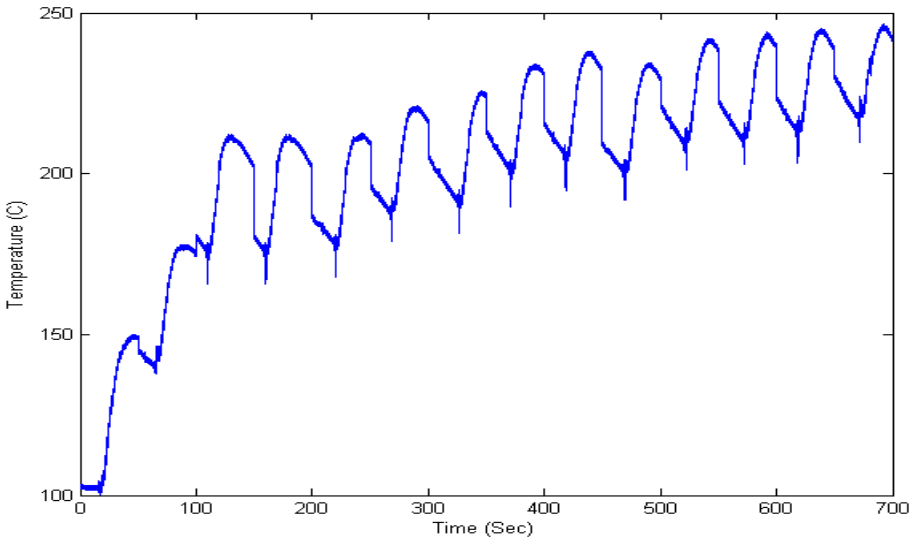

Figure 5.26: Thermocouple T3 readings versus time

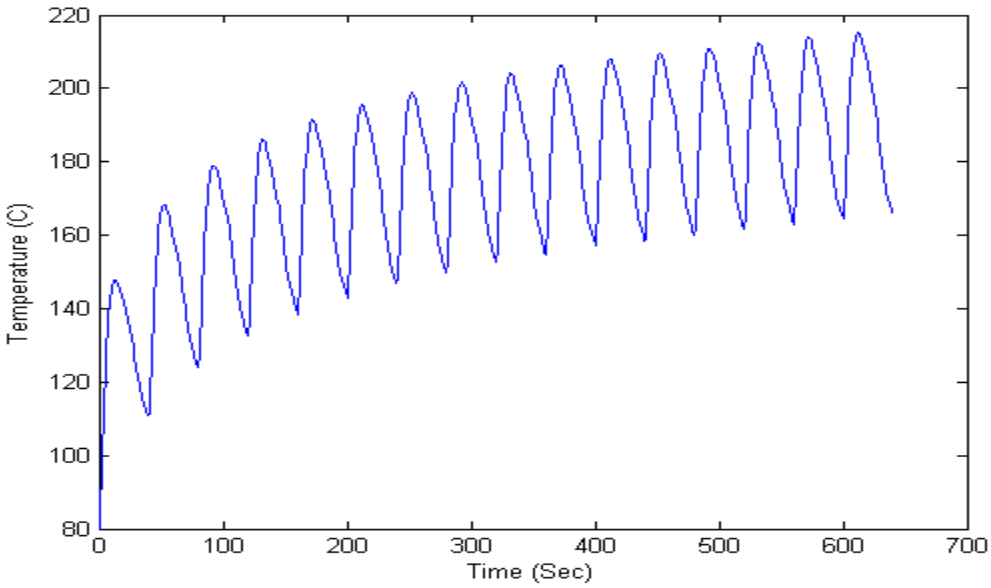

Figure 5.27: Simulation predicted temperatures for thermocouple T3 versus time

CHAPTER 6

CONCLUSIONS AND FUTURE WORK

The research was devoted to modeling die casting process in order to predict the final casting shape. In order to achieve this goal, a simulation model was built to model the die casting process. An experimental work was conducted to verify and validate the simulation model results. In this chapter the conclusions from both the simulation modeling and experimental work are presented. Suggestions for research continuation and future work are also presented.

6.1 Conclusions

The conclusions are given for the simulation modeling and the experimental work separately. The simulation modeling conclusions are related to the modeling techniques used in the analysis, the effects of different factors on the simulation results and comparison between the casting distortion predictions and experimental measurements. The experimental work conclusions are linked mostly to the machine model and its matching to the actual machine.

6.1.1 Simulation model conclusions

A coupled thermal-mechanical finite element model was created to simulate the die casting process in order to predict casting distortion and residual stresses. Three material models were used to evaluate the effect of the selected material model on the simulation output. A *design of experiment* (DOE) was conducted to evaluate the effect of four modeling parameters on the simulation. The following are the conclusions from the analysis of the simulation results:

- Most of the residual stresses in the casting are formed inside the die while the casting is restrained by the die steel. After ejection, and during cooling to room temperature, the residual stresses decrease and the casting relaxes to some extent. The amount of relaxation predicted by the simulation depends on the material model used.
- Using the elastic material model to simulate the mechanical behavior of the casting overestimates the predicted residual stresses. The elastic-plastic material model shows much less stresses than the elastic one. The elastic-viscoplastic material model predicts the lowest values of residual stresses. Using the viscoplastic material models is increasing widely in the area of casting modeling, but the unavailability of the required material properties for aluminum alloys eliminates the efficient use of this model in die casting at present.

- Most of the casting distortion happens after ejection during cooling down to room temperature. Before ejection the casting is restrained by the die steel and therefore cannot distort freely at the restrained directions. In numerical values, the distortion values at ejection were about 10-20% of the distortion at room temperature.
- Different material models did not affect the distortion patterns of the casting at ejection, although the distortion values were different. This is reasonable recalling the fact that the distortion before ejection is limited by the die steel.
- At room temperature the different material models resulted in only slightly different distortion patterns. Thus the distortion pattern is not very sensitive to the selected material model in the simulation. The distortion values were different among the different material models. The measured casting dimensions, at room temperature, changed by 0.5 - 0.9 %, 0.8 – 1.0 % and 0.60 – 0.88 % from the solid model dimensions in the elastic, plastic and viscoplastic models respectively.
- The DOE results for the ejection temperature looked very reasonable. Only the heat transfer coefficient and the injection temperature affected the ejection temperature.
- The yield strength had the major effect on the residual stresses in the casting at ejection, while the injection temperature and heat transfer coefficient had the main effect on the residual stresses at room temperature. The DOE results also show a significant effect of the interaction between the ejection temperature and stresses. This research intended mainly to show the

significance of the material properties on the final casting distortion. Research is needed to develop the correct material properties of the aluminum alloys used in die casting.

- Final casting distortion is a function of the interaction between the temperature and stresses at ejection rather than being a function of different modeling factors separately.
- Increasing the injection temperature increases the casting distortion. This was a common trend in all the simulation results. Physically, this is very reasonable, since more heat means more shrinkage and hence more thermal strains.
- Some cases showed very good match between the predicted and measured values for dimensions D1, D2 and D3 (Figure 4.17) along the parting plane.
- The simulation model under estimated the distortion value of dimension H (Figure 4.17) across the parting plane. This is due to the lack of hydrostatic pressure inside the casting and the effect of die separation on this dimension. The casting in the simulation model cannot behave as a liquid and fill the separation between the two dies. Also the separation calculated by the model would not be the same as the separation in the machine for two reasons: The first reason is that the machine model used is stiffer than the actual machine (section 5.2.2.1). The second reason is that the separation is affected by the dynamic loads which are not included in the model.
- Related to the previous point, the simulation model predicts flatter back surface of the casting than the measured castings. This surface is located

across the parting plane, and the discussion in the previous point applies to this point. However the predicted values of flatness lied within the experimentally measured range for all the simulation cases.

- Quenching the casting in water after ejection did not show any significant difference both in the simulation and the experimental measurements.
- The final casting shape is a function of the ejection temperature and residual stresses and ignoring the stresses leads to a wrong solution. Running the simulation cases with removing the stresses from the casting upon ejection led to an under estimated distortion for all the measured dimensions. In numerical values, about 24-38% of the final distortion was resulted by the ejection residual stresses.
- Using the coupled thermal mechanical analysis was very costly both in preparing the model and running it. The main goal of using the coupled analysis was to include the effect of gap formation on heat transfer coefficient and the temperature dependence of material properties. From the simulation results, there was no gap except at the biscuit and runner area which are artifact of boundary conditions rather than a correct phenomenon. Also it is possible to include the temperature dependence of material properties in the uncoupled analysis with high accuracy except for the viscoplastic analysis. Due to these facts it is advised to use the uncoupled analysis for design and industrial purposes.
- The running time for elastic analysis was about 12 hours, where the running times for plastic and viscoplastic analysis were about 4 and 40 days

respectively. These numbers shows that the material model affects significantly the simulation cost. So, as an advice, if only the distortion patterns are needed, it is more efficient to run an elastic analysis. If the residual stresses are needed, the elastic plastic analysis should be used. The viscoplastic analysis is not useful unless the material data are available. However, very high costly simulation should be expected.

The variation of the casting distortion predicted by different simulation models, was larger than the variation of the experimental measurements for the dimensions along parting plane. The reason was that the simulation was able to cover a wide range of modeling factors levels. Prior to this work, many practitioners predicted that the variation in distortion measurements would be so large that simulation predictions would be useless for practical applications. These results show that the simulation can predict the casting distortion, if the adequate modeling parameters were selected.

The comparison between the casting measurements and the simulations predictions demonstrated the significance of the residual stresses on the casting distortion. Casting simulation models should include this effect of residual stresses in order to predict accurate casting distortion.

6.1.2 Experimental work conclusions

To validate the die casting machine model an experimental work was conducted on the 250 ton BUHLER die casting machine available in the Net Shape Manufacturing lab at Ohio State University. A total of 71 sensors were installed on the machine parts.

Only 68 sensors were working during the machine run. These are 35 load cells, 16 tie bar strain gages, 15 die strain gages and one thermocouple in the cover insert. The following are the conclusions from the analysis of the experimental results:

- The load cells measurements were very repeatable with very low standard deviation compared to the average reading.
- The loading patterns of the load cells were very much the same as the simulation predictions except in the location of maximum loading.
- At load condition I (clamping load) most of the load cells showed good match with the simulation predictions.
- During load condition II (i.e. casting), the response of the load cells to the intensification pressure was different from the simulation predictions. On the cover side, the experimental reading showed that the total load on the load cells decreased by about 10% and every load cell lost some of its loading after intensification. The total load in the simulation was constant and some of the load cells lost a part of its loading, while the others gained more load after intensification. The reason is the high stiffness of the machine model compared to the actual machine stiffness. The high stiffness resulted from the lack of the rear platen and the cover platen and the ejector mechanism support frame.
- The tie bar strain gages showed very good match with the simulation predictions at both load conditions I and II.

- The die strain gages showed good match with the simulation predictions at load conditions I . The match was not very good as the match in the tie bar strains due to several reasons:
    - The rough surfaces of the dies compared to the highly finished surfaces of the tie bars
    - Effect of temperature on the die strain gages.
    - The lack of perfect symmetry in the die.
    - The effect of boundary conditions, in the simulation model, on the dies is more severe than the effect on the tie bars.
- During load condition II, good match between the die strain gages readings and the simulation was not achieved.
- The thermocouple measurements showed the same pattern as the simulation model. Some differences in the temperature values were noticed but not significant.

A simple machine model, like the one that was used in this research, is capable of predicting the load distribution on different machine parts with accepted accuracy. Such a model might be very useful for die casting dies and machines design. On the other hand, a more comprehensive model is needed if higher accuracy is needed.

6.2 Future work

The research studied modeling the die casting process in order to predict the casting distortion. The research provided insights to different modeling techniques and criteria. The research also provided experimental work to verify and validate the simulation model. Several modifications can be added to the model to enhance its predictions:

- *Modeling the rest of the machine parts*. Adding more machine parts to the model will facilitate better solutions. An example for the parts that can be added is the rear platen and the toggle system.
- *Enhancing the material model of the casting*. The stress-strain curve of the casting material needs to be defined at as many temperatures as possible to avoid jumps between the stress or strain values. Also the stress-strain curve must be smoothed to avoid any sharp corners.
- *Modifying the Design of Experiment*. The DOE needs to be modified to include the interaction between the different factors. Also some factors may be added as, for example, the cavity pressure and cooling lines.
- *Liquid simulation*. This would be the most important enhancement to the model. In this modification the casting should work as a liquid at temperatures over the liquidus and as a solid at lower temperatures. This is not possible using the ABAQUS software, and search is needed for another software that may offer this facility.

LIST OF REFERENCES

1. Foundrymen's handbook (1929), The penton publishing Co., Cleveland, Oh.

2. Analysis of Casting Defects (1947), The American Foundarymen's Association, Chicago, Illinois.

3. Anonymous (Fall 1983), Designing to Avoid Casting Strain, Casting Engineering & Foundry World, v 15, n 3, p40- p48.

4. Parkins, R.N. and Cowan, A. (1953-1954), The Mechanism of Residual-Stress Formation in Sand Casting, Journal of the Institute of Metals, Vol.82, p1- p8.

5. Thomas, B. G. (1995), Issues in Thermal-Mechanical Modeling of Casting Processes, ISIJ International, v 35, n 6, p 737- p743.

6. Thomas, B.G. (1993), Stress Modeling of Casting Processes: An Overview, Modeling of Casting, Welding and Advanced Solidification Processes VI, p519-p534.

7. Chayapathi, A., Kesavan, V. and Miller, R.A. (1999), The Effects of Die and Machine Variables on Die Deflection, Transactions 20th International Die Casting Congress and Exposition, North American Die Casting Association, Cleveland, Oh., p169-p176.

8. Arrambide, A. and Miller, R. A. (1999), Finite Element Modeling of Slide Distortion in a Transmission Casing Die, Transactions 20th International Die Casting Congress and Exposition, North American Die Casting Association, Cleveland, Oh.,p91-p102.

9. ABAQUS version 5.8 Manual (1998), HKS Inc., USA.

10. Zhang C. (2001), Design of a Load Cell Configuration for Die Deflection Experiments**,** Thesis (M.S.),Ohio State University.

11. Campbell, J., (October 1991), Solidification Modeling: Current Limitations and Future Potential, Materials Science and Technology, V 7, n 10, p 885- p894.

12. Barone, M.R. and Caulk, D.A. (2000), Analysis of Liquid Metal Flow in Die Casting, International Journal of Engineering Science, 38, p1279- p1302.

13. Lewis R.W. Ravindran K. and Huang H.C. (1991), Casting Modeling by Finite Elements - Our Experience, Modeling of Casting, Welding and Advanced Solidification Processes V, The Minerals, Metals & Materials Society, p3- p14.

14. Lewis, R.W. and Ravindran, K. (2000), Finite Element Simulation of Metal Casting, International Journal for Numerical Methods in Engineering, 47, p29- p59.

15. MAGMASOFT 4.0 Manual (2000), MAGMA Inc., Germany.

16. Rosindale, I and Davey, K. (1999), Transient Thermal Model for the Hot Chamber Injection System in the Pressure Die Casting Process, Applied Mathematical Modeling, V. 23, p255- p277.

17. Rosindale, I and Davey, K. (1998), Steady State Thermal Model for the Hot Chamber Injection System in the Pressure die Casting Process, Journal of Materials Processing Technology, V. 82, p. 27- p45.

18. Thomas, B.G., Samarasekera, I. V. and Brimacombe, J.K. (March 1987), Mathematical Model of the Thermal Processing of Steel Ingots: Part I. Heat Flow Model, Metallurgical Transactions B, V. 18B, p119- p130.

19. Thomas, B.G., Samarasekera, I., V. and Brimacombe, J. K. (March 1987), Mathematical Model of the Thermal Processing of Steel Ingots: Part II. Stress Model, Metallurgical Transactions B, V. 18B, p131- p147.

20. Barone, M. R. and Caulk, D. A. (1999), A New Method for Analyzing Cavity Fill in Die Casting, Transactions 20th International Die Casting Congress and Exposition, North American Die Casting Association, Cleveland.

21. Bounds, S., Davey, K., Hinduja, S. (February 2000), An Experimental and Numerical Investigation into the Thermal Behavior of the Pressure Die Casting Process, Transactions of the ASME,V. 122, P.90- p99.

22. Voss, M.J. and Tsai, H.L. (1996), Effects of the Rate of Latent Heat Release on Fluid Flow and Solidification Patterns During Alloy Solidification, International Journal of Engineering and Science, V34, No.6, p715- p7.

23. Nishida, Y., Droste, W. and Engler, S. (1986), The Air Gap Formation Process at the Casting-Mold Interface and the Heat Transfer Mechanism Through the Gap, Metallurgical Transactions B, V. 17B, p833- p844.

24. Hwang, J. C., Chuang, H. T., Jong, S. H. and Hwang, W. S. (1994), Measurement of Heat Transfer Coefficient at Metal/Mold Interface During Cooling, AFS Transactions, V 144, p877-p883.

25. Hou, T. X. and Pehlke, R. D. (1988), Determination of Mold/Metal Interfacial Heat Transfer and Simulation of Solidification of an Aluminum-013% Silicon Casting, AFS Transactions, V 91, p129-p136.

26. Dantzig J. A. (1989), Thermal Stress Development in Metal Casting Processes, Metallurgical Science and Technology, V 7, n 3, p133, p178.

27. Smelser, R. E. and Richmond, O. (1988), Constitutive Model Effects on Stresses and Deformations in a Solidifying Cylinder, Modeling of Casting and Welding Processes IV, The Minerals, Metals & Materials Society, p313- p328.

28. Kelly, J. E., Michalek, K. P., O'connor, T. G., Thomas, B. G. and Dantzig, J. A. (October 1988), Initial Development of Thermal and Stress Fields in Continuously Cast Steel Billets, Metallurgical Transactions A, V19A, p2589-p2601.

29. Zabaras, N., Ruan, Y. and Richmond, O. (Dec 1991), On the Calculation of Deformations and Stresses During Axially Symmetric Solidification, Journal of Applied Mechanics, Transactions ASME. v 58, n4, , p865- p871.

30. Wang, K. C., Ramnarayan, V., Chandrasekharan, S., Cheng, S. and Paul, A. J. (1993), Thermal Stress Analysis of Sand Castings, Computer Applied in Shaping & Forming of Materials, The Minerals, Metals & Material Society, p137- p155.

31. Kristiansson, J. O. (1982), Thermal Stresses in the Early Stage of Solidification of Steel, Journal of Thermal Stresses, V 5, p315-330.

32. Parkins, R. N. and Cowan, A. (1953-1954), The Mechanism of Residual-Stress Formation in Sand Casting.", Journal of the Institute of Metals, V82, p1- p8.

33. www.matls.com

34. Lin, J. C., and Righi, J (1998), Alloy Influence on Filling, Macroshrinkage, Hot Cracking and Properties in Aluminum Shape Castings, Automotive Alloys II, The Minerals, Metals and Material Society, p 45 – p61.

35. Kim, K. Y., Sakuta, H. and Suzuki, T. (1991), Deformation Analysis of Al-7%Si-0.3%Mg Alloy Castings" Modeling of Casting, Welding and Advanced Solidification Processes V, The Minerals, Metals & Materials Society, p259-p264.

36. Makhlouf, M., Apelian, D. and Wang, L. (1998), Microstructures and Properties of Aluminum Die Casting Alloys, NADCA Publication #215.

37. Shames I.H., and Cozzarelli F.A. (1997), Elastic and Inelastic Stress Analysis, Taylor & Francis.
38. David, S. B. (1987), Finite element analysis : from concepts to applications, Addison-Wesley Pub. Co.

39. Zienkiewicz, O. C. (1977), The Finite Element Method, McGraw-Hill Book Company (UK) Limited.

40. Osborne, M. A. (1995), Analysis of the Effects of Die Casting Process Control on Casting Dimensional Variability, Ph.D. Dissertation, Ohio State University.

41. www.omega.com

42. Crisfield, M. A. (1991), Non-linear Finite Element Analysis of solids and Structures, JOHN WILEY & SONS, UK.

43. Drezet, J. M. and Plata, M. (1995), Thermomechanical Effects During Direct Chill and Electromagnetic Casting of Aluminum Alloys. Part I: Experimental Investigation, Light Metals, The Minerals, Metals & Material Socity, p931- p940.

44. Drezet, J. M. and Plata, M. (1995), Thermomechanical Effects During Direct Chill and Electromagnetic Casting of Aluminum Alloys. Part II: Numerical Simulation, Light Metals, The Minerals, Metals & Material Socity, p941- p950.

45. Asbjorn, M. and Holm, E. J. (1991), On the Use of Constitutive Internal Variable Equations for Thermal Stress Prediction in Aluminum Casting, Journal of Thermal Stresses, V14, p571- p587.

46. Okamura, K. and Yamamoto, K. (1993), Coupled Analysis Between Deformation and Heat Transfer of Solidifying Steel Shell in Continuous Casting Mold, Modeling of Casting, Welding and Advanced Solidification Processes VI, the Minerals, Metals & Materials Society, p535, p542.

47. Celentano, D., Oller, S. and Onate, E. (1995), A Coupled Thermomechanical Model for the Solidification of Cast Metals, International Journal of Solids and Structures, V33, N5, p647- p673.

48. Campbell, J. (2000), The Concept of Net Shape Manufacturing, Materials and Design, V21, p373- p380.

49. Gerber, A. G. and Sousa, A. C. M. (1995), Numerical Investigation of the Influence of Air Gaps Upon the Solidification in a Rotary Caster, Journal of Materials Processing Technology, V48, p657-p 665.

50. Goudie, N. J. and Argyropoulos, S. A. (1995), Technique for the Estimation of Thermal Resistance at Solid Metal Interfaces Formed During Solidification and Melting, Canadian Metallurgical Quarterly, V34, N1, p73- p84.

51. Davey, K. and Bounds S. (1997), Modeling the pressure Die Casting Process using Boundary and Finite Element Methods, Journal of Materials Processing Technology, V63, p696 – p700.

52. Bounds, S., Davey, K. and Hinduja, S. (1999), Modeling the Pressure Die Casting Process using Hybrid Finite-Boundary Element Model, International Journal for Numerical Methods in Engineering, V45, p1165- p1185.

53. Hou, T. X., Pehlke, R. D. and Wilkes, J. O. (1991), Computer Simulation of Casting Solidification using a Combination of the Finite Element and Boundary Element Methods, Modeling of Casting, Welding and Advanced Solidification Processes V, p15- p22.

54. Li, B. Q. (1997), Numerical Simulation of Flow and Temperature Evolution during the Initial Phase of Steady-State Solidification, Journal of Materials Processing Technology, V71, p402- p413.

55. Liu, J. C., Anyalebechi, P. N., Sherbad, M. and Bachowski, R. (1991), Coupled Thermomechanical Model for Continuous Bar Casting, Modeling of Casting, Welding and Advanced Solidification Processes V, p229- p236.

56. Nai-yi, L., Louis, G., Hector, J. and Barber, J. R. (1992), Theories of Growth Instability during Solidification of Metals: Part 2. Stress Function Approach, Journal of Materials Processing & Manufacturing Science, V1, p40- p55.

57. Lewis, R. W., Ransing, R. S. (2000), The Optimal Design of Interfacial Heat Transfer Coefficients via a Thermal Stress Model, Finite Elements in Analysis and Design, V34, p193- p209.

58. The Metals Handbook (1961), American Society for Metal, Novelty, Ohio, V1, Page958.

APPENDIX A

DRAWINGS

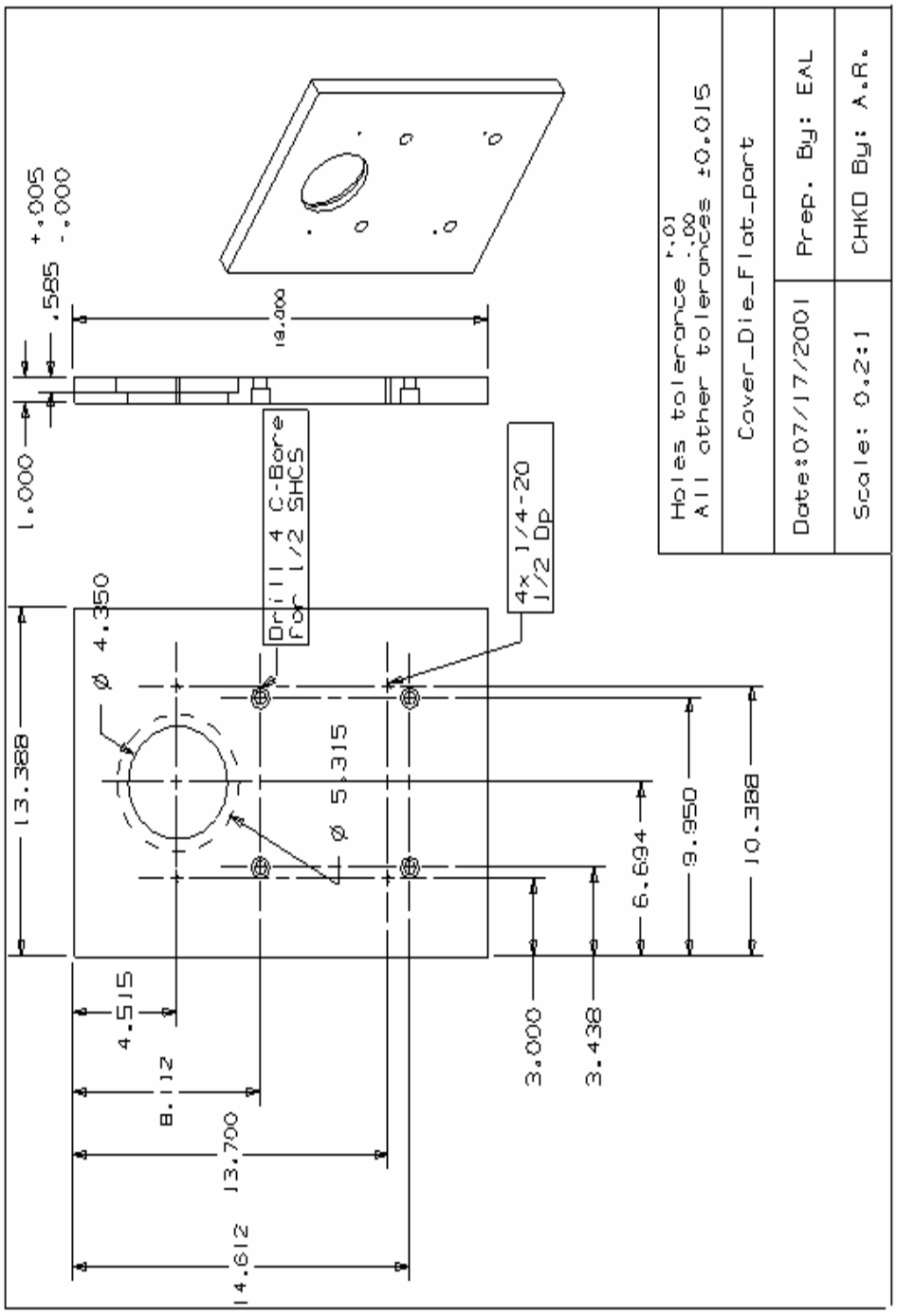

Figure A.1: Cover die plate

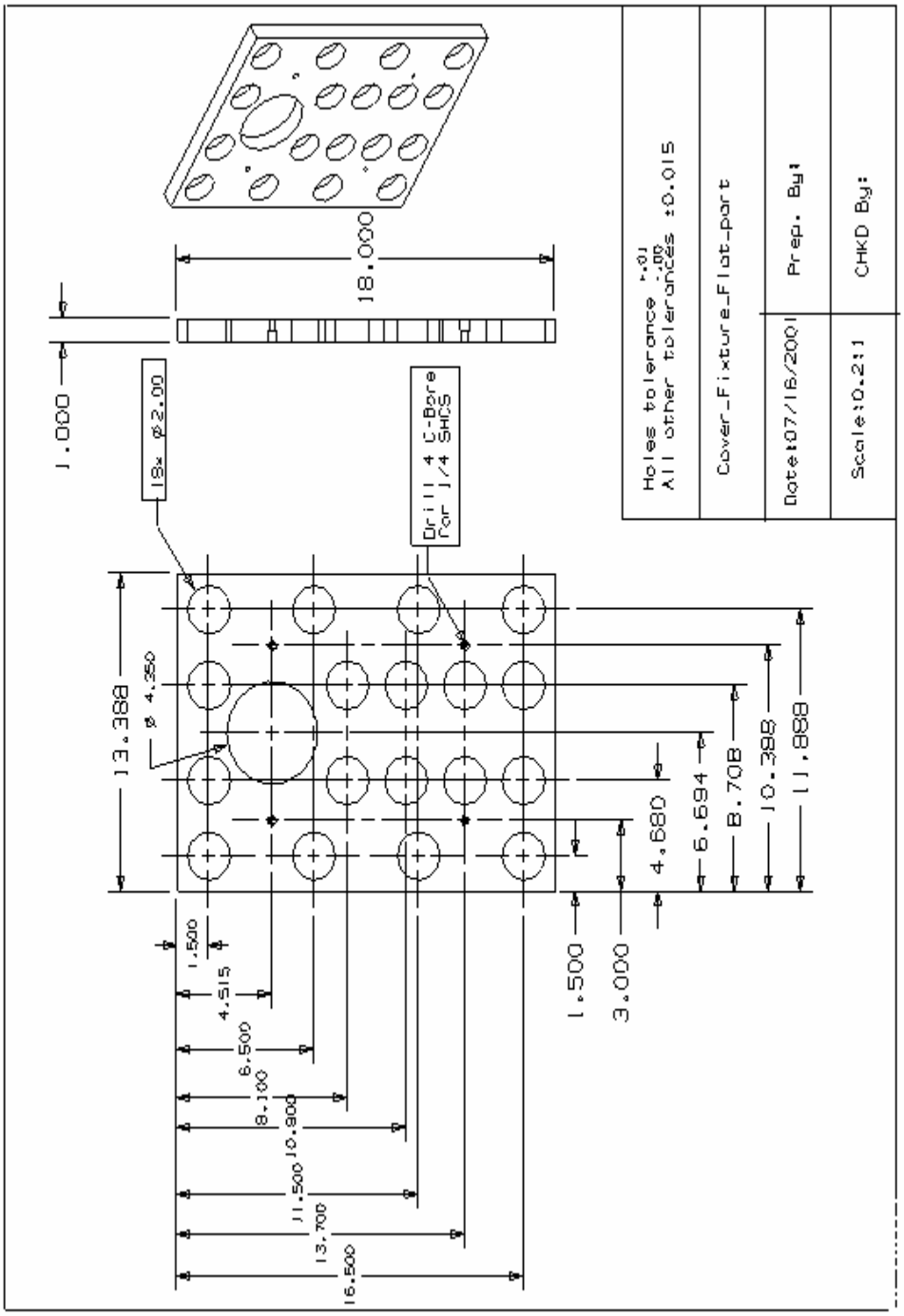

Figure A.2: Cover intermediate plate

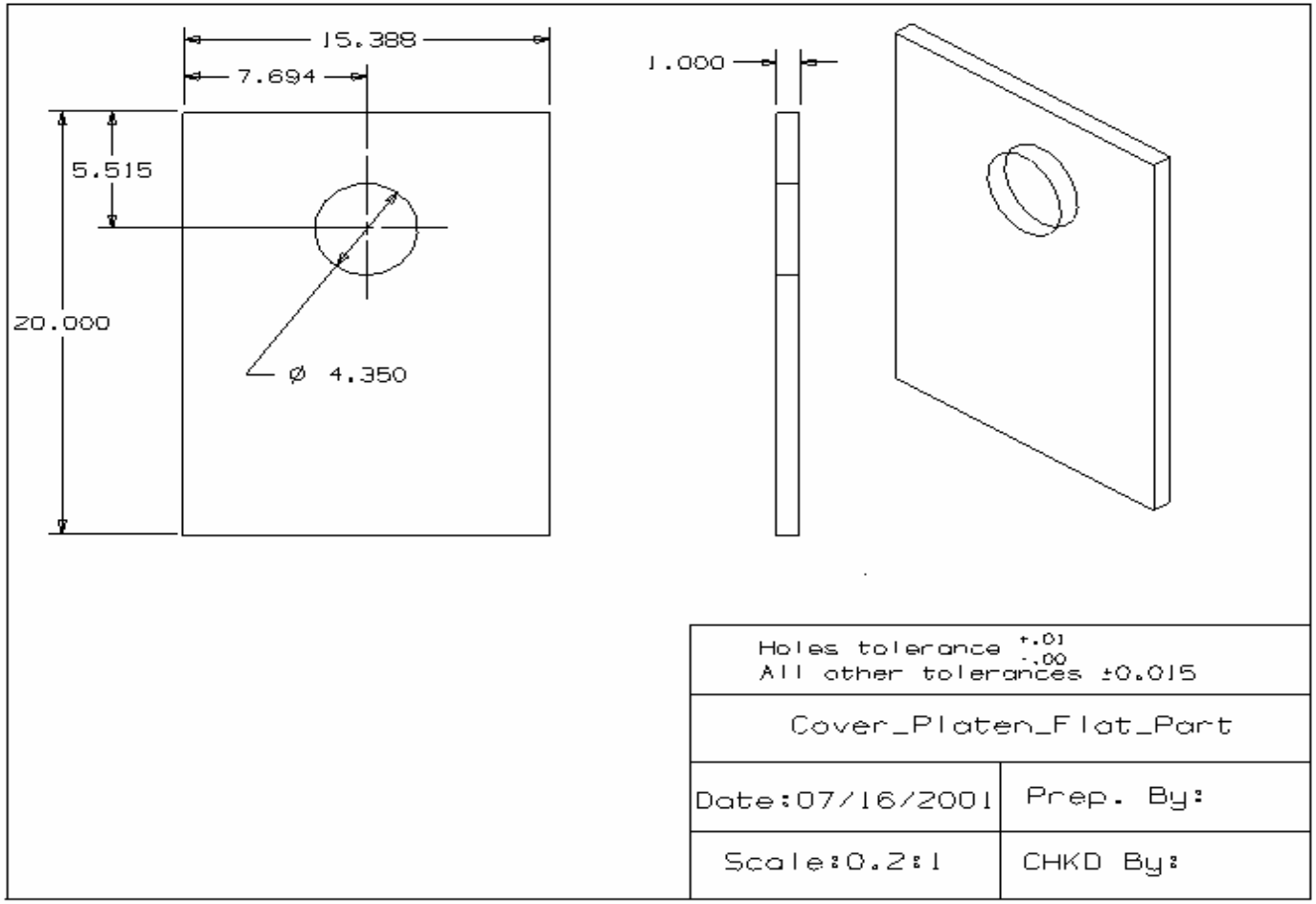

Figure A.3: Cover platen plate

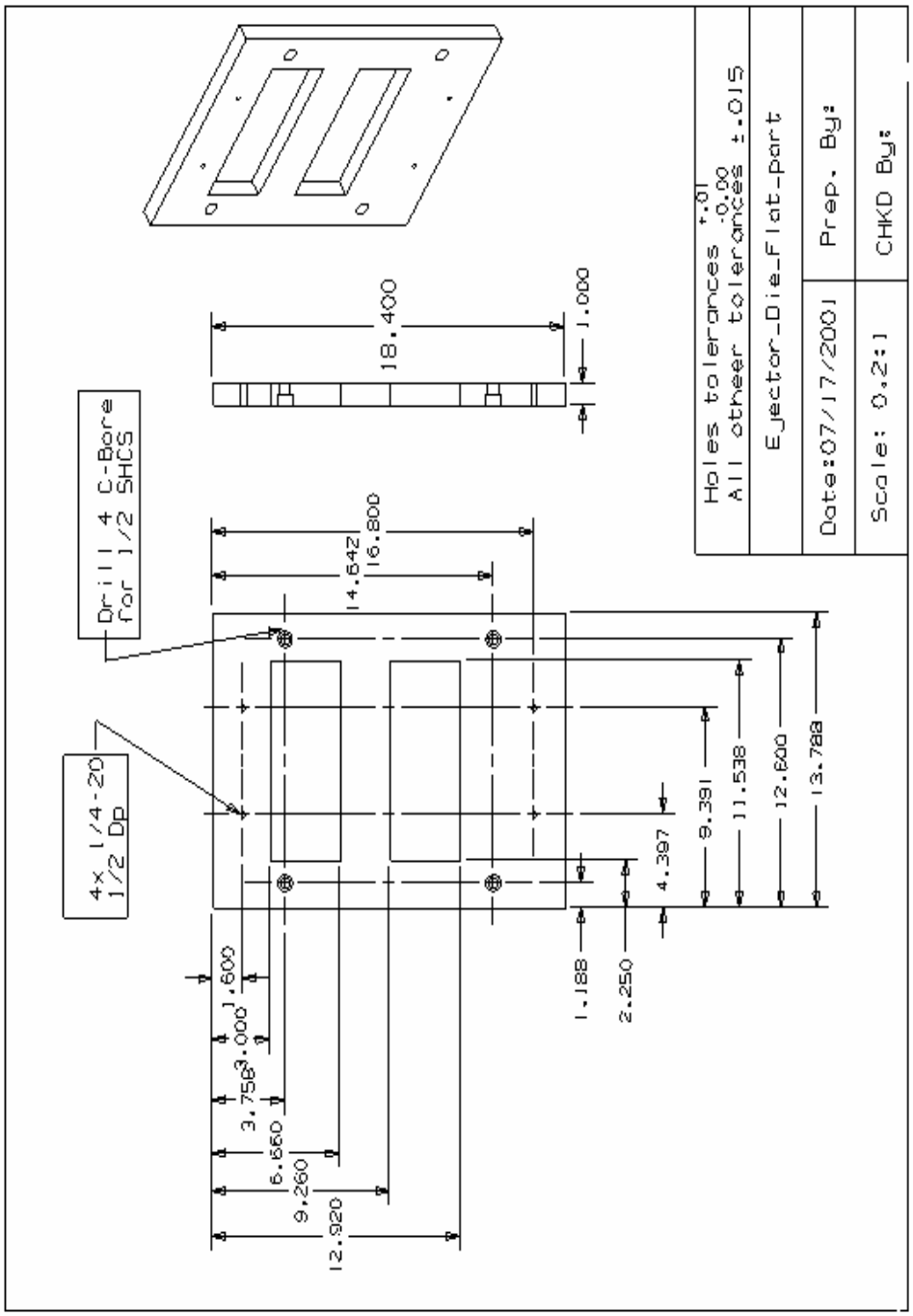

Figure A.4: Ejector die plate

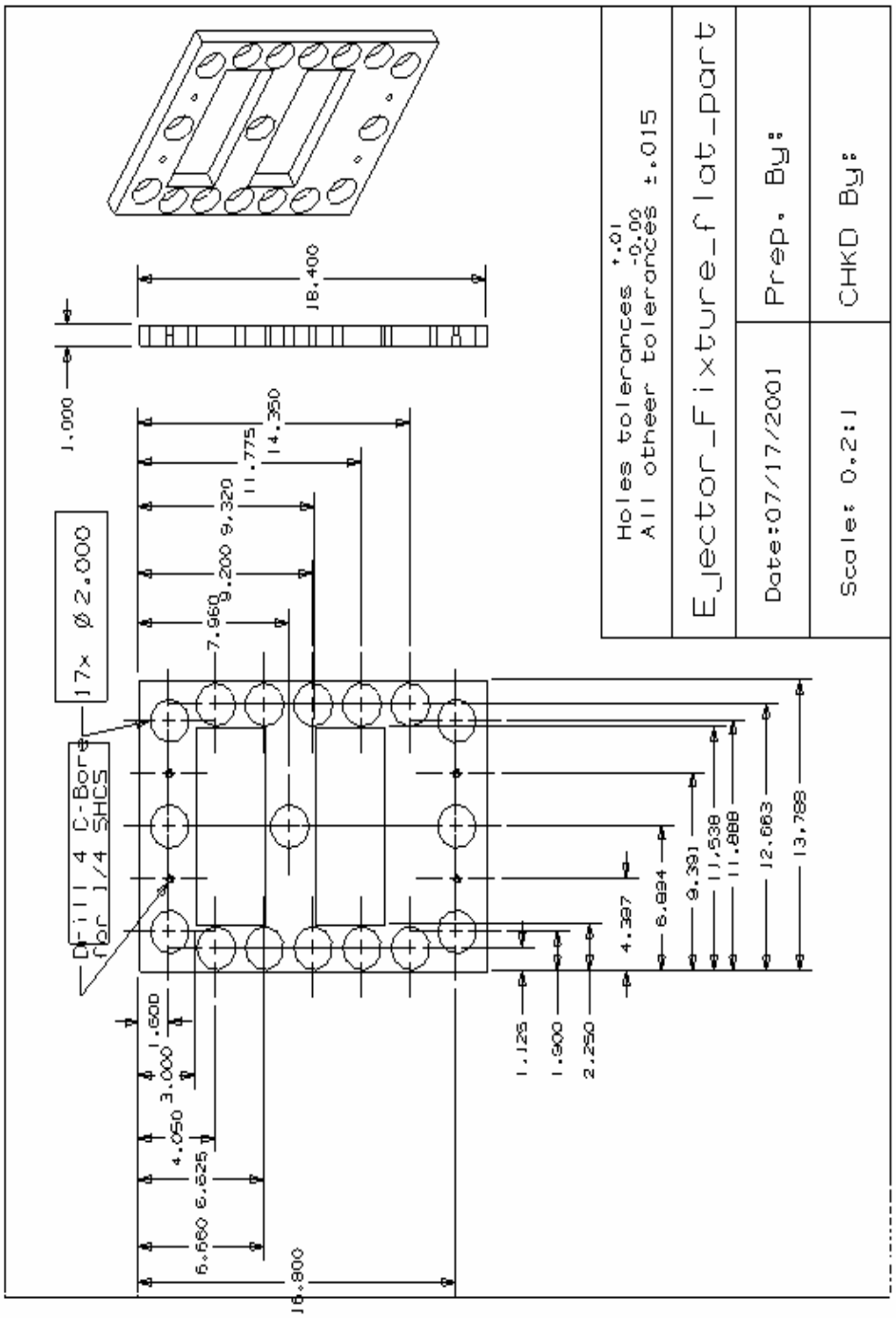

Figure A.5: Ejector intermediate plate

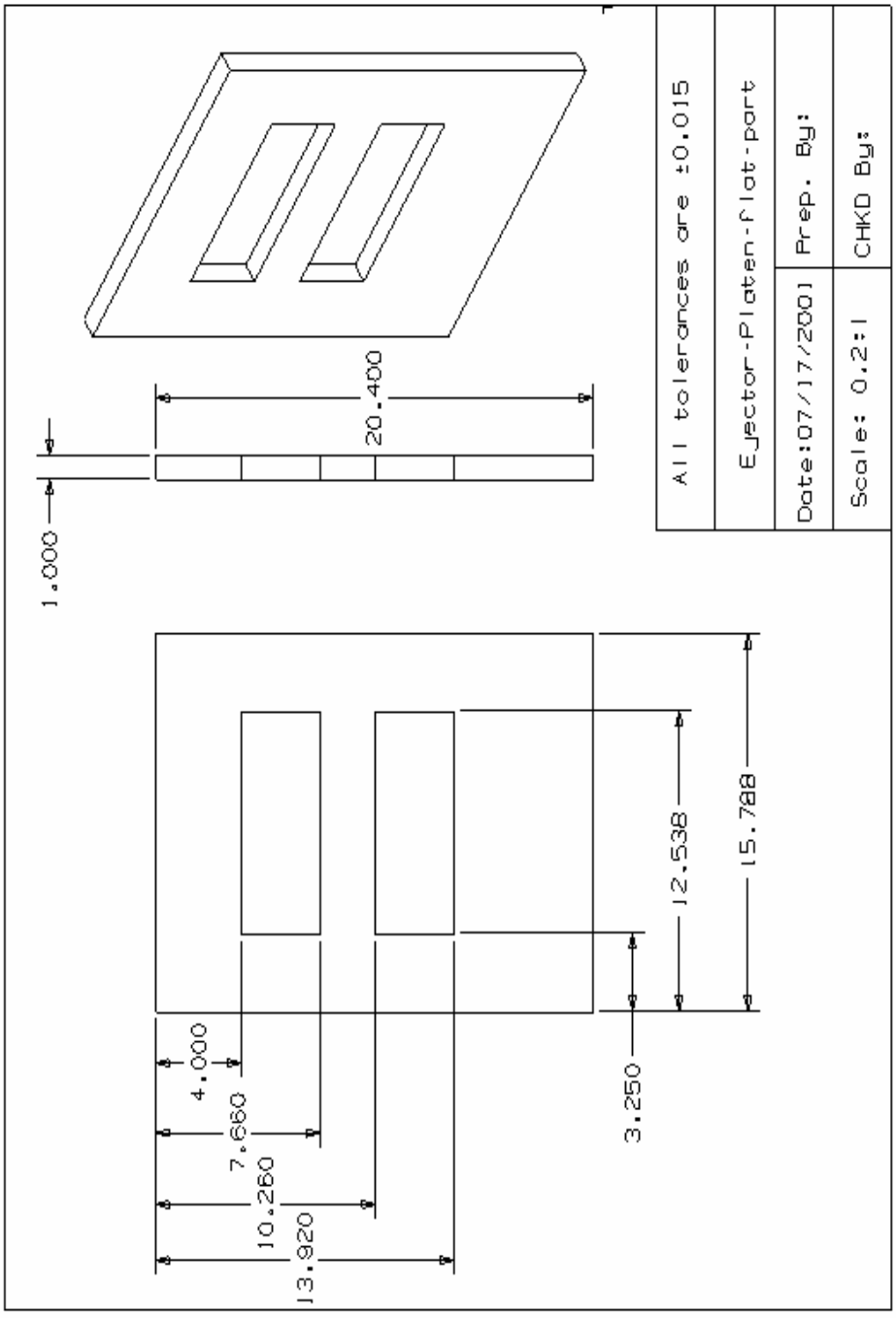

Figure A.6: Ejector platen plate

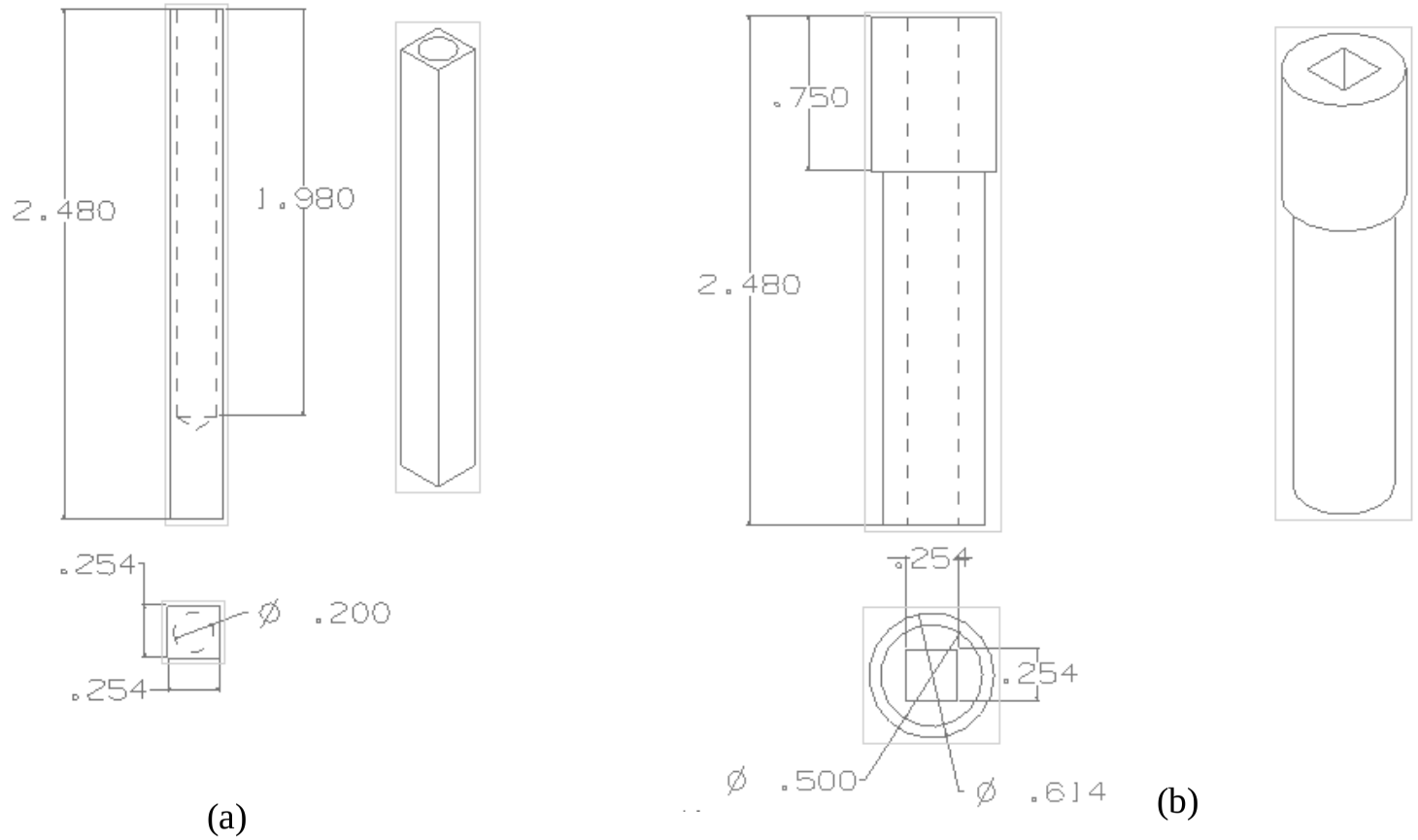

Figure A.7: Thermocouple fixture. Internal part (a), external part (b)

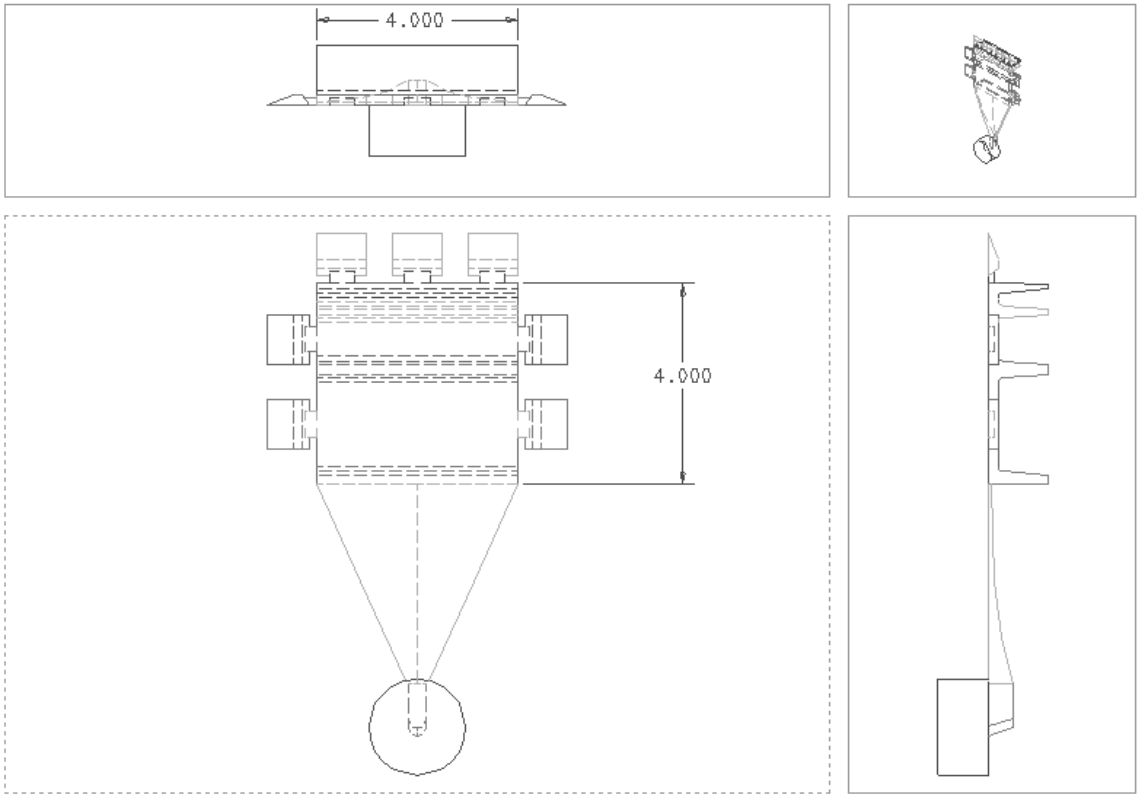

Figure A.8: Casting drawing

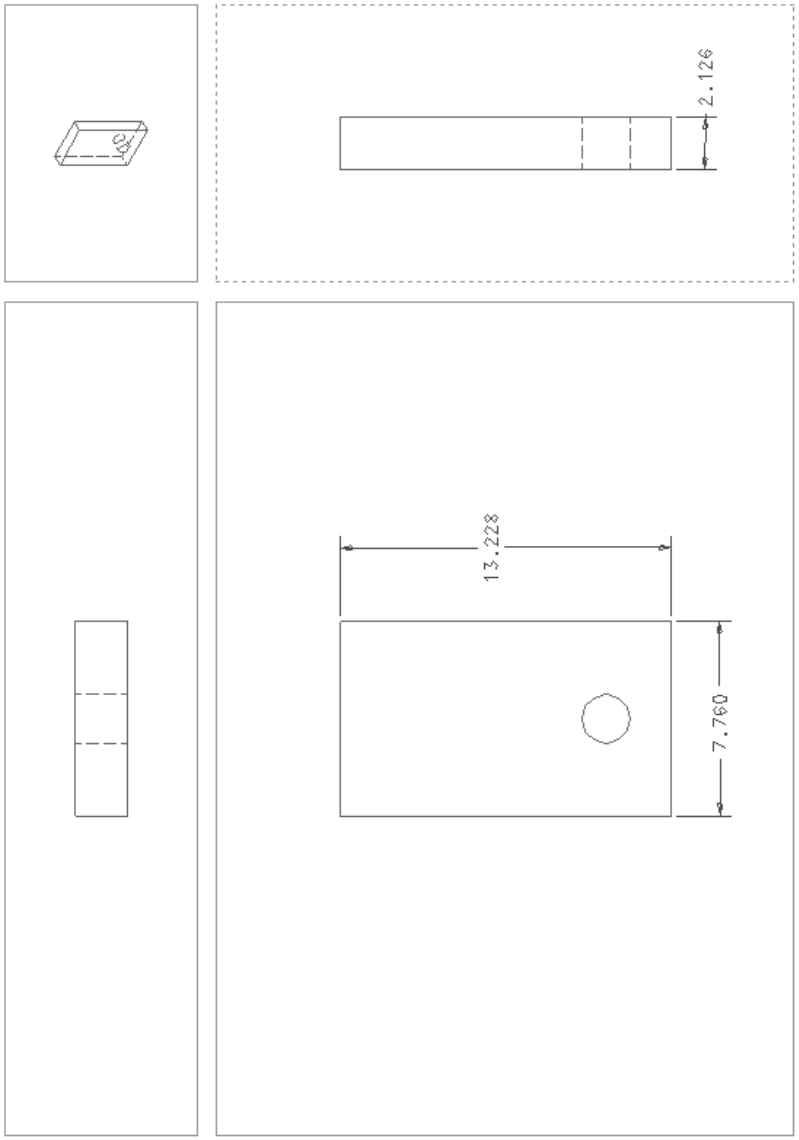

Figure A.9: Cover insert drawing

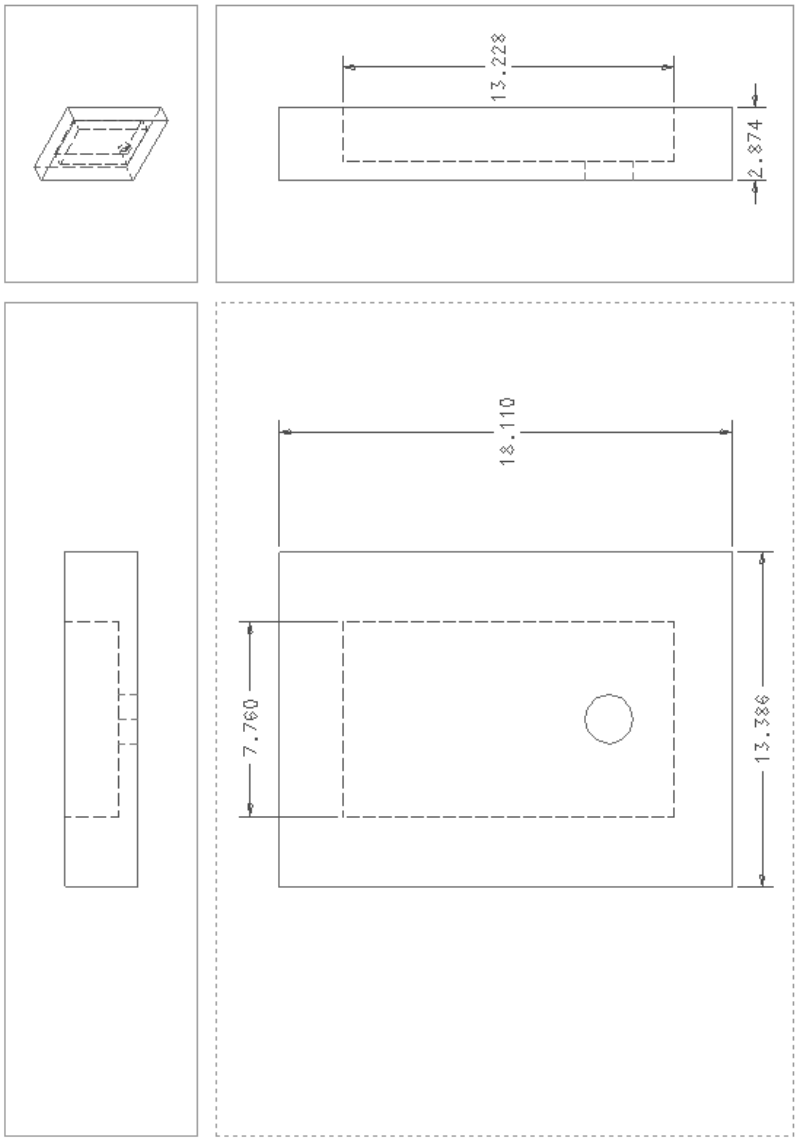

Figure A.10: Cover die drawing

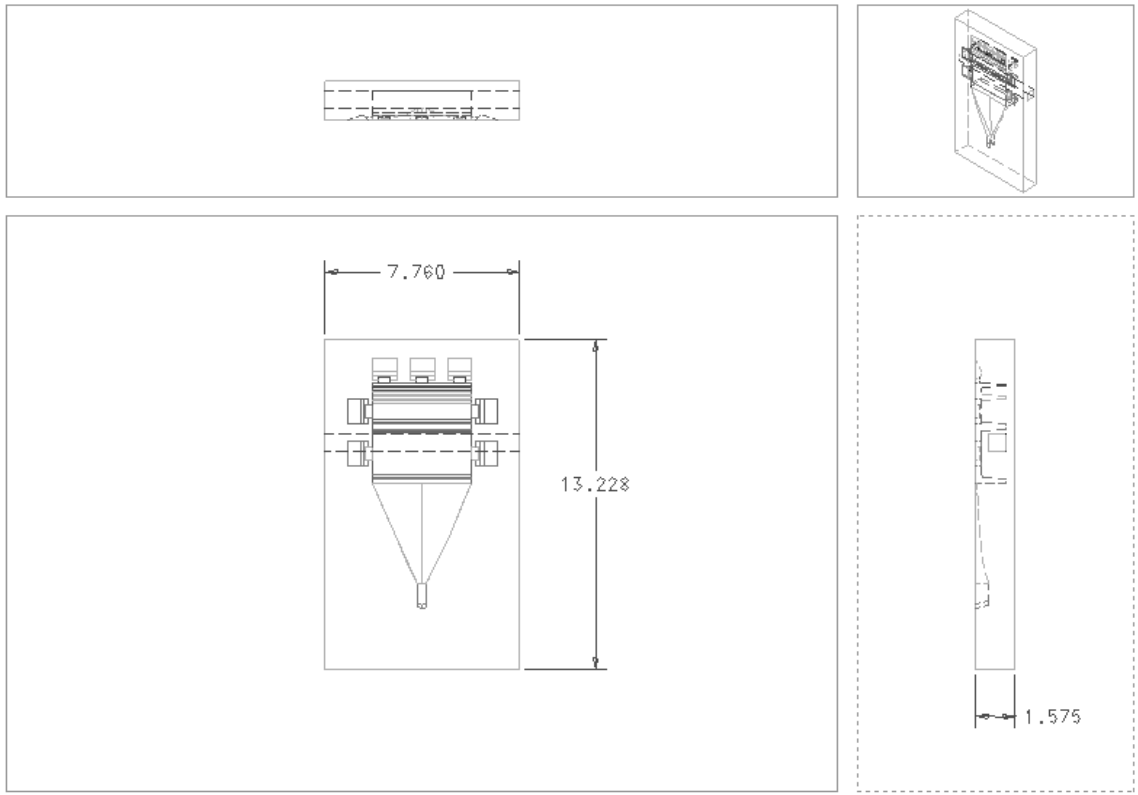

Figure A.11: Ejector insert drawing

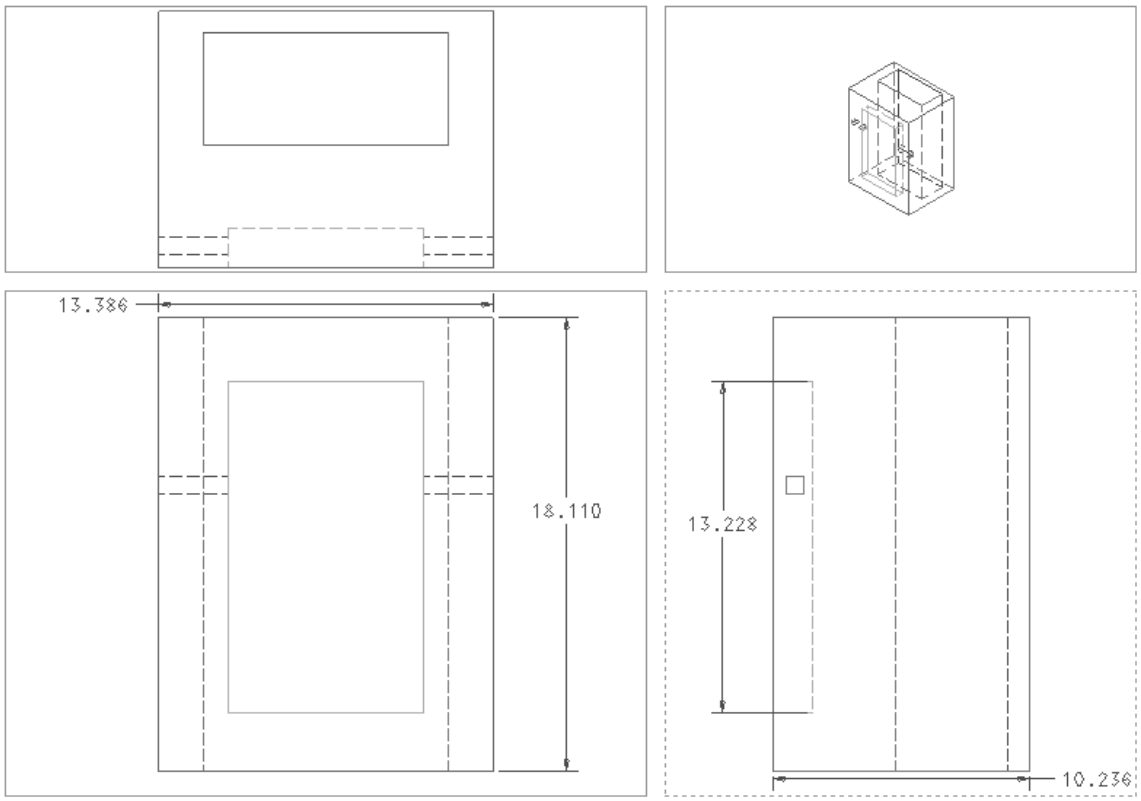

Figure A.12: Ejector die and back support drawing

APPENDIX B

SENSORS SPECIFICATIONS

B.1 Load cells specifications

The load cells were purchased from OMEGA-DYNE. The model selected is LC307-100K. Load cells properties are given in Table B.1 [41].

Property	Value
Range	0-100,000 lbs
Safe overload	150,000 lbs
Ultimate overload	300,000 lbs
Linearity	1% FSO
Zero balance	2% FSO
Operating temperature range	-54 to +121 ^{o}C
Compensated temperature range	+15 to +71^{o}C
Excitation	5 V dc

Table B.1: Load cells specifications

B.2 Thermocouples specifications

The thermocouples specifications are given in Table B.2.

Property	Value
Manufactures	OMEGA
Model	XC-20-K-24
Type	K
Size	20 gage
Range	(-185) - (+1250)^{o}C

Table B.2: Thermocouples specifications [41]

Table B.3 shows the specifications of the used cement used to fix the thermocouple in its fixture.

Property	Value
Coefficient of thermal expansion	4.6E-6
Maximum service temperature	843 ^{o}C
Thermal conductivity	1.15 W/mK
Electrical conductivity	Insulator

Table B.3: Cement properties

B.3Strain gages specifications

Property	Value
Manufactures	OMEGA
Model	SG-7/350-LY11
Maximum strain	30000 μ strain
Hysteresis	negligible
Service temperature (static)	-30-250 ^{o}C
Service temperature (Dynamic)	-30-300^{o}C
Glue type	SG496

Table B.4: Strain gages specifications

APPENDIX C

LABVIEW PROGRAM

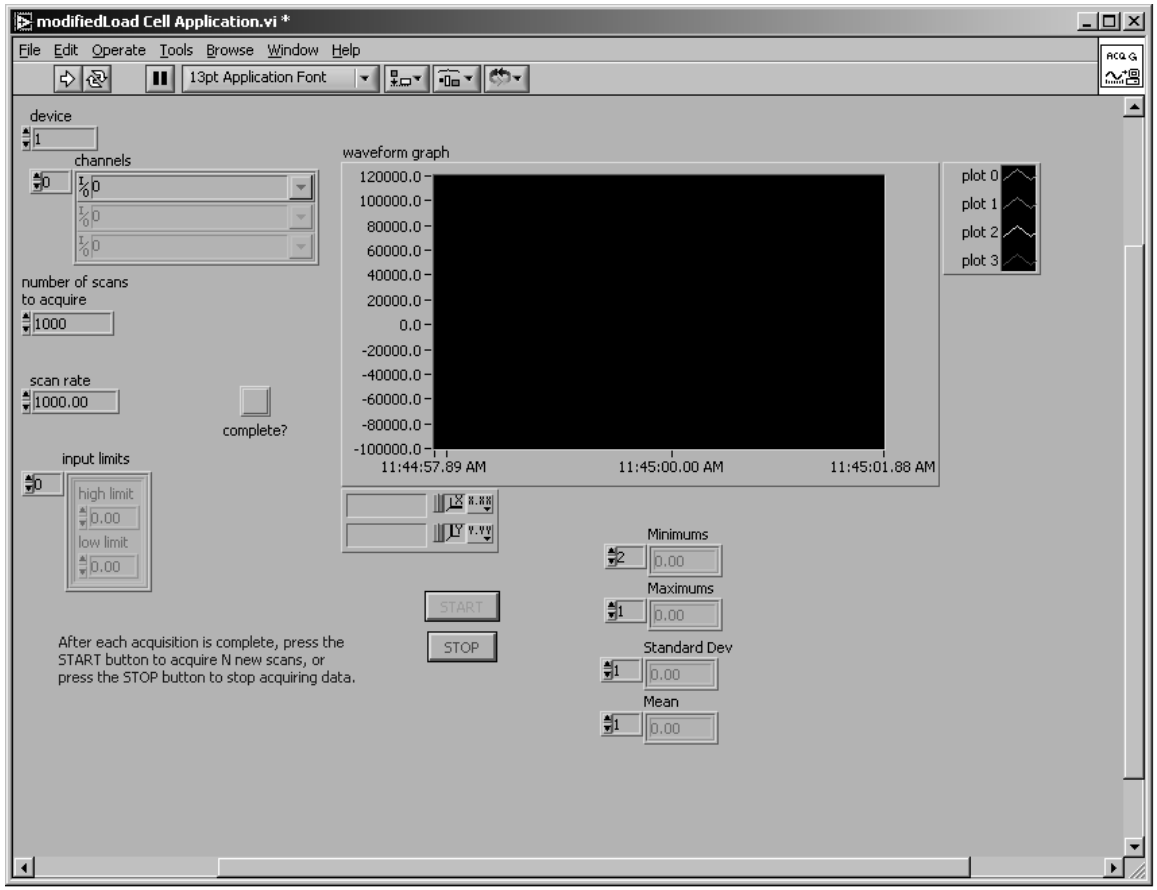

Figure C-1: Labview program main window

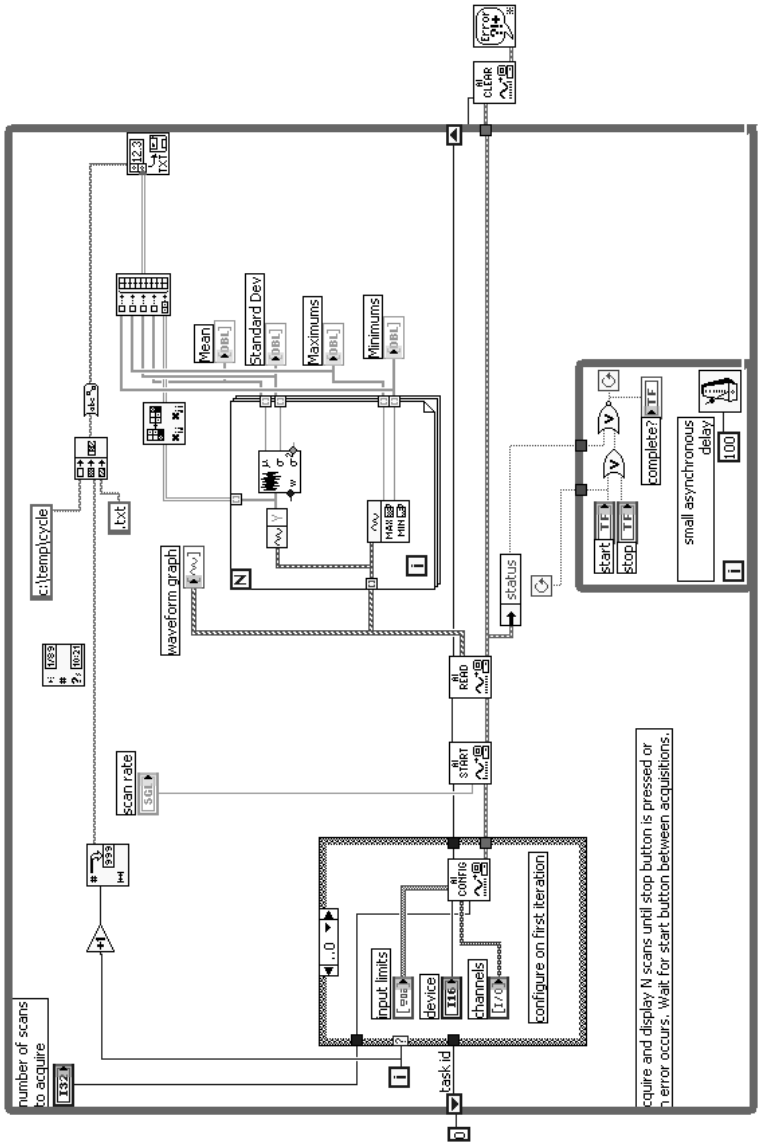

Figure C-2: Labview program diagram window

APPENDIX D

EXPERIMENTAL DATA

In this appendix, some of the experimental raw data are presented. Table D.1 shows the status of each casting made (good or bad). The casting was considered good if it had no filling problem (i.e. no cavities on the casting surface) otherwise it was considered as a bad casting.

Table D.2 demonstrates the cooling condition and the weight of every good casting. Two cooling conditions were used: air cooling (A) and water cooling (W). Tables D.3 and D.4 illustrate the raw data from the castings measurements using the CMM. Table D.5 describes the CMM specifications. Tables D.6 and D.7 depicts few of the readings by the load cells during one run.

D.1 Summary of Casting Data

Casting #	Status (**G**ood or **B**ad)	Casting #	Condition (**G**ood or **B**ad)
1	B	35	G
2	B	36	G
3	B	37	G
4	G	38	G
5	B	39	G
6	B	40	G
7	B	41	G
8	B	42	G
9	B	43	G
10	G	44	B
11	B	45	B
12	B	46	B
13	G	47	G
14	B	48	B
15	G	49	B
16	G	50	G
17	B	51	G
18	G	52	G
19	B	53	G
20	B	54	G
21	B	55	B
22	G	56	G
23	B	57	G
24	B	58	G
25	B	59	G
26	G	60	G
27	G	61	G
28	G	62	G
29	G	63	G
30	G	64	G
31	B	65	G
32	G	66	G
33	G	67	G
34	G		

Table D.1: Castings condition

Serial #	Casting #	Cooling (**A**ir or **W**ater)	Weight (gram)
1	4	A	296
2	10	A	291
3	13	A	290
4	15	A	291
5	16	A	293
6	18	A	291
7	22	A	297
8	26	A	291
9	27	A	294
10	28	A	297
11	29	A	295
12	30	A	291
13	32	A	299
14	33	A	296
15	35	A	293
16	36	A	294
17	37	A	296
18	38	A	297
19	39	A	297
20	40	A	296
21	41	A	296
22	42	w	297
23	43	A	289
24	47	A	289
25	50	W	297
26	51	A	300
27	52	W	298
28	53	A	297
29	54	W	298
30	56	W	299
31	57	W	298
32	58	A	300
33	59	A	299
34	60	W	299
35	61	W	299
36	62	W	299
37	63	W	296
38	64	A	297
39	65	W	298
40	66	A	300
41	67	W	298

Table D.2: Castings cooling condition and weight

Serial #	Casting #	D1(mm)	D2(mm)	D3(mm)	H(mm)	Flatness (R-square)
1	4	9.746	24.902	50.157	30.030	0.9727
2	10	9.743	24.900	50.140	30.038	0.9642
3	13	9.741	24.882	50.122	30.063	0.9487
4	15	9.746	24.897	50.129	30.135	0.9679
5	16	9.756	24.887	50.114	30.038	0.9414
6	18	9.749	24.889	50.109	30.107	0.9345
7	22	9.741	24.902	50.112	30.076	0.9826
8	26	9.751	24.900	50.117	30.066	0.9804
9	27	9.738	24.902	50.114	30.025	0.9730
10	28	9.779	24.978	50.135	29.901	0.8976
11	29	9.726	24.892	50.137	30.145	0.9815
12	30	9.733	24.884	50.117	30.140	0.9300
13	32	9.736	24.912	50.145	30.150	0.9967
14	33	9.743	24.917	50.129	30.010	0.9682
15	35	9.754	24.895	50.119	29.916	0.9608
16	36	9.731	24.892	50.145	30.002	0.9814
17	37	9.728	24.882	50.122	29.962	0.9764
18	38	9.726	24.882	50.119	30.020	0.9555
19	39	9.726	24.884	50.119	30.066	0.9743
20	40	9.728	24.882	50.127	30.051	0.9852
21	41	9.733	24.887	50.124	30.030	0.9791
22	43	9.741	24.900	50.114	30.213	0.9614
23	47	9.779	24.902	50.122	29.898	0.9287
24	51	9.764	24.910	50.119	30.089	0.9957
25	53	9.749	24.900	50.124	29.990	0.9734
26	58	9.728	24.889	50.114	30.051	0.9610
27	59	9.746	24.907	50.132	30.043	0.9850
28	64	9.731	24.895	50.129	30.058	0.9805
29	66	9.743	24.905	50.137	29.944	0.9803

Table D.3 Air cooled castings dimensions and flatness

Serial #	Casting #	D1(mm)	D2(mm)	D3(mm)	H(mm)	Flatness (R-square)
1	42	9.736	24.887	50.104	30.063	0.9678
2	50	9.751	24.897	50.112	29.944	0.9753
3	52	9.731	24.882	50.117	30.142	0.9901
4	54	9.738	24.900	50.109	30.074	0.9910
5	56	9.731	24.884	50.117	30.043	0.9743
6	57	9.731	24.882	50.122	30.010	0.9814
7	60	9.723	24.892	50.124	30.124	0.9911
8	61	9.738	24.884	50.119	30.063	0.9862
9	62	9.731	24.895	50.137	30.053	0.9668
10	63	9.726	24.889	50.109	30.147	0.9813
11	65	9.718	24.892	50.109	30.287	0.9855
12	67	9.721	24.882	50.117	30.051	0.9678

Table D.4: Water cooled castings dimensions and flatness

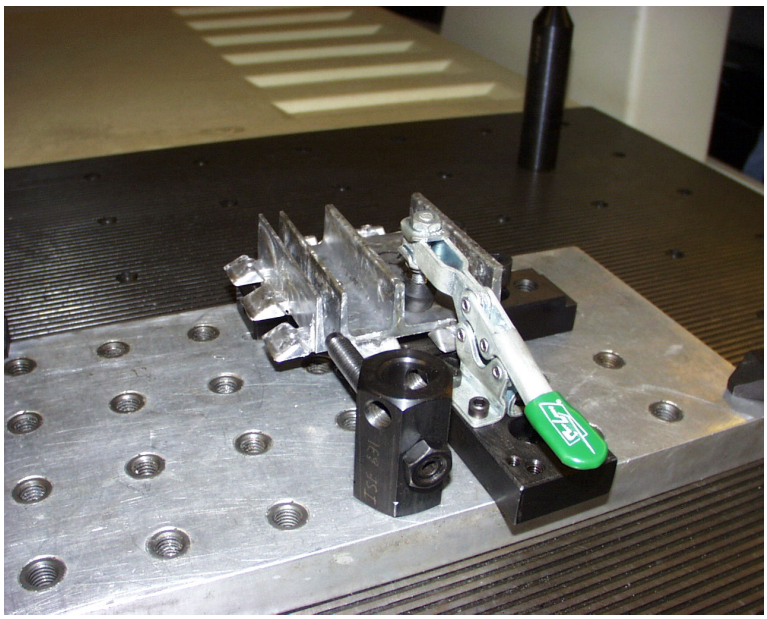

Figure D.1: Fixture for measuring the dimensions

Specification	Value
Manufacturer	Sheffield Cordax
Model	R-30
Linear accuracy (in/mm)	0.003/0.00012
Volumetric accuracy (in/mm)	0.0055/0.0002
Repeatability (in/mm)	0.0055/0.0002

Table D.5: CMM specifications

D.2 Summary of Load Cells Readings

C1	C2	C3	C4	C5	C6	C7	C8	C9	C10	C11	C12	C13	C14	C15	C16	C17	C18
140	143	174	195	266	58	48	123	103	256	44	46	6	100	165	148	180	170
140	143	174	195	266	58	48	123	103	256	44	46	6	100	166	148	180	170
140	143	174	195	266	58	48	123	103	256	44	46	6	100	166	148	180	170
140	143	174	195	266	58	48	123	103	256	44	46	6	100	166	148	180	170
140	143	174	195	266	58	48	123	103	256	44	46	6	100	165	148	180	170
140	143	174	195	266	58	48	123	103	256	44	46	6	100	166	148	180	170
140	143	174	195	266	58	48	123	103	256	44	46	6	100	166	148	180	170
140	143	174	195	266	58	48	123	103	256	44	46	6	100	165	148	179	170
140	143	174	195	266	58	48	123	103	257	44	46	6	100	166	148	180	170
140	143	174	195	266	58	48	123	103	256	44	46	6	100	166	148	180	170
140	143	174	195	266	58	48	123	103	256	44	46	6	100	166	148	180	170
140	143	174	195	266	58	48	123	103	256	44	46	6	100	166	148	180	170
140	143	174	195	266	58	48	123	103	256	44	46	6	100	166	148	180	170
140	143	174	195	266	58	48	123	103	256	44	46	6	100	166	148	180	170
140	143	174	195	266	58	48	123	103	256	44	46	6	100	166	148	180	170
140	143	174	195	266	58	48	123	103	256	44	46	6	100	166	148	180	170
140	143	174	195	266	58	48	123	103	256	44	46	6	100	166	148	180	170
140	143	174	195	266	58	48	123	103	256	44	46	6	100	166	148	180	170
140	143	174	195	266	58	48	123	103	256	44	46	6	100	166	148	180	170
140	143	174	195	266	58	48	123	103	256	44	46	6	100	166	148	180	170

Table D.6: Sample readings by load cells at cover side at load condition I (2452KN) (from one run)

E1	E2	E3	E4	E5	E6	E7	E8	E9	E10	E11	E12	E13	E14	E15	E16	E17
233	187	134	114	174	174	152	64	46	30	249	147	146	141	120	103	138
233	187	134	114	174	174	152	64	46	30	249	147	146	141	120	103	138
233	187	134	114	174	174	152	64	46	30	249	147	146	141	120	103	138
233	187	134	114	174	174	152	64	46	30	249	147	146	141	120	103	138
233	187	134	114	174	174	152	64	46	30	249	147	146	141	120	103	138
233	187	134	114	174	174	152	64	46	30	249	147	146	141	120	103	138
233	187	134	114	174	174	152	64	46	30	249	147	146	141	120	103	138
233	187	134	114	174	174	152	64	46	30	249	148	146	141	120	103	138
233	187	134	114	174	174	152	64	46	30	249	147	146	141	120	103	138
233	187	134	114	174	174	152	64	46	30	249	147	146	141	120	103	138
233	187	134	114	174	174	152	64	46	30	249	147	146	141	120	103	138
233	187	134	114	174	174	152	64	46	30	249	147	146	141	120	103	138
233	187	134	114	174	174	152	64	46	30	249	147	146	141	120	103	138
233	187	134	114	174	174	152	64	46	30	249	147	146	141	120	103	138
233	187	134	114	174	174	152	64	46	30	249	147	146	141	120	103	138
233	187	134	114	174	174	152	64	46	30	249	147	146	141	120	103	138
233	187	134	114	174	174	152	64	46	30	249	147	146	141	120	103	138
233	187	134	114	174	174	152	64	46	30	249	147	146	141	120	103	138
233	187	134	114	174	174	152	64	46	30	249	147	146	141	120	103	138
233	187	134	114	174	174	152	64	46	30	249	148	146	141	120	103	138
233	187	134	114	174	174	152	64	46	30	249	147	146	141	120	103	138

Table D.7: Sample readings by load cells at cover side at load condition I (2452KN) (from one run)

APPENDIX E

SIMULATION DATA

Run	Ejection temperature (^{o}C)		
	Point 1	Point 2	Point3
1	277	325	303
2	285	334	311
3	292	344	319
4	292	344	319
5	277	325	304
6	284	333	310
7	322	380	348
8	330	392	357
9	309	363	335

Table E.1: Ejection temperature at locations 1, 2 and 3 for the DOE cases

Run	Von Mises stresses (^{MPa})		
	Point 1	Point 2	Point3
1	91	65	78
2	160	149	158
3	97	107	97
4	78	104	88
5	165	148	165
6	87	81	85
7	55	70	68
8	155	151	156
9	89	82	88

Table E.2: Von Mises stresses at locations 1, 2 and 3 for the DOE cases at ejection

Run	Von Mises stresses (^{MPa})		
	Point 1	Point 2	Point3
1	16	40	10
2	31	61	21
3	24	65	30
4	26	73	48
5	20	66	23
6	28	74	54
7	58	86	44
8	66	109	77
9	19	79	20

Table E.3: Von Mises stresses at locations 1, 2 and 3 for the DOE cases at room temperature (air cooling)

Run	Von Mises stresses (^{MPa})		
	Point 1	Point 2	Point3
1	16	39	10
2	31	61	21
3	20	66	23
4	11	92	50
5	20	66	23
6	28	75	74
7	59	97	45
8	66	110	77
9	20	80	20

Table E.4: Von Mises stresses at locations 1, 2 and 3 for the DOE cases at room temperature (water cooling)

Run	Von Mises stresses (^{MPa})		
	Point 1	Point 2	Point3
1	5	27	10
2	5	28	11
3	5	26	14
4	4	16	54
5	5	29	13
6	5	30	13
7	2	13	14
8	5	13	9
9	4	17	19

Table E.5: Von Mises stresses at locations 1, 2 and 3 for the DOE cases at room temperature (air cooling – stress free)

Run	Change in dimension (mm)			
	D1	D2	D3	H
1	-0.019	-0.024	-0.019	0.043
2	-0.028	-0.039	-0.039	0.072
3	-0.028	-0.040	-0.041	0.085
4	-0.025	-0.033	-0.033	0.084
5	-0.025	-0.035	-0.030	0.052
6	-0.025	-0.035	-0.034	0.074
7	-0.023	-0.030	-0.028	0.062
8	-0.029	-0.038	-0.038	0.071
9	-0.021	-0.025	-0.021	0.046

Table E.6: Change in dimensions D1, D2, D3 and H at ejection for the DOE cases

Run	Change in dimension (mm)				Flatness (R-square)
	D1	D2	D3	H	
1	0.108	0.212	0.400	0.276	0.954
2	0.102	0.229	0.415	0.351	0.957
3	0.150	0.245	0.443	0.358	0.955
4	0.161	0.239	0.441	0.337	0.950
5	0.015	0.175	0.323	0.311	0.958
6	0.143	0.220	0.415	0.321	0.955
7	0.125	0.282	0.493	0.351	0.954
8	0.130	0.339	0.465	0.426	0.956
9	0.049	0.144	0.423	0.295	0.957

Table E.7: Change in dimensions D1, D2, D3 and H and the flatness of the back surface at room temperature for the DOE cases